Untangling Galaxy Components: the Kinematics and Stellar Populations of Bulges and Disks

Martha Tabor



The University of Nottingham

Thesis submitted to the University of Nottingham
for the degree of Doctor of Philosophy, February 2019

"If you're in pitch blackness, all you can do is sit tight until your eyes get used to the dark."

– Haruki Murakami

Supervisors:	Prof. Michael Merrifield
	Prof. Alfonso Aragón-Salamanca
Examiners:	Dr Russell J. Smith
	Prof. Chris Conselice

Abstract

Photometric bulge-disk decompositions have long been used as a way of separating out the central and extended components in a galaxy. However, whether these photometric components are made up of different stellar populations with distinct kinematics, or whether they are just a convenient way to fit a galaxy light profile, is not clear. By developing a method of bulge-disk decomposition that exploits both spectroscopic and photometric information available in integral field spectroscopy, we separate out bulges and disks based on their stellar populations and kinematics, to see if they are truly distinct. Tests of this new method on an initial sample of three S0 galaxies shows that the data are best fit when including two components with different kinematics, demonstrating that, at least in some of these systems, bulges and disks are indeed distinct and separable components. We therefore decided to apply the method to a larger sample from the MaNGA survey.

By applying this spectroscopic decomposition to this large sample of early-type galaxies, we extract information on the kinematics and stellar populations of bulges and disks, allowing us to compare the age, metallicity, specific angular momentum, j, and spin parameter, λ_R, of the individual components. We find that bulges and disks have similar ages, but different metallicities, with bulges tending to have higher metallicity than their corresponding disks. Bulges and disks follow their own distinct kinematic relationships, both on the plane of the stellar spin parameter, λ_R, and ellipticity, ϵ, and in the relation between stellar mass, M_*, and specific angular momentum, j_*, with the location of the galaxy as a whole on these planes being determined by how much bulge and disk it contains.

As a check of the physical significance of the kinematic decompositions, we also dynamically model the individual galaxy components within the global potential of the

galaxy. The resulting components exhibit kinematic parameters consistent with those derived from the spectroscopic decomposition, and though the dynamical modelling suffers from some degeneracies, the bulges and discs display systematically different intrinsic dynamical properties. An application to MUSE data, with higher spatial and spectral resolution, indicates that with high enough quality data it is possible to separate bulges and disks into distinct physically-meaningful components.

The work presented in this thesis demonstrates the value in considering the individual components of galaxies rather than treating them as a single entity, which neglects information that may be crucial in understanding where, when and how galaxies evolve into the systems we see today.

Acknowledgements

There are so many people who have helped to achieve the work presented in this thesis. First and foremost, I want to thank my supervisors, Mike and Alfonso, for helping and supporting me over the last 4 years. Their seemingly limitless stock of ideas and knowledge about astronomy is amazing, and their encouragement and honesty has been so helpful in getting me to this point.

I also want to thank everyone who encouraged my interest in physics and astronomy over the years, from a great physics teacher in high school, to the people who allowed me to attempt to help, while probably hindering, their research in various summer projects.

Thanks to everyone in CAPT for being the source of endless pedantic conversions to distract me from work. Extra thanks to Lyndsay Old and Tom Clarke for being awesome friends and Broadway companions. In fact, thanks to Broadway cinema for being my second home and never questioning my request for under 25 tickets.

Thanks to the friends I made in La Palma for making it a great year. I hope to have a gara or two on the beach again with you all at some point!

I want to thank Tom for being the best friend a person could ask for, and for getting me through the tough times and making the good times better. Turns out there aren't many problems that a few too many whiskies and a bad rendition of Wagon Wheel wont solve.

Lastly, I want to thank my parents for their constant support and interest, for providing a home whenever I needed a break, and for encouraging me to be curious about how everything in the world, and beyond, works. This thesis is dedicated to them.

Contents

List of Figures **iv**

List of Tables **vi**

1 Introduction **1**

1.1 Galaxy Morphological Classifications 1

1.2 Galaxy evolution: late-types to early-types 4

1.2.1 Internal Processes 4

1.2.2 External Processes 6

1.2.3 Environment versus mass 7

1.2.4 Effects on the components of galaxies 8

1.3 Bulge-Disk decompositions 8

1.3.1 Photometric bulge-disk decompositions 9

1.3.2 Trends with bulge-to-total ratio 9

1.3.3 Properties of bulges and disks 11

1.3.4 The distinctness of bulges and disks 15

1.3.5 Spectroscopic bulge-disk decomposition 15

1.4 Thesis Structure 17

2 Data **19**

2.1 Integral Field Spectroscopy 19

2.2 CALIFA 22

2.2.1 Sub-sample selection 23

2.3 The MaNGA Survey 24

2.3.1 Sample Selection 26

3 Spectroscopic decomposition **29**

3.1 The Method 30

3.1.1 Photometric bulge–disk decomposition 30
3.1.2 Spectroscopic bulge–disk decomposition 33
3.1.3 Tests 34
3.1.4 NGC 528 42
3.1.5 NGC 7671 and NGC 6427 45
3.1.6 Stellar Populations 48
3.2 Discussion 52
3.2.1 The Method 52
3.2.2 Bulge and disk properties 53
3.3 Conclusions 54

4 Spectroscopic Decomposition of MaNGA early-type galaxies 56
4.1 Enhancements to the method 57
4.1.1 Photometric Decomposition 57
4.1.2 Spectroscopic Decomposition 58
4.1.3 Aperture effects 64
4.2 Stellar Populations 65
4.2.1 Age and metallicity 65
4.2.2 Star-formation histories 67
4.3 Kinematics 70
4.3.1 Specific angular momentum 71
4.3.2 Stellar Spin Parameter, λ_R 76
4.4 Applying spectroscopic decomposition to large IFU surveys 79
4.5 Conclusions 81

5 JAM Dynamical modelling 83
5.1 Dynamical models 84
5.2 Building the models 86
5.3 Comparing spectroscopic decomposition to dynamical modelling . . . 91
5.4 Addressing the distinctness of JAM components 97
5.5 Conclusions 100

6 Discussion and further work 101
6.1 Discussion 101
6.1.1 The existence of bulges and disks 101

6.1.2 Properties of bulges and disks 102
6.2 Further work 107
6.2.1 Spectroscopic decomposition of spiral galaxies 107
6.2.2 Extending spectroscopic decomposition to lower masses . . . 110
6.2.3 Dynamical modelling 110
6.2.4 The bulge-disk decomposition method to end all bulge-disk decomposition methods 111

Bibliography **112**

List of Figures

1.1 Hubble tuning fork 2
1.2 Hubble tuning fork - kinematic update by Capellari 4
1.3 Galaxy colour-mass diagram 5
1.4 The Sérsic profile 10
1.5 The $M_* - j_*$ relation 12
1.6 The $\lambda_R - \epsilon$ relation 13
1.7 Contamination of disk with varying bulge-to-total ratio 14

2.1 IFU data-cube 21
2.2 SDSS images of the CALIFA test galaxies 24
2.3 Sample mass distribution 27

3.1 GALFIT photometric bulge-disk decomposition of NGC 528 32
3.2 Simulated bulge and disk tests 35
3.3 Simulated bulge and disk tests with similar properties 38
3.4 Chi-squared maps for grid of bulge and disk velocities along galaxy major axis 40
3.5 Kinematic maps for NGC 528 44
3.6 Kinematic maps for NGC 7671 46
3.7 Kinematic maps for NGC 6427 47
3.8 Age and metallicity maps for NGC 528 49
3.9 Age and metallicity maps for NGC 7671 50
3.10 Age and metallicity maps for NGC 6427 51

4.1 Schematic of spectroscopic bulge-disk decomposition method 59
4.2 Kinematic maps for galaxy 8249-3701 61
4.3 Kinematic maps for galaxy 8259-3701 62
4.4 Kinematic maps for galaxy 8253-3701 63
4.5 Bulge and disk flux-weighted age and metallicity 67

4.6 Stellar population comparison with other work 68
4.7 Mass-metallicity relalation for the bulge and disk components 69
4.8 Star-formation histories for the bulge and disk 70
4.9 Star-formation histories for the bulge and disk for different galaxy masses 71
4.10 Angular momentum–stellar mass relation for bulges and disks 75
4.11 Projected specific angular momentum of the bulge and disk components 76
4.12 λ_{Re} vs ellipticity, ϵ for decomposed bulges and disks 77
4.13 λ_{Re} vs ellipticity, ϵ for overlapping bulge and disk regions 79
4.14 Bulge effective radius versus bulge λ_{Re} 81

5.1 MGE fits to two example galaxies in the MaNGA survey 87
5.2 Observed $V_{\rm rms}$ (right) and JAM best-fit model $V_{\rm rms}$ for three sample galaxies 88
5.3 Kinematic maps for best fitting bulges and disks found using JAM modelling, compared to kinematic maps found for bulges and disks from the spectroscopic decomposition 90
5.4 Histogram of κ, the ratio of the observed velocity to the velocity field predicted by a JAM model with $\sigma_\phi = \sigma_R$ 92
5.5 Comparison between bulge and disk κ values obtained through JAM modelling of the global velocity field, and those obtained through JAM modelling of the spectroscopically decomposed components 94
5.6 Histogram of bulge and disk κ values 95
5.7 Bulge and disk kappa plotted against global galaxy κ. 96
5.8 JAM models for two MUSE observations 99

6.1 Angular momentum–stellar mass relation in the GADGET-3 simulation 105
6.2 Spectroscopic decomposition of a MaNGA spiral galaxy 109

List of Tables

2.1 CALIFA sample galaxy properties 24

3.1 Parameters of the GALIFT photometric decomposition 32

Published Work

Much of the material in this thesis has been presented in the two papers listed below:

- Tabor M., Merrifield M., Aragón-Salamanca A., Cappellari M., Bamford S. P., Johnston E., 2017, "Untangling galaxy components: full spectral bulge-disc decomposition", MNRAS, 466, 2024
- Tabor M., Merrifield M., Aragón-Salamanca A., Fraser-McKelvie A., Peterken T., Smethurst R., Drory N., Lane R. R., 2019, "SDSS IV MaNGA: Full spectroscopic bulge-disc decomposition of MaNGA early-type galaxies"

The majority of the work in Chapter 3 has been published in the first paper, while the work in Chapters 4 and 5 has been published in the second.

The vast majority of the work presented in this thesis was performed by the author, with advice from the coauthors listed above. When the material is taken from the literature, or the result of more collaborative research, this is stated in the relevant chapter.

Chapter 1

Introduction

"The history of astronomy is a history of receding horizons."

- Edwin Hubble

1.1 Galaxy Morphological Classifications

This thesis is aimed at understanding the morphological components present in galaxies, with respect to their stellar populations and the motions of their constituent stars.

It was Emmanuel Kant who first suggested in the 18th century that distant nebulae may in fact be other galaxies, revolutionising the field of astronomy and marking the beginning of the field of extragalactic studies. However, morphological classifications of these galaxies did not become prominent until the early 20th century, when Edwin Hubble proposed a classification system which divided galaxies into three types, as shown in Figure 1.1 (Hubble, 1926). On the left are elliptical galaxies, characterised by being 'red and dead' systems with no star formation and no visible structure. Their position on the diagram is determined by their perceived flattening, according to the ratio of the length of their major and minor axes. The right-hand side of the diagram is populated by spiral galaxies, containing some of the most visually beautiful galaxies in the Universe, populated by young stars and experiencing ongoing star formation.



Figure 1.1: Hubble tuning fork. Image credit: btc.montana.edu

It was observed that these galaxies appear to be made up of two parts: a flattened component, plus a central, more spheroidal component, referred to as the disk and bulge respectively. The horizontal position of a spiral galaxy on Hubble's diagram is determined by how tightly wound their spiral arms are and the luminosity of the bulge component, and which branch they lie on depends on the presence of a bar.

The third population of galaxies are known as lenticular galaxies, or S0s. They lie between spiral and elliptical galaxies, displaying similar traits to both, with clear photometric disks similar to spiral galaxies, but the quiescent red colours stereotypical of ellipticals.

Known as the Hubble tuning fork, this diagram led to ellipticals and S0s being defined as 'early-type', and spiral galaxies being termed 'late-type'. Current understanding is that, in fact, the stars in elliptical galaxies tend to be older than those in spiral galaxies, making this naming convention somewhat confusing, but, one of many quirks in the field of astronomy, the terms are still commonly used. These simple morphological classifications, while not without their problems, have been shown to correlate with many properties of galaxies, including mass, colour, gas content, average age, star formation, chemical composition and angular momentum.

At the simplest level, many galaxies appear to be composed solely of a bulge and a disk of varying proportions, the most basic examples of which are S0 galaxies. However, as our observational capabilities have increased it has become apparent that more

complex classification systems are necessary to fully describe the range of galaxy morphologies present in the universe around us. These complications partly arose due to uncertainties arising on the nature of the bulge component. Originally thought to resemble elliptical galaxies in structure, with steep central luminosity gradients, increasingly observations show that this is not the case, with bulges often displaying shallower luminosity gradients, occasionally even showing similar profiles to galaxy disks (Sérsic, 1963; Andredakis & Sanders, 1994; Andredakis, Peletier & Balcells, 1995; Courteau, deJong & Broeils, 1996; Carollo, 1998; MacArthur *et al.*, 2004). In addition, bulges characterised by a more boxy shape are now understood to be buckled bars viewed in projection (Kuijken & Merrifield, 1995; Bureau & Freeman, 1999). This variation in bulge morphologies, and presumably formation mechanisms, makes a single simple evolutionary scenario from late to early-types unlikely.

A related problem is that S0 galaxies appear not to be as structurally simple as first thought and in fact display a range of bulge-to-total luminosity ratios and frequently contain more complex structures such as bars and even spiral arms. Added complications arose from the difficulties in accounting for the effects of inclination, with face-on S0s appearing round and featureless, making them easy to mis-classify as elliptical galaxies. With the increasing availability of spatially-resolved spectroscopic information, Cappellari *et al.* (2011) proposed an updated classification system aimed at getting around these problems by incorporating kinematics, such that early-type galaxies are classified according to their rotation. Rotation-dominated galaxies, including spirals and S0s, are then classed as fast rotators and dispersion-dominated galaxies are classed as slow rotators. Spiral galaxies then branch off from early-type fast rotators, as shown in Figure 1.2.

The common thread in these evolution scenarios is the understanding that early-type galaxies, whether rotation-dominated or not, lie towards the end of an evolutionary path beginning with the disky star-forming galaxies which dominate the early universe, and ending with the bulge-dominated passive ‘red and dead’ galaxies, common in our local universe today. Exactly how this evolution takes place, however, is still not well understood.

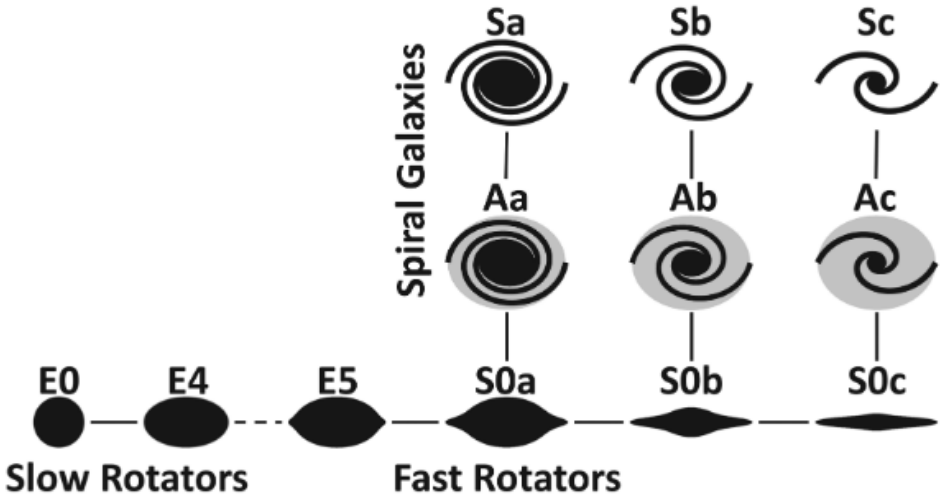


Figure 1.2: Hubble tuning fork updated by Cappellari *et al.* (2011) to include kinematic classifications.

1.2 Galaxy evolution: late-types to early-types

The bimodal nature of the galaxy population is clearly demonstrated by the distribution in colour–mass space, with a clear divide between the young, star forming population of the blue cloud, and the older, quenched population of the red sequence (Strateva *et al.*, 2001), as shown in Figure 1.3. The evolution of a galaxy is linked to its morphology, with indications that elliptical galaxies tend to have had their star-formation quenched rapidly, while disky galaxies evolve more gradually, with more slowly declining star-formation rates (e.g. Smethurst *et al.*, 2018). The method by which star formation ceases in galaxies is one of the most debated topics in the field of galaxy evolution. Many processes have been suggested as the culprit for this so-called quenching, and they can be broadly divided into two categories: internal processes and external processes. In the following sections, I will outline the most common theories attributed to each.

1.2.1 Internal Processes

The extent to which internal effects play a role in a galaxy tends to correlate with its physical properties, such as mass, morphology and angular momentum, each playing a role in enhancing or suppressing the various processes.

- **Stellar Feedback** The star formation rate of a galaxy can be regulated by super-

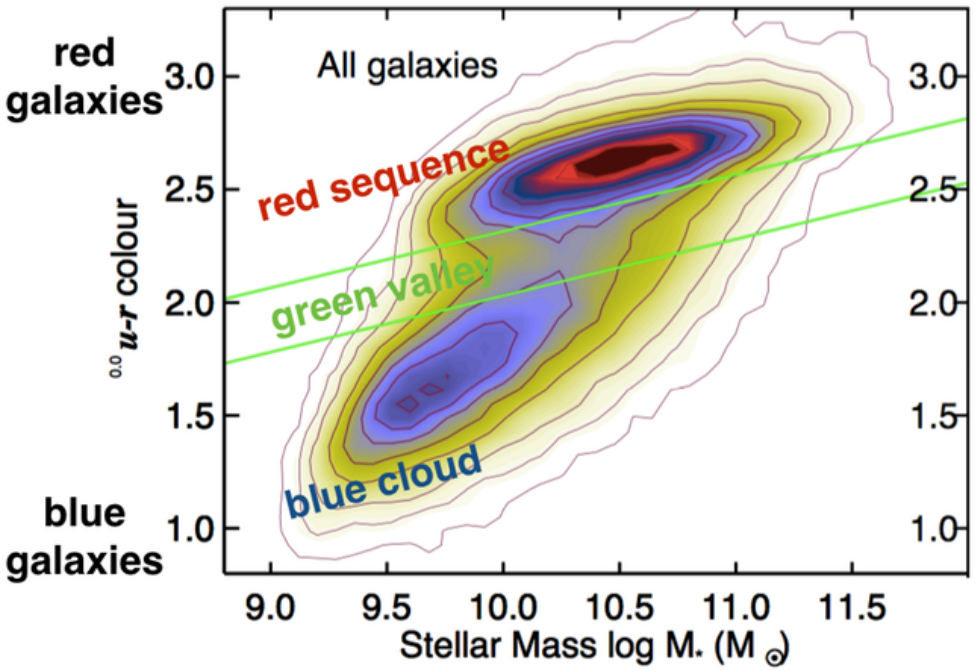


Figure 1.3: The galaxy colour-mass diagram from SDSS plus GALEX data. Image credit Schawinski *et al.* (2014)

novae, which can heat the surrounding inter-stellar medium (ISM) and therefore prevent the collapse of gas. In addition, galactic winds driven by supernovae have been shown to be able to remove a large fraction of gas from a galaxy (Larson, 1974; Efstathiou, 2000). Massive stars can also play an important role in feedback, producing radiation pressure and stellar winds which heat or remove gas and dust in the ISM (e.g. Hopkins, Quataert & Murray, 2012).

- **AGN Feedback** The active galactic nucleus of a galaxy can produce radiation, winds and jets which interact with the interstellar medium causing ejection or heating of the gas (Fabian, 2012). This helps to explain why, even when galaxies have an available supply of cold gas, they are not always undergoing star formation (e.g. Wong *et al.*, 2015).

- **Secular Evolution** The transfer of angular momentum in the disk can lead to migration of material into the centre of the galaxy, resulting in the build up of a bulge. This angular momentum transfer has been shown to occur via structures such as bars and spiral arms, resulting in a disky 'pseudo-bulge' (see Kormendy & Kennicutt, 2004, for a review).

1.2.2 External Processes

The environment a galaxy lies in has been demonstrated to have an effect on its evolution. This relationship is exemplified by the morphology–density relation, showing that the fraction of quenched elliptical and S0 galaxies rises with increasing local galaxy density (Dressler, 1980). Other correlations have also been found, with redder galaxies with lower star-formation rates found in denser regions of clusters (e.g Balogh *et al.*, 2004). Many methods have been shown to effect star-formation rates in dense environments, and it is likely that multiple processes play a role over a galaxy's lifetime.

- **Galaxy–galaxy interactions** With the hierarchical growth of structure now widely accepted in ΛCDM cosmology, it follows that the merging of galaxies most likely plays an important role in their evolution. Mergers have been shown to have a variety of effects on the resulting system, depending strongly on the mass ratio of the progenitors, referred to as 'minor' for very different masses and 'major' for similar masses, and on their gas content, classed as 'wet' for gas-rich (e.g. Mihos & Hernquist, 1996), and 'dry' for gas-poor collisions (e.g. van Dokkum, 2005). These collisions disrupt the orbits of the gas in galaxies, inducing starburst events which consume the gas, thus preventing future star formation. When galaxies interact repeatedly, but their velocity is too high to lead to a collision, the gravitational effects can result in asymmetry, tidal tails and bars, an effect known as 'harassment' (Moore *et al.*, 1996).

- **Galaxy–intra-cluster medium interactions** These include 'ram-pressure stripping' (Gunn & Gott, 1972) where cold gas is stripped from galaxies due to pressure from the intra-cluster medium. A variation on this is the 'strangulation' or 'starvation' scenario where hot, diffuse gas is stripped from the halo. This gas can no longer accrete onto the disk to replenish gas used for star formation, and star formation will therefore slow and eventually cease once the remaining gas has been consumed (Balogh *et al.*, 1999; Balogh, Navarro & Morris, 2000).

- **Accretion** Working against quenching scenarios, gas can also be accreted from the inter-galactic medium, along filaments of the cosmic web, fueling star formation in galaxies (see Kereš *et al.*, 2005, and refences within).

It is very likely that a galaxy will experience not just one, but many of the processes discussed here over its lifetime, both internal and external. One of the difficulties in studying galaxies is that we only have a single snapshot of a galaxy, enabling us to see signatures of the most recent events to affect it, but not every period of its history. Simulations are therefore valuable tools in understanding how multiple processes can affect a galaxy over its lifetime. For instance, Martig & Bournaud (2009) used simulations to demonstrate a process they term 'morphological quenching'. They show that if the bulge of a spiral galaxy is built up to a great enough extent, for example through external processes such as minor mergers or accretion, the disk will become stable against fragmentation and therefore star formation will cease; an interesting case of where external interactions can trigger internal effects.

1.2.3 Environment versus mass

While many properties of galaxies, including colour and morphology, have been shown to depend on environment, they also depend on stellar mass (e.g. Baldry *et al.*, 2006; Brinchmann *et al.*, 2004), most likely due to the mass-dependent efficiency of the internal quenching processes outlined in the previous section. Because massive galaxies preferentially reside in over-dense regions, it is difficult to tell whether or not environment plays a role independent of mass. Some studies indicate that both play some role in the evolution of the galaxy population, though the extent to which they contribute may depend on redshift (Bamford *et al.*, 2009; Peng *et al.*, 2010b).

With the increasing availability of integral field data, and therefore accurate kinematic measurements, the morphology-density relation was extended by Cappellari *et al.* (2011) to a 'kinematic morphology-density relation', demonstrating that the fraction of slow rotating elliptical galaxies increases sharply with increasing local density, along with the number of fast-rotating early-type galaxies, while the number of spiral galaxies falls. However, as seen for the classical morphology-density relation, when accounting for stellar mass this dependence becomes much weaker or even non-existent (Veale *et al.*, 2017; Brough *et al.*, 2017; Greene *et al.*, 2017). This widely-debated issue is often referred to as a key aspect of the 'nature versus nurture' problem.

1.2.4 Effects on the components of galaxies

The structure, or morphology, of a galaxy, is affected by the processes undergone throughout its lifetime. The various evolutionary scenarios outlined in the previous section will affect the constituent components in different ways, both in terms of their relative ages and metallicities, and their kinematics. For example, an S0 galaxy which arrived in its quenched state simply due to running out of gas, sometimes referred to as the faded spiral scenario, will look structurally and kinematically similar to a spiral galaxy, being most likely dominated by a regularly rotating disk. In contrast, a galaxy which has undergone a major merger event, or a series of minor mergers, will likely be very different structurally and kinematically to its progenitor spiral. Major merger events tend to build up large, dispersion dominated systems (Toomre, 1977), with the disk most likely completely destroyed, though recent simulations suggest that depending on how gas-rich the merger was the disk may survive or even be re-built (Hopkins *et al.*, 2009a; Querejeta *et al.*, 2015a). Minor mergers will also act to build up a dispersion-dominated bulge through disrupting the gas, causing infall and star formation in the central regions of the galaxy (Naab & Burkert, 2003; Bournaud, Jog & Combes, 2005; Hopkins *et al.*, 2009b). Simulations can, with increasing detail, help us understand how even subtle differences in a galaxy's evolution lead to differences within the components. Separating out the light from bulge and disk components and looking at their light profiles, stellar populations and kinematics can therefore provide key information on the processes the galaxy has undergone to reach its present state (e.g. Johnston *et al.*, 2012).

1.3 Bulge-Disk decompositions

A crucial step in understanding the formation history of a galaxy is knowing where and when its constituent stellar populations were formed. As a first approximation of this, photometric bulge-disk decompositions have long been used as a way of separating out the central and extended components in a galaxy. By comparing structural features of these components such as their effective radii and concentration, as well as their colours in order to infer information about their chemical compositions and ages, much

progress has been made in understanding their evolution. To this end, increasingly sophisticated softwares such as GALFIT (Peng *et al.*, 2002), GIM2D (Simard, 1998) and BUDDA (de Souza, Gadotti & dos Anjos, 2004) have been developed to formalize and automate the process of fitting such multiple components.

1.3.1 Photometric bulge-disk decompositions

Luminosity profiles of galaxies and their constituent components are commonly described by a Sérsic function (Sérsic, 1963), defined as

$$I(r) = I_e \left\{ -b_n \left[\left(\frac{r}{R_e} \right)^{1/n} \right] \right\}, \tag{1.1}$$

where $I(r)$ is the surface brightness at a given radius, R_e is the effective radius, n is the Sérsic index, I_e is the intensity at the effective radius, and b_n is a function of the Sérsic index such that $\Gamma(2n) = 2\gamma(2n, b_n)$. where Γ and γ represent the complete and incomplete gamma functions, respectively. The shape of this function is determined by the Sérsic index, as shown in figure 1.4. For disks a Sérsic index of $n = 1$ is generally used, correponding to an exponential profile (Kormendy, 1977), while for the bulge the Sérsic index is more variable. While historically a de Vaucouleurs profile of $n = 4$ was commonly used (de Vaucouleurs, 1948), with advances in imaging capabilities it was found that in fact Sérsic indices could be anywhere from $n = 1$, similar to the disk, to $n \geq 4$ as found for high-mass ellipticals (Andredakis, Peletier & Balcells, 1995; de Souza, Gadotti & dos Anjos, 2004). Recent studies therefore tend to adopt a general Sérsic profile where n is left free to vary (e.g. Simard *et al.*, 2011).

1.3.2 Trends with bulge-to-total ratio

Studies into the structural parameters of bulges and disks have provided some interesting insights. The bimodality in the relationship between the mass and colour of galaxies, dividing galaxies into the star-forming blue cloud and quenched red cloud [see Section 1.2], has been shown to correlate with the physical structure of the galaxies and their components, in particular the predominance of the bulge, or the bulge-to-total flux ratio (e.g. Fang *et al.*, 2013). The blue cloud is dominated by rotationally

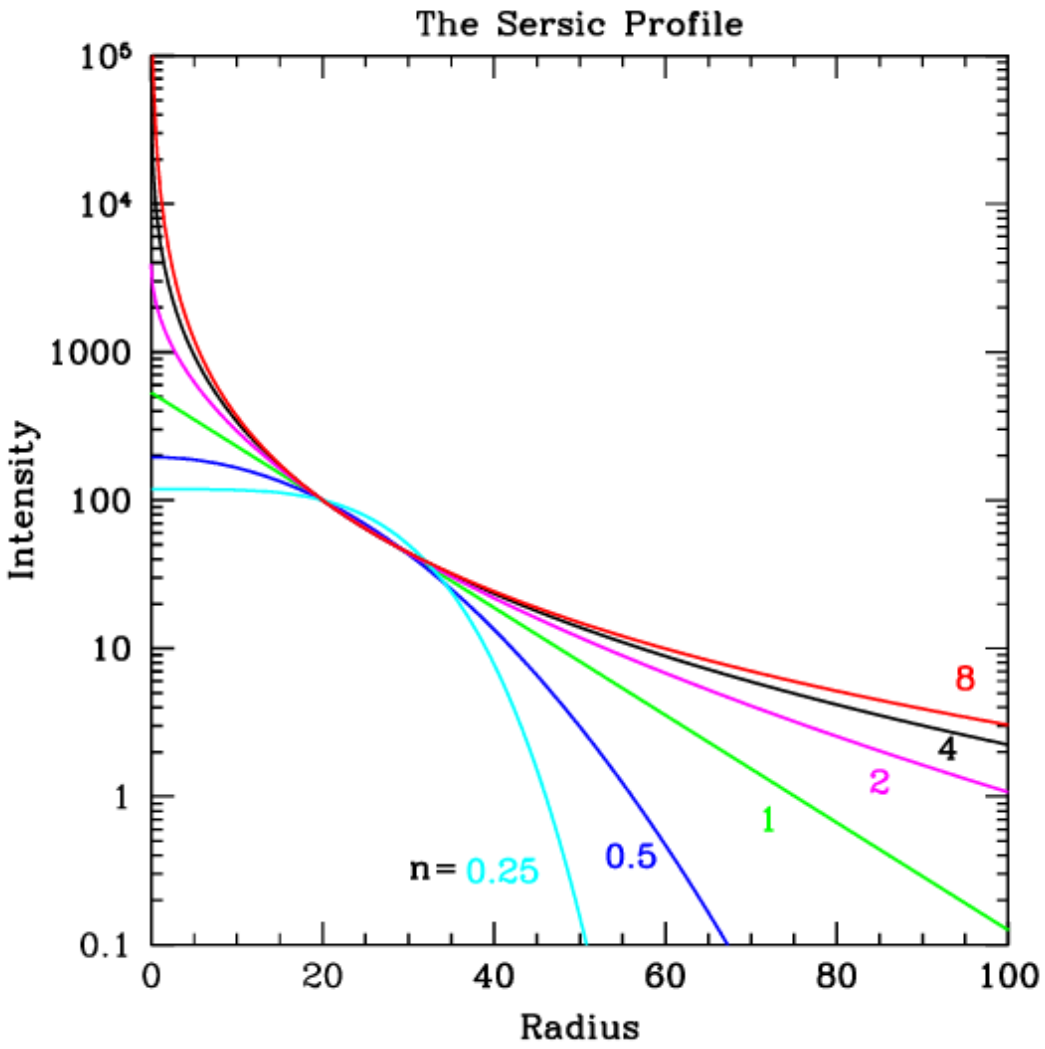


Figure 1.4: Sérsic function for various Sérsic indices at fixed R_e and b_n. (Peng *et al.*, 2010a)

supported disks while the red cloud are predominantly classified as spheroidal, albeit with some interesting crossovers. This has led to the suggestion that the bimodality in galaxy properties, both in colour and in structural properties such as the luminosity–size plane and the luminosity–surface-brightness plane (Blanton *et al.*, 2003; Driver *et al.*, 2005) is not due to two galaxy populations, but due to two components with fundamentally different characteristics, combined in different measures (Driver *et al.*, 2006).

This idea has also become prevalent in the studies of galaxy kinematics. Early work on the formation of galaxies highlighted the importance of three quantities in describing galaxies: mass, M, angular momentum, J, and energy, E. Observationally, the specific

angular momentum $j_* = J/M$, defined as

$$j_* = \frac{\sum F_i R_i \mid V_i \mid}{\sum F_i} \tag{1.2}$$

where F_i, R_i and V_i are the flux, radius and velocity of the i^{th} spatial point in the galaxy, provides a convenient way of analysing the rotational velocity of systems. Fall (1983) demonstrated the relation between stellar mass, M_*, and j_*, which showed that both elliptical and spiral galaxies obey power-law scaling relations of the form $j_* \propto M_*^{\alpha}$, where $\alpha = 0.6 \pm 0.1$, but with elliptical galaxies offset to lower values of j_* for a given mass. This is remarkably close to the relation expected from galaxy formation theory, where the galactic halos formed through hierarchical clustering obey the scaling relation $j_{\rm halo} \propto M_{\rm halo}^{\alpha}$ with $\alpha = 2/3$, and baryons retain the angular momentum of their dark matter halos as they collapse to the halo centre (Fall & Efstathiou, 1980).

More recent studies, both observational and in simulations, have shown that the offsets from the $M_* - j_*$ relation correlate very well with the bulge-to-total luminosity ratio (Romanowsky & Fall, 2012; Obreschkow & Glazebrook, 2014; Cortese *et al.*, 2016; Sweet *et al.*, 2018; Posti *et al.*, 2018), as shown in Figure 1.5. This points towards a scenario in which bulges and disks follow their own kinematic relations, with the global properties of the galaxy being determined by the relative contribution of each.

A similar dependence can be seen in the stellar spin parameter, λ_R, with the position of a galaxy on the $\lambda_R - \epsilon$ plane depending on the bulge-to-total ratio, as seen in Figure 1.6 for the ATLAS^{3D} sample (Krajnović *et al.*, 2013). This again points towards the bulges and disks displaying distinct kinematic parameters, combining to determine the global properties of the galaxy.

1.3.3 Properties of bulges and disks

Photometric decompositions provide us with structural properties of galaxy components, and these are often used to understand and catagorise galaxies. This is especially true for galaxy bulges, with the Sérsic index often used as a way of separating out pseudo-bulges from classical bulges. With flatter light profiles, pseudo-bulges are expected to be more disk-like in nature, most likely forming through gradual secular evolution processes in the disk (see Kormendy & Kennicutt, 2004, for a review), while

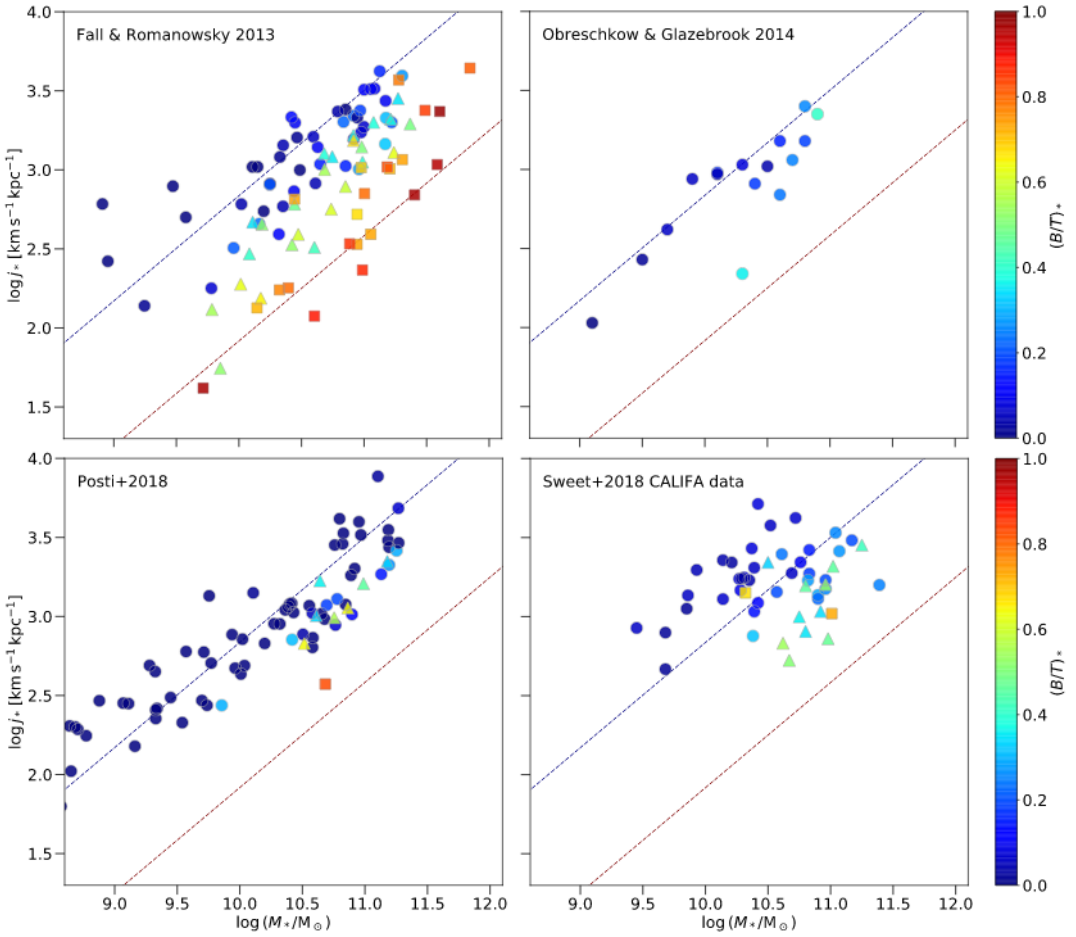


Figure 1.5: The $M_* - j_*$ relation for several studies, both observational and from simulations, showing the correlation in the scatter of the relation with the B/T flux ratio. (Fall & Romanowsky, 2018).

classical bulges have steep light profiles and shapes similar to elliptical galaxies and are likely to be dispersion-dominated systems formed through mergers (Hopkins *et al.*, 2009a) or via dissapative collapse of protogalactic gas clouds (Eggen, Lynden-Bell & Sandage, 1962). However, attempts to understand the extent to which photometric parameters are accurate proxies for kinematic properties of components have provided mixed conclusions. While Fabricius *et al.* (2012) found that low Sérsic index bulges tend to be more rotationally supported, other studies have found no evidence of this (Méndez-Abreu *et al.*, 2018; Falcón-Barroso *et al.*, 2003).

Thob *et al.* (2018) compare kinematic and photometric parameters for galaxies in the EAGLE simulation, and conclude that kinematics provide a better diagnostic of whether a galaxy is star-forming or passive than photometric properties. They also find that the photometric properties, such as the flattening of a galaxy, do correlate

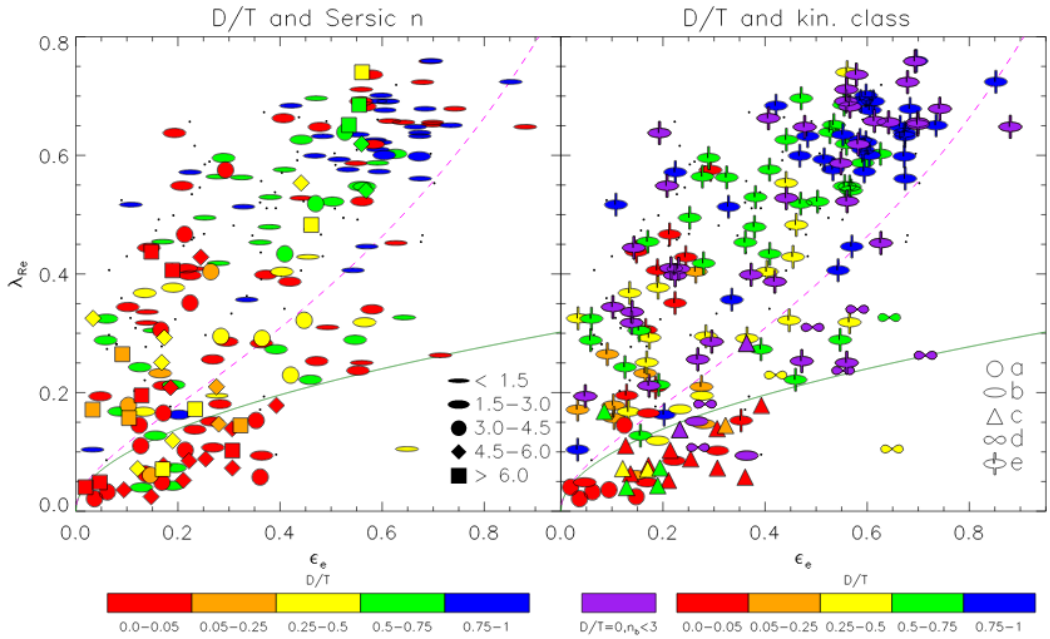


Figure 1.6: λ_R vs. ellipticity for the ATLAS^{3D} sample, coloured by disk-to-total ratio with symbols representing varying Sérsic index on the left, and kinematic class on the right. (Krajnović *et al.*, 2013)

with kinematic properties but with a large scatter, which in turn correlates with the anisotropy of the velocity dispersion and the bulge-to-total ratio.

The common use of these photometric parameters in classifying galaxies and inferring their formation scenarios means that understanding to what extent they correspond with the intrinsic properties, of both galaxies as a whole and individual components, is increasingly important.

Studies into the stellar populations of bulges and disks have also yielded mixed results, particularly for early-type galaxies, finding older bulge components than disks (Caldwell, 1983; Bothun & Gregg, 1990; Norris, Sharples & Kuntschner, 2006), similar ages in both components (Peletier & Balcells, 1996; Mehlert *et al.*, 2003; Chamberlain *et al.*, 2011), and older disks than bulges (Fisher, Franx & Illingworth, 1996; Bell & deJong, 2000; Kuntschner, 2000; MacArthur *et al.*, 2004). Studies specifically into S0 galaxies residing in clusters tend to find predominantly younger bulges than disks (Bedregal *et al.*, 2011; Johnston *et al.*, 2012), indicating that these S0s are most likely the evolutionary result of gas stripping from spiral galaxies, in which the "last gasp" of star formation occurred in their central regions, enhancing the bulge light. Fraser-McKelvie *et al.* (2018) find that there appears to a be a bimodality in the populations of

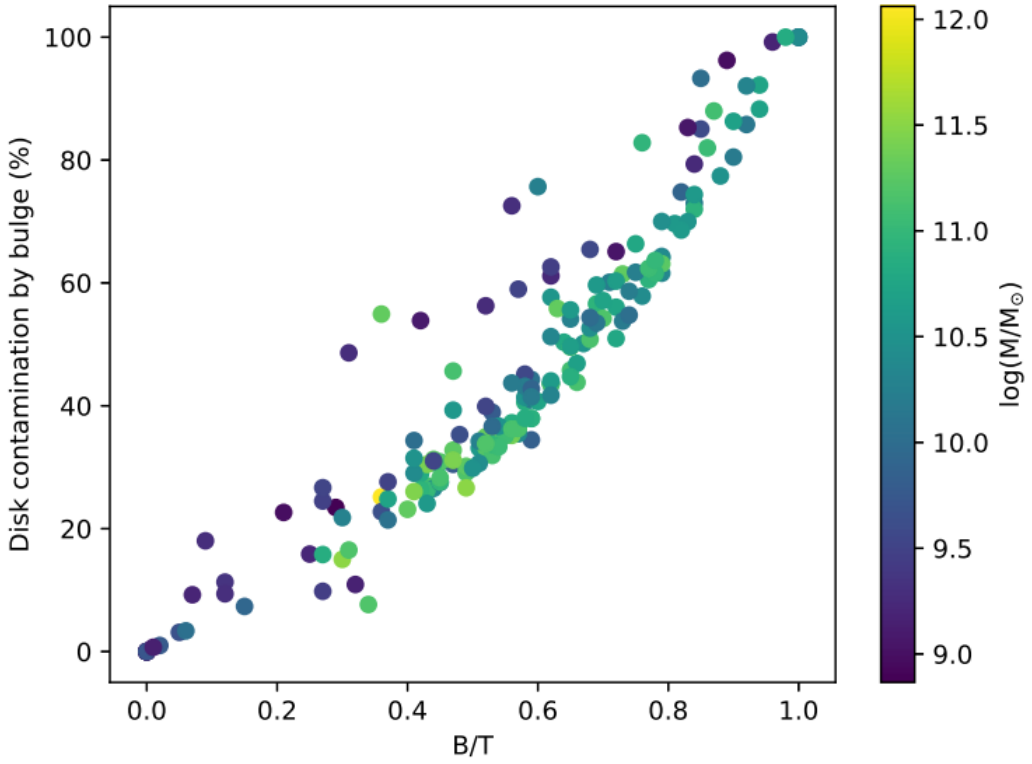


Figure 1.7: Contamination of disk with varying bulge-to-total ratio for S0 galaxies from the MaNGA survey.

the components, with high mass S0s having older bulges than disks, while the opposite is true for low mass. They also find no trend with environment, though their sample does not extend to high density cluster environments.

The difficulties in understanding the properties of individual components is partly due to the difficulties in separating them. Defining spatial bulge and disk regions of a galaxy and determining the properties within each still often suffers from contamination, particularly in the disk regions of bulge-dominated galaxies. Fraser-McKelvie *et al.* (2018) looked at a sample of S0 galaxies from the MaNGA survey, defining bulges as the area within one bulge effective radii, and disks as the area outside two bulge effective radii, and found that for large bulge-to-total (B/T) ratios, the disk is heavily contaminated by bulge light, as shown in Figure 1.7.

Untangling the stellar populations and kinematics of each component in a more rigorous way and determining their properties individually is an obvious next step in understanding and making meaningful comparisons between the properties of these components.

1.3.4 The distinctness of bulges and disks

While bulge–disk decompositions have long been used to describe the structure of galaxies, whether they represent individual stellar populations with separable kinematics remains unclear. The original picture of galaxy structure as outlined by Hubble, with a central spheroidal bulge with a de Vaucouleurs law surface brightness profile (de Vaucouleurs, 1948), combined with a more extended exponential disk (Freeman, 1970), fits nicely with a dynamical picture in which part of the system consists of stars on largely random orbits, resulting in a spheroidal component with little net rotation, while the remainder is made up of stars in well-ordered rotation, producing a highly-flattened disk. Thus, bulge–disk decomposition offered a neat and convenient way of separating the different parts of a galaxy, and hence exploring the formation histories of these dynamically-distinct features.

However, as the level of detail in observations has increased, evidence has appeared indicating that bulges and disks are not as simple and distinct as was first thought. With many bulges displaying disk-like features such as spiral structure, inner disks and bars, and often following shallower surface brightness profiles than originally thought, such developments have blurred the distinction between disks and bulges, and thus raised the question of whether the components obtained by decomposing a galaxy photometrically really represent individual stellar populations with distinct kinematics, or whether these decompositions are just a convenient way of parameterising galaxy light distributions.

The key to addressing this question is provided by spectra: since their absorption lines contain information on both stellar kinematics and populations, analysis of spectral data can in principle be used to test whether the individual bulge and disk components form coherent distinct entities in terms of their dynamics and stellar properties, and hence whether the decomposition makes any intrinsic physical sense.

1.3.5 Spectroscopic bulge-disk decomposition

To determine whether bulges and disks are indeed distinct, and to truly understand the role that they play individually within the galaxy, we must be able to separate out the

stellar populations within a galaxy, and extract ages, metallicities, and kinematics. To determine these parameters, however, we need spectral information. Johnston *et al.* (2012) developed a method of separating out bulges and disks of S0 galaxies using long-slit spectroscopy, which provides a one-dimensional cut through the light distribution of a galaxy. By decomposing these profiles into bulge and disk components at each wavelength provided by the spectrograph, they produced a direct measure of the amount of bulge and disk light as a function of wavelength; in other words, they extracted separate bulge and disk spectra, which would allow the stellar populations in these components to be compared. More recently, they have generalised the technique to analyse integral-field unit (IFU) data, which produce spectra right across the face of a galaxy, and hence generate a three-dimensional data cube comprising a spectrum at each location on the sky. By applying GALFITM (Häußler *et al.*, 2013), a modified version of GALFIT, to an "image slice" through the data cube at each wavelength, it is possible to calculate the relative contributions of bulge and disk at that wavelength, and hence calculate a separate spectrum for each component as before, but now based on a more reliable two-dimensional image rather than just a one-dimensional cut (Johnston *et al.*, 2017).

This decomposition method allows ages and metallicities to be extracted for the bulges and disks, yielding some very interesting results, but it is not well suited to addressing the question of the distinctness of the components. When the effective radii of the components are fixed, as in Johnston *et al.* (2017), it reduces each component to a single spectrum, losing most of the information relating to variations with position in the galaxy, which would tell us how homogeneous each component is. In addition, it discards all the kinematic information in the spectra, even though some of the clearest defining features of bulges and disks are related to their distinct dynamical properties [see Cappellari 2016 for a review].

Spectroscopic decomposition methods utilising the kinematics have been developed in order to separate out kinematically decoupled disks (Johnston *et al.*, 2014; Coccato *et al.*, 2015), allowing the kinematics and stellar populations of the two disks to be extracted simultaneously. This is, in general, significantly easier than separating bulges and disks due to the large difference in velocities between the stellar populations of

counter rotating disks, making spectral lines relatively simple to deconvolve. In contrast, bulges and disks are expected to display similar kinematics, making it difficult to untangle the spectra of each.

Bender (1990) found that the asymmetric shape of the line-of-sight velocity distribution along the major axis of disky elliptical galaxy NGC 4621 was best explained by the presence of two gaussians with different mean velocities and velocity dispersions, i.e. a bulge and a disk component. Subsequent studies such as Scorza & Bender (1995) used this effect to explore the kinematics of bulge and disk components for a wider sample of disky ellipticals. However, this approach is limited in terms of the spatial information, looking only at the behaviour along the major axis of the galaxy, and does not provide information on the stellar populations of the components, which is also a key element in determining whether the components are truly distinct.

In this thesis we have built on this work, developing a method to extract ages, metallicities and kinematics for individual components within galaxies using spectroscopy, while still conserving spatial information. This allows us to determine the fundamental properties of the components, and the role they play within a galaxy.

1.4 Thesis Structure

To describe this work, the thesis is set out as follows. In Chapter 2 I present the data and sample of galaxies used in this thesis. In Chapter 3 I will introduce a method of spectroscopic bulge-disk decomposition and use it to address whether bulges and disks are truly distinct components. In Chapter 4 I then apply this spectroscopic decomposition to a large sample of early-type galaxies. By separating stellar components that are spatially and kinematically segregated, with distinct chemical compositions and age distributions, we can extract observational kinematic properties such as λ_R and j_*, and stellar population parameters, such as age and metallicity, for the bulges and disks separately. Chapter 5 then uses simple dynamical modeling to determine dynamical properties of bulges and disks in order to compare to the results of the spectroscopic decomposition, and also to determine if bulges and disks have fundamentally different dynamical properties. Finally, in Chapter 6 I present my conclusions and their

implications along with potential future applications of the method.

Chapter 2

Data: Integral Field Spectroscopy

"It is a capital mistake to theorize before one has data."

- Sherlock Holmes

In this chapter we discuss the reasons for using integral field spectroscopy for this work, as well as the surveys and sample selections used throughout the rest of this thesis.

2.1 Integral Field Spectroscopy

The key in separating individual stellar populations lies in their spectra. Spectral indices provide key information on the stellar populations present in a system, allowing the determination of their age and levels of heavy elements present. In addition, the Doppler shift in the position of absorption lines, and the amount by which they are broadened tell us how the stars are moving within a galaxy. This combination of information on the chemical composition and the kinematics of galaxies has led to some of the most important discoveries in the field of galaxy evolution, particularly when used in large surveys such as the Sloan Digital Sky Survey (SDSS), which allow for meaningful statistical analysis. By obtaining spectra of large numbers of galaxies, SDSS succeeded in reinforcing old, and determining new, scaling relations linking

mass, luminosity, kinematics, star formation rates and chemical composition. Key examples include the colour-bimodality (Strateva *et al.*, 2001; Balogh *et al.*, 2004), colour–density relation (Hogg *et al.*, 2003; Blanton *et al.*, 2005), the mass–metallicity relation for stars (Thomas *et al.*, 2010; Johansson, Thomas & Maraston, 2012) and gas (Tremonti *et al.*, 2004), the Fundamental Plane (Bernardi *et al.*, 2003), the dependence of star formation on stellar mass (Kauffmann *et al.*, 2003) and the star formation rate vs. stellar mass relation (Brinchmann *et al.*, 2004; Salim *et al.*, 2005; Wuyts *et al.*, 2011).

Obtaining spectra, however, is observationally expensive, and therefore for a long time only a single spectrum was obtained per galaxy, as for surveys such as SDSS, zCOSMOS (Lilly *et al.*, 2007) and the 2DF survey (Lewis *et al.*, 2002). While expanding greatly on our knowledge, as illustrated by the studies mentioned previously, this meant that our understanding of galaxies was primarily based on information from the integrated galaxy light, neglecting information on the spatial distribution of galaxy properties, both with radius and azimuthally. This is especially problematic when trying to understand the properties of individual components, as the central light will be dominated by the bulge and neglect the outer disk-dominated regions. This also leads to difficulties in dealing with aperture losses, with the diameter of the fibre used corresponding to different physical scales at different redshifts.

The development of long-slit spectroscopy provided a way to obtain spatially resolved spectroscopic properties. By moving a spectrograph along the major axis of the galaxy, kinematics and stellar populations could be obtained both in the central regions where the bulge dominates and the outer disk-dominated regions. However, long slit spectroscopy is still observationally expensive and does not allow for the analysis of more complicated galaxy structures, such as spiral arms, which do not necessarily have the same properties across all axes.

Integral-field unit (IFU) spectroscopy combines spectral information with full spatial information, providing spectra of a galaxy across its face. This combination allows morphological features of galaxies, which have long been used to understand and classify various galaxy types, including complex structures such as spiral arms and bars, to be compared to the detailed kinematic and compositional information made available

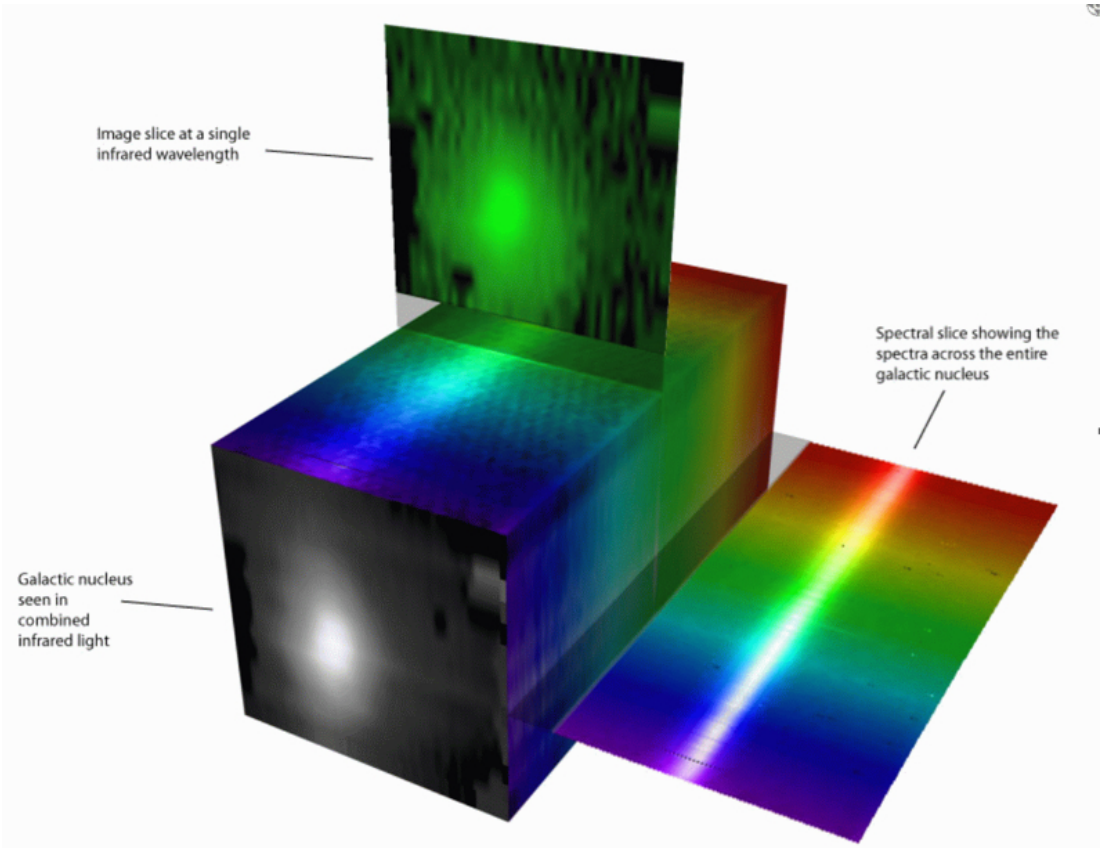


Figure 2.1: An IFU data-cube: provides a spectrum at each spatial point in the galaxy, and therefore an image of the galaxy at each wavelength step. Image credit: Stephen Todd (ROE) and Douglas Pierce-Price (JAC)

through spectra. By positioning galaxies on bundles of optical fibres such that light from different parts of the galaxy is channelled into separate fibres, or by using an image-slicer, each part of the galaxy can be passed through a spectrograph, producing its own individual spectrum. These spectra can then be combined into a "data-cube", with a spectrum for each spatial point in the galaxy, or, thought of in another way, an image of the galaxy at each wavelength (see Figure 2.1 for a schematic).

There are now an expanding number of IFU projects, either ongoing or completed, aiming to address a variety of science goals. SAURON (de Zeeuw *et al.*, 2002) and ATLAS^{3D} (Cappellari *et al.*, 2011) surveyed 260 early-type galaxies in the nearby universe over a relatively narrow wavelength coverage (4800-5380Å) and focused exclusively on early-type galaxies. The DiskMass survey (Bershady *et al.*, 2010) targeted 146 nearly face-on disk galaxies to study stellar and gas kinematics. The VENGA survey (Blanc *et al.*, 2013) used a fibre-fed integral field spectrograph, VIRUS-P on the 2.7-m Telescope at McDonald Observatory, and targeted 30 nearby spiral galaxies.

The CALIFA (Calar Alto Legacy Integral Field spectroscopy Area) survey (Sánchez *et al.*, 2012) used the PPak instrument and targeted 600 nearby galaxies selected to sample a wide variety of stellar masses and star formation rates. Coming at the problem from a more quality-over-quantity philosophy are more sophisticated instruments such as MUSE on the VLT and the upcoming WEAVE on the WHT, which allow IFU observations of small numbers of galaxies to be undertaken in exquisite detail.

While each of these surveys has been ground breaking in its own way, even CALIFA with its relatively large sample size does not allow for SDSS-like studies of galaxies. When binning galaxies by stellar mass, environment, and morphology, the sample size necessary for significant statistics is quickly lost (e.g González Delgado *et al.*, 2016). The main limitation for the sample size is that all these surveys are targeting galaxies one by one and are therefore inefficient at building up a large statistical sample. Both the ongoing MaNGA (Mapping Nearby Galaxies at APO [1]) survey (Bundy *et al.*, 2015), and the SAMI [2] Galaxy survey (Bryant *et al.*, 2015) aim to address this issue by making multiple simultaneous observations. SAMI aims to observe 3400 galaxies in total, and has already produced many interesting science results. MaNGA is even larger, aiming to observe 10,000 galaxies in the nearby universe. We choose here to use data from both the CALIFA survey and the MaNGA survey. This was partly due to timing, with the MaNGA survey, which provides the largest sample of IFU observations, not yet fully ready on the onset of this work. It also, however, demonstrates the versatility of the method presented, being easily adaptable to multiple IFU surveys.

2.2 CALIFA

In Chapter 3 we use data from the recently-completed CALIFA survey, which obtained spatially-resolved spectroscopy of 600 nearby ($0.005 \leq z \leq 0.03$) galaxies over a wide range of morphologies, selected from the Sloan Digital Sky Survey (SDSS) photometric catalogue. They were selected to cover the full colour–magnitude diagram down to $\mathrm{M_B} \sim -18$ mag, and the observations were taken using the PMAS/PPAK integral field spectrophotometer, mounted on the Calar Alto 3.5m telescope.

[1] Apache Point Observatory

[2] the Sydney-Australian-Astronomical-Observatory Multi-object Integral-Field Spectrograph

The survey provides spectra in two setups: the V500 setup in the red, covering a wavelength range of 4300–7000Å, with spectral resolution $\mathrm{R} \sim 850$ and the V1200 setup, which yielded spectra with a wavelength range of 3650–4840Å, $\mathrm{R} \sim 1650$. For the work presented in this thesis we use the V1200 setup due to its high spectral resolution, with a FWHM of 2.3 Å corresponding to a velocity resolution of ~ 80 km s^{-1} at the blue end and ~ 60 km s^{-1} at the red end of the spectrum. The large field-of-view (> 1 arcmin^2) of PPAK provides good coverage, allowing larger structures such as disks and spiral arms to be covered. A full description of the data can be be found in García-Benito *et al.* (2015).

The CALIFA sample was selected from the SDSS DR7 photometric catalog (Abazajian *et al.*, 2009), ensuring the availability of multi-band photometry, and its footprint is therefore almost identical to that of SDSS. The CALIFA "mother sample" of 937 possible targets was selected through a small set of selection criteria, and the actual targets were then selected from this sample according to their visibility such that the final CALIFA sample consists of a subset of ∼2/3 of the mother sample.

CALIFA has produced many results so far, such as the metallicity gradient for star-forming galaxies (Sánchez *et al.*, 2014), the spatially-resolved evolution of galaxies (Pérez *et al.*, 2013), the resolved star formation main sequence (Cano-Díaz *et al.*, 2016; González Delgado *et al.*, 2016) and the spatially-resolved stellar mass-metallicity relation (González Delgado *et al.*, 2014).

2.2.1 Sub-sample selection

For our pilot work establishing the viability of a spectroscopic decomposition method, we needed a few classic text cases. From the CALIFA sample, we therefore selected three field S0 galaxies: NGC 528, NGC 7671 and NGC 6427. The SDSS colour images of these galaxies are shown in Figure 2.2, and the galaxies properties are summarised in Table 2.1. With their simple structure, all containing clear bulge and disk components and no visible dust, spiral structure or bar, they make good first test examples of such a bulge–disk decomposition method. They are also all fairly massive galaxies, meaning they are luminous and their structure should therefore be fairly easy to pick out. They were selected as isolated galaxies using the classification provided by CALIFA, the

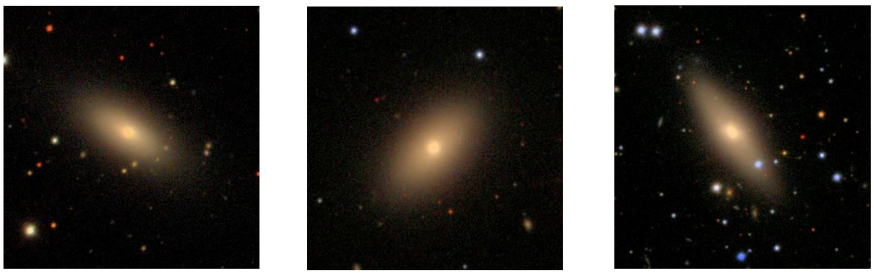


Figure 2.2: SDSS images of the three test galaxies over the CALIFA field of view; from left to right NGC 528, NGC 7671 and NGC 6427.

Galaxy	Kmag	$\mathrm{M}/\mathrm{M}_{\odot}$	I(°)	Distance modulus
NGC 528	-24.36	1.5×10^{11}	70	34.24
NGC 7671	-24.05	5.9×10^{10}	75	33.49
NGC 6427	-23.43	4.0×10^{10}	90	33.91

Table 2.1: Absolute magnitude, stellar mass (converted from K-band magnitude using eq.(2) of Cappellari 2013), inclination ($i = 0$ for a face-on galaxy) and redshift distance modulus (Makarov *et al.*, 2014) of galaxy sample.

details of which are presented in Walcher *et al.* (2014). Selecting this Hubble type and environment also allows us to compare and contrast the result with the previous analysis by Johnston, Aragón-Salamanca & Merrifield (2014) in their study of cluster S0s.

In order to fully determine the strengths and limitations of the method, we have chosen to explore the decomposition of one galaxy, NGC 528, in particular detail. At an inclination of ~ 70 degrees, it clearly displays both bulge and disk, while still ensuring that enough of any rotational motion is projected into the line of sight to be detected. It was also chosen for its brightness: it has a K-band absolute magnitude of $\mathrm{M}_{\mathrm{K}} \approx -24.36$ (Skrutskie *et al.*, 2006); using eq.(2) of Cappellari (2013) this luminosity can be converted into a large stellar mass of $\mathrm{M}_{*} \approx 1.5 \times 10^{11} \mathrm{M}_{\odot}$, ensuring that any kinematic structure will be well resolved with the CALIFA spectral resolution.

2.3 The MaNGA Survey

The MaNGA Survey is the largest integral field survey to-date, aiming to obtain IFU spectroscopy for ∼10,000 nearby galaxies up to $z = 0.15$ (Yan *et al.*, 2016a) by 2020. It is a project of SDSS IV (Blanton *et al.*, 2017), using the 2.5m telescope at Apache

Point Observatory (Gunn *et al.*, 2006) and BOSS spectrographs (Smee *et al.*, 2013). The data cubes cover a wide wavelength range of 3600–10300Å, with a spectral resolution R$\sim$2000, corresponding to a median velocity resolution of 70 km/s, and a spatial resolution of 2.5", both similar to the CALIFA survey. The survey aims to observe a luminosity-dependent, volume-limited sample of galaxies above a stellar mass of $\mathrm{M}_* = 10^9\mathrm{M}_\mathrm{o}$, with a roughly flat log($\mathrm{M}_\star$) distribution (Law *et al.*, 2015; Wake *et al.*, 2017). Because of this, more high mass galaxies are observed than is representative of the actual galaxy population in the universe, so the galaxies are also assigned a weight such that they are up or down-weighted depending on their under or over-representation. This allows meaningful statistical analysis to be done on what is then a representative sample of galaxies in the local universe.

The survey includes a 'primary' sample, consisting of about 50% of the targets, with full spatial coverage out to $\sim 1.5R_e$. There is also a 'colour-enhanced' sample, to balance to colour distribution at a given stellar mass, which, together with the primary sample, constitutes the 'Primary+' sample, making up 67% of the targets. The remaining $\sim 33\%$ makes up the 'secondary' sample, with a coverage out to $\sim 2.5R_e$.

By combining multiple fibre bundles across a field in the sky, multiple galaxies can be observed simultaneously, reducing the time needed to observe large numbers of galaxies compared to long-slit spectroscopy. There are various IFU sizes with a distribution optimised to match the size and density of the targets, ranging from 127-fibre IFUs of 32 arcseconds to 19-fibre IFUs of 12 arcsecond diameter.

The raw data is reduced by a data reduction pipeline (Law *et al.*, 2016; Yan *et al.*, 2016b) and made available as a final data-cube for each galaxy, with three dimensions: two spatial and a third spectral dimension. This data is released to the MaNGA collaboration in stages, referred to as MaNGA product launches (MPLs), as the data becomes available, and later to the public. In this work we use data from the 6th MaNGA product launch (MPL-6), consisting of ~ 4700 galaxies. Final products of the data are also made available through the MaNGA Data Analysis Pipeline (DAP), such as spectral indices and kinematics. These products have not been utilised in this work however, since in order to obtain parameters for the individual components we must perform our own bespoke analysis.

The key science questions the survey aims to address are:

- How galactic disks grow through accretion.
- The roles of stellar accretion, major mergers, and secular evolution processes in the present-day growth of galactic bulges and ellipticals.
- How star formation is regulated and shut down by internal and/or external processes and the dependence on environment.
- How mass and angular momentum is distributed across galaxy components and what effect this has on the components through time.

All of these goals, and particularly the 2nd and 4th, are very relevant to the work undertaken in this thesis, making the MaNGA survey an excellent place to acquire the necessary data.

2.3.1 Sample Selection

To select a sample of early-type galaxies, we use the Galaxy Zoo 2 catalogue (Lintott *et al.*, 2011; Willett *et al.*, 2013), which provides statistics on galaxy characteristics voted for by the public for SDSS galaxies. By selecting all objects with 'smooth' vote fraction > 0.7 (Willett *et al.*, 2013), with the vote fractions debiased to account for redshift-dependent bias as described in Hart *et al.* (2016), we rule out spiral and irregular galaxies while keeping all early-type galaxies including lenticulars and ellipticals. We also remove galaxies with bars (bar fraction > 0.7) so as to avoid more complicated kinematics, leaving 821 galaxies in our sample. Additional cuts are made throughout the decomposition process in order to retain galaxies with significant bulge and disk components and sufficient spatial variations after binning the data-cubes into high S/N bins. These cuts consist of:

- removing galaxies which, once binned to S/N=30, contain fewer than 20 bins. This removes the largest number of galaxies, predominantly low mass galaxies, from the sample.

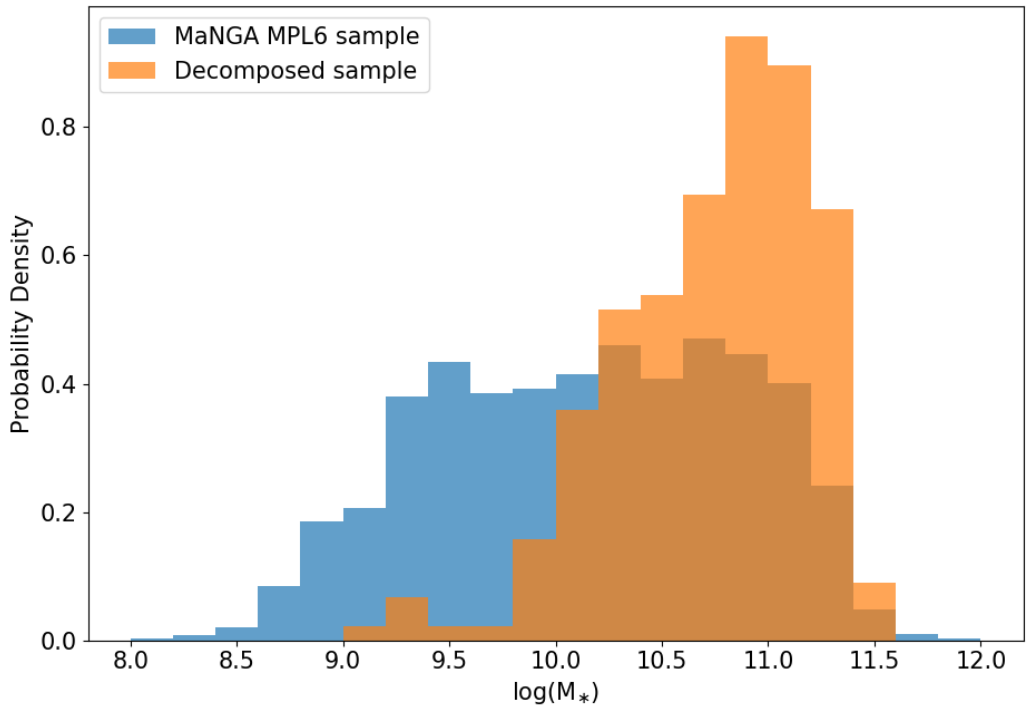


Figure 2.3: Mass distribution of the final decomposed sample of galaxies and of the full MaNGA MPL-6 sample.

- removing galaxies where either the bulge or the disk never contributes more than 5 bins with flux greater than 30% of the total flux. This is similar to taking a bulge-to-total flux ratio cut, with all galaxies removed have B/T > 0.9 or B/T < 0.1.

- removing galaxies where the decomposed disk component is kinematically classed as a slow-rotator. This will happen when the spectroscopic decomposition fails, producing very noisy kinematic maps with therefore no ordered rotation.

These cuts tends to remove low-mass galaxies which do not have sufficient S/N, unfortunately preventing this work from comparing galaxy properties over a large range of mass. However, the number and quality of IFU surveys is only increasing, and we hope that in the future it will be possible to extend the method presented in this thesis to a wider range of galaxies. These cuts are described and justified in detail in Chapter 4 and the mass distribution of the final sample, along with the distribution of the MaNGA MPL6 sample, is shown in Figure 2.3.

While superior in spectral resolution and sample size to CALIFA, the MaNGA survey

has lower spatial resolution. This can cause complications when looking at individual components, since bulges can have effective radii smaller than the FWHM of the observations. This can result in the properties being effectively smeared out across the bulge, affecting important spatial variations in the velocity and velocity dispersion which determine kinematic parameters. We do tests to assess the significance of this issue, which are discussed in Chapter 4. IFU observations provide us with an unprecedented view into the structure and composition of galaxies, and are likely to only become more widely used in the future. Developing methods in order to best exploit the wealth of information made available through this data is therefore crucial. We hope that the work presented in this thesis contributes in a meaningful way to this goal.

Chapter 3

Spectroscopic decomposition: the distinctness of bulges and disks

“ They seem so twinkle-still, but they never cease
Inventing new spaces and huge explosions
And migrating in mathematical tribes over
The steppes of space at their outrageous ease.”

– Stars and Planets, Norman MacCaig

Bulge-disk decompositions have long been used as a way of describing and parameterising the light profiles of galaxies. However, whether bulges and disks are composed of different stellar populations with their own kinematics is not clear. In this chapter, we therefore attempt a new approach to decomposing galaxies into bulge and disk components, which retains both the kinematic and stellar population information, and allows freedom for the properties of each component to vary with position, subject only to the global constraint that the relative fluxes of bulge and disk component at each location match those produced by image decomposition. Thus these models, by construction, reproduce the bulge and disk components of the conventional photometric image fitting technique, but also fit the full spectral data cube for the galaxy. By investigating the stellar kinematics and populations of the resulting fitted components, and how they

vary with position, it will be possible to test whether the imposed image decomposition produces coherent underlying physical sub-systems. We apply this decomposition to three sample galaxies selected from the CALIFA survey, the details of which are described in Chapter 2.

3.1 The Method

3.1.1 Photometric bulge–disk decomposition

To perform the initial bulge–disk decomposition that tells us how much light to ascribe to each component at each point in the galaxy, we have first collapsed the integral field spectroscopy data cube in the spectral direction to produce a fairly crude image of the galaxy at the appropriate spatial resolution.

To determine the photometric parameters of the bulge and disk we use GALFIT (Peng *et al.*, 2010a), which fits the image with a 2-dimensional model composed of combinations of various components. The simple structure of lenticular galaxies, in particular the sample selected here which show no evidence of bars or spiral structure, allow us to fit the galaxy with a simple two component model. Bulges and disks have been found to be well described by a Sérsic profile (Sérsic, 1963), where disks tend to have a Sérsic index $n = 1$, also known as an exponential profile, and bulges have a Sérsic index ranging from $n \approx 1$ to $n \approx 4$. Bulges of lower Sérsic index are more disk-like and are known as pseudo-bulges, while a profile with $n = 4$ is known as a de Vaucouleurs profile (de Vaucouleurs, 1948) and is commonly associated with classical bulges and elliptical galaxies. As n increases, the profile becomes more centrally concentrated with extended wings (see Section 1.4 for more details).

We allow the Sérsic index of the bulge to vary, along with the magnitude, position angle, axis ratio and effective radii of both components. We fix the Sérsic index of the disk at $n = 1$. The specific point-spread function (PSF) for this observation is not part of the currently-released CALIFA data, so we modelled it as a narrow Moffat profile plus a broad low-intensity Gaussian as described in García-Benito *et al.* (2015), and varied its Moffat parameters to minimise the residuals between model and image data.

The best fit was found to result from a PSF with a FWHM of $2.2\,\mathrm{arcsec}$, although the subsequent results do not depend sensitively on the exact value adopted.

The parameters of the derived best-fit galaxy models for the three sample galaxies are listed in Table 3.1, and an indication of the quality of the fit is provided in Figure 3.1, which shows data, model and residuals for NGC 528. The fit is generally very good, although the central asymmetric residual indicates that the galaxy seems to have a slightly off-centre nucleus, but this phenomenon has no effect on what follows. It is also interesting to note from Table 3.1 that this galaxy clearly favours an almost exponential bulge with a Sérsic index near unity, and is therefore an example of the non-classical bulge behaviour mentioned above.

	NGC 528		NGC 7671		NGC 6427	
Parameter	Bulge	disk	Bulge	disk	Bulge	disk
R_e/R_S	$2.2'' \pm 0.1''$	$9.2'' \pm 0.1''$	$1.6'' \pm 0.002''$	$8.68'' \pm 0.05''$	$2.90'' \pm 0.04''$	$9.88'' \pm 0.11''$
Axis ratio	0.78 ± 0.01	0.52 ± 0.01	0.93 ± 0.01	0.67 ± 0.002	0.797 ± 0.003	0.474 ± 0.003
n	1.07 ± 0.04	1.0 (fixed)	0.99±0.04	1.0 (fixed)	0.93±0.03	1.0 (fixed)
PA	-89.8 ± 2.57	59.02 ± 0.15	18.6±7.6	-43.6 ± 0.3	64.8 ± 2.6	34.7 ± 0.3
$\frac{B}{T}/\frac{D}{T}$	0.28 ± 0.01	0.72 ± 0.01	0.28 ± 0.01	0.72 ± 0.01	0.32 ± 0.01	0.68 ± 0.01

Table 3.1: Parameters of GALFIT photometric decomposition of collapsed data cube image of NGC 528, NGC 7671 and NGC 6427. Note the errors shown are statistical estimates directly from GALFIT, which underestimate the true uncertainties.

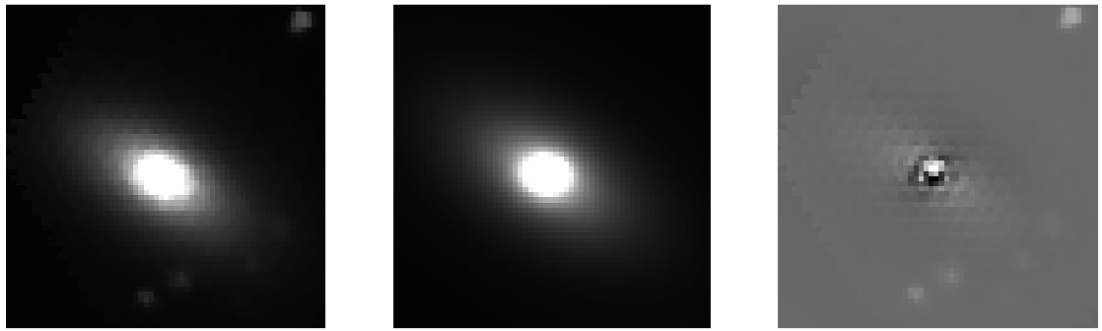


Figure 3.1: The collapsed CALIFA data cube for NGC 528, the GALFIT best fit model, and the residuals (galaxy minus model)

3.1.2 Spectroscopic bulge–disk decomposition

In order to carry out the spectral decomposition, we need to fit bulge and disk components, weighted by their relative contribution at each spatial coordinate of the data cube, to the spectrum at that point. To this end, we have used the Python version of the penalised pixel-fitting code, updated as described in Cappellari & Emsellem (2004) which, from version 5.1, allows multiple components with different populations and kinematics to be fitted to spectra simultaneously (see Johnston *et al.* 2014).

For a given set of nonlinear parameters, pPXF solves a linear system for the weights of the spectral templates and additive polynomials, with the extra constraint that the weights of the spectral templates must be non-negative [eq. 3 in Cappellari & Emsellem (2004)]. This linear least-squares problem is solved by pPFX as a Bounded Variables Least Squares problem, with the specific BVLS method by Lawson & Hanson (1995).

Here we want to enforce an additional constraint to the problem: we require the template spectra describing the bulge component to contribute a prescribed fraction $f_{\rm bulge}$ of the total flux in the fitted spectrum

$$f_{\rm bulge} = \frac{\sum w_{\rm bulge}}{\sum w_{\rm bulge} + \sum w_{\rm disk}}, \tag{3.1}$$

where $w_{\rm bulge}$ and $w_{\rm disk}$ are the weights assigned to the set of spectral templates used to fit the bulge and disk respectively.

This constraint could be implemented by using a generic quadratic programming algorithm to solve the linear least-squares sub-problem, while including equation (3.1) as an exact linear equality constraint. Instead, we chose a simpler route, which requires minimal changes to the pPXF algorithm. It consists of enforcing the equality constraint by adding the following single extra equation to the linear least-squares sub-problem

$$\frac{1}{\Delta}\left[(f_{\rm bulge} - 1)\sum w_{\rm bulge} + f_{\rm bulge}\sum w_{\rm disk}\right] = 0, \tag{3.2}$$

with the parameter Δ set to a very small number (e.g. 10^{-9}), which specifies the relative accuracy at which this equation needs to be satisfied. When both the spectral templates and the galaxy spectrum are normalized to have a mean flux of order unity, the best fitting weights $w_{\rm bulge}$ and $w_{\rm disk}$ are generally smaller than unity and equation (2) is satisfied to numerical accuracy. This new option is activated by setting the

keyword FRACTION from the Python pPXF version 5.2. Activating this option results in a negligible execution time penalty of the pPXF fit, when compared to an unconstrained fit.

3.1.3 Tests

The pPXF code requires that one specifies the base set of stellar populations from which the model is constructed. For this analysis, we have adopted the single stellar population templates of Vazdekis *et al.* (2010), providing high-resolution spectra for stellar populations with 7 different metallicities ranging from -2.32 to 0.22 and 42 ages from 0.06 Gyr to 17.8 Gyr, resulting in a total catalogue of 350 spectra. An age range that extends beyond the age of the Universe is required to account for uncertainties in the stellar population models. Some caution is necessary in using such models, both in the extremes of metallicity, where observations are scarce, and generally since such models must assume an initial mass function, the shape of which is notoriously uncertain. However, combinations of this extensive library should provide a reasonable match to most stellar populations that we are likely to encounter, and offer at least an initial estimate of their ages and metallicities.

In general, the signal-to-noise ratio of the individual spectra in the data cube is not sufficient to fit simultaneously for kinematics and populations of multiple components. In order to determine at what signal-to-noise level this fit becomes possible, we have tested the method by decomposing a simulated galaxy spectrum composed of two stellar populations of different ages and metallicities and with kinematics typical of a non-rotating bulge and disk. To explore the full capabilities of the method we have looked at models with a galaxy bulge-to-total ratio of 0.3 and 0.5, and for each we vary the simulated signal-to-noise ratio from 10 to 35. To ensure the model is actually converging on the proper solution and does not simply return values close to the initial estimates, we have performed ten realisations at each signal-to-noise ratio, each time setting the initial kinematic estimates of both velocity and sigma to be a random value within 50 km s^{-1} of the actual value. The best-fit kinematics and stellar populations at each signal-to-noise ratio are shown in Figure 3.2.

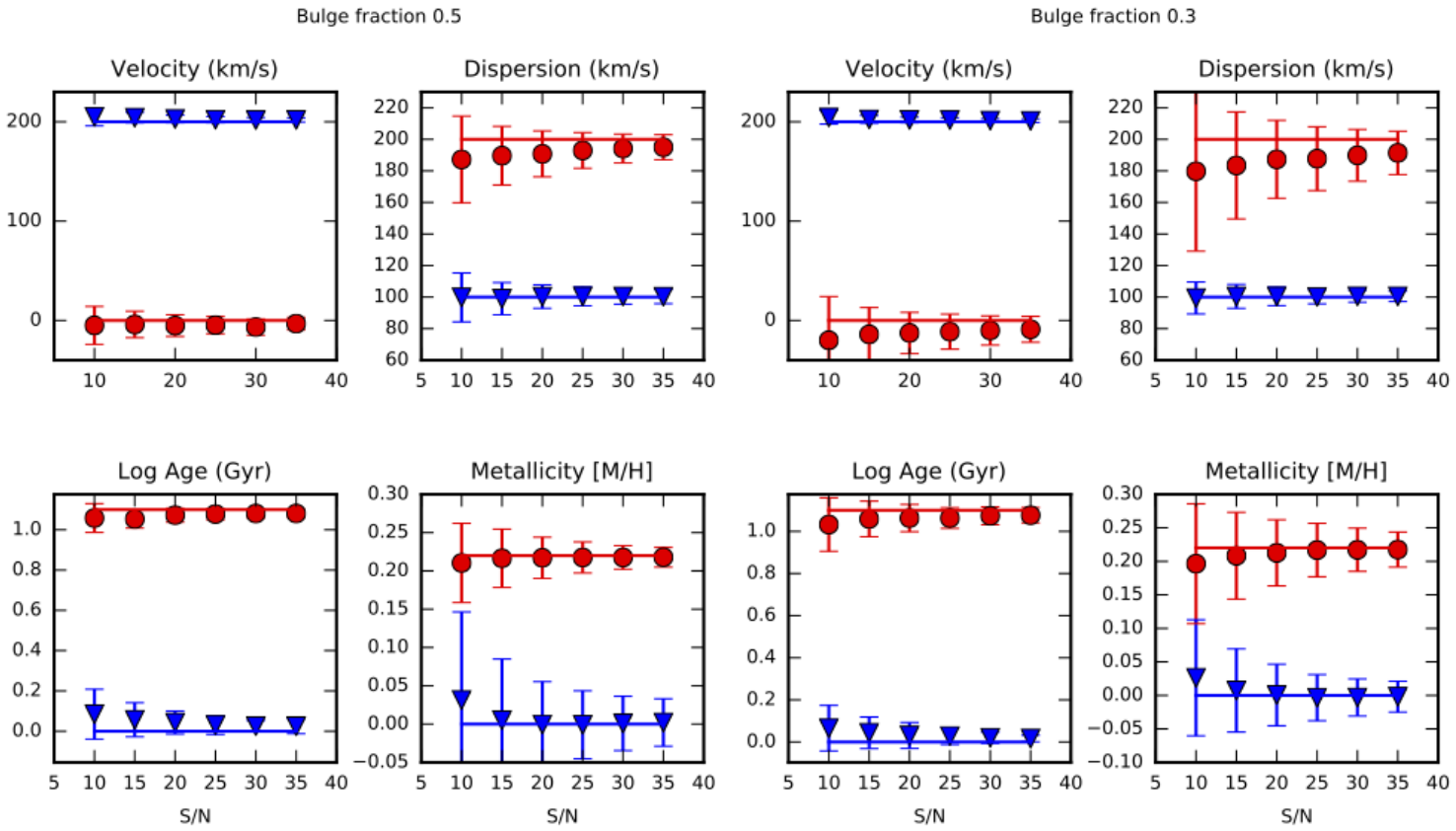


Figure 3.2: Best-fit kinematics and stellar populations for a simulated galaxy spectrum with a non-rotating, high dispersion bulge of 12 Gyrs and metallicity of 0.22, and a rapidly rotating, cool disk of 1 Gyrs and solar metallicity. The left-hand side shows a case with a bulge fraction of 0.5 and the right-hand side with a bulge fraction of 0.3. Red circles represent the median values of 10 realisations with varying initial estimates for the bulge, and blue triangles represent the same for the disk. The error bars show the standard deviation of the 10 realisations. The solid line shows the actual values given to the components.

This test demonstrates the effectiveness of the method, showing that when both components contribute a significant amount to the flux, both their kinematics and stellar populations can be accurately determined with no systematic errors, and are not heavily dependent on the initial kinematic estimates. The velocity dispersion and metallicity tend to be more difficult to determine than the line-of-sight velocity and the age, but these effects are well known and inherent in the difficulties of spectral fitting. It is also clear that when a component contributes less flux to the galaxy spectrum, its properties are harder to determine. However, even down to a flux fraction of 0.3, the parameters can be reliably obtained, albeit with some scatter.

The test demonstrated above takes a fairly extreme case of a non-rotating very old bulge and a rapidly rotating very young disk. It is therefore helpful to also look at a case where the parameters of the two components are more similar, as is likely to be the case in many galaxies, particularly early-type galaxies where we would expect both bulge and disk to be fairly old. Such a case, with bulge and disk ages of 12.6 and 7 Gyrs, velocities of 150 and 200kms^{-1}, and metallicity and dispersion as before, is shown in figure 3.3.

It is clear that, for sufficiently high signal-to-noise, the parameters are still accurately found, though, as is expected, the more similar the two components are, the more difficult it becomes for pPXF to extract their parameters. This is particularly noticeable for the age and metallicity of the components, which appear to be harder to separate at lower signal-to-noise ratios. At sufficiently high signal-to-noise however, pPXF still accurately determines the relative difference between the populations of the bulge and disk, and in fact tends to underestimate the difference between the components, such that if any difference is found, it is unlikely to be purely an artifact of the fitting process. In addition, while the systematic errors in the age and metallicity should be kept in mind when interpreting future results, this will not effect the question of the distinctness of the components, which depends on the separation of kinematics.

A potential method of understanding the more detailed effects any errors may have on the fitting process would be to perform a full bulge-disk decomposition on an artificial galaxy, built from SSP model spectra. We believe that the tests performed here are currently sufficient to demonstrate the ability of the method to accurately decompose a

galaxy bulge and disk and address the distinctness of the components, but future work may benefit from such a full-galaxy approach.

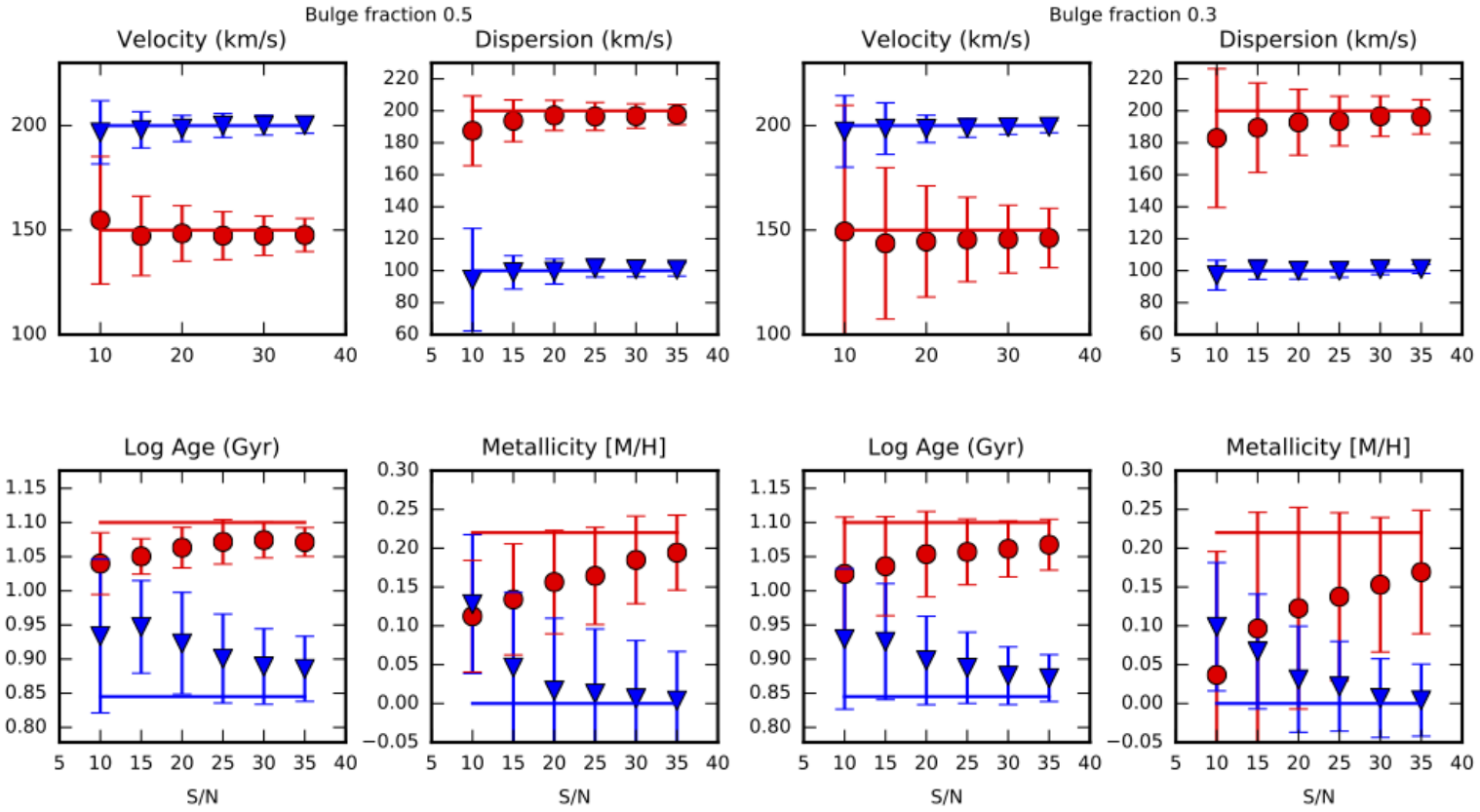


Figure 3.3: Best-fit kinematics and stellar populations for a simulated galaxy spectrum with a rotating, high dispersion bulge of 12 Gyrs and metallicity of 0.22, and a rapidly rotating, cool disk of 7 Gyrs and solar metallicity. The left-hand side shows a case with a bulge fraction of 0.5 and the right-hand side with a bulge fraction of 0.3. Red circles represent the median values of 10 realisations with varying initial estimates for the bulge, and blue triangles represent the same for the disk. The error bars show the standard deviation of the 10 realisations. The solid line shows the actual values given to the components.

To retain as much spatial information as possible while avoiding significant biases, particularly in the derived age and metallicity, a signal-to-noise ratio of 25 was adopted for the decomposition. In order to obtain spectra of this quality from the CALIFA data cube, we co-added the data spatially using the Python version of the Voronoi binning code of Cappellari & Copin (2003).

We performed an additional test on the real CALIFA data-cube of galaxy NGC 528, taking a sample of bins along the major axis of the galaxy and performing the decomposition for each bin over a grid of bulge and disk velocities, from -400 km s^{-1} to 400 km s^{-1}. pPXF uses a local non-linear optimization algorithm to fit the kinematics, starting from an initial guess for the parameters. However, with multiple kinematic components, the χ^2 will generally present multiple local minima and there is no guarantee pPXF will converge to the global one. A simple brute-force way of finding the global minimum consists of sampling a regular grid of starting guesses with pPXF. By constraining the velocities of the fit to be within the pixel of the velocity grid, while letting the velocity dispersions vary freely, pPXF is forced to cover the full range of velocities, and we can therefore make sure we find the global rather than a possible local minimum for the χ^2.

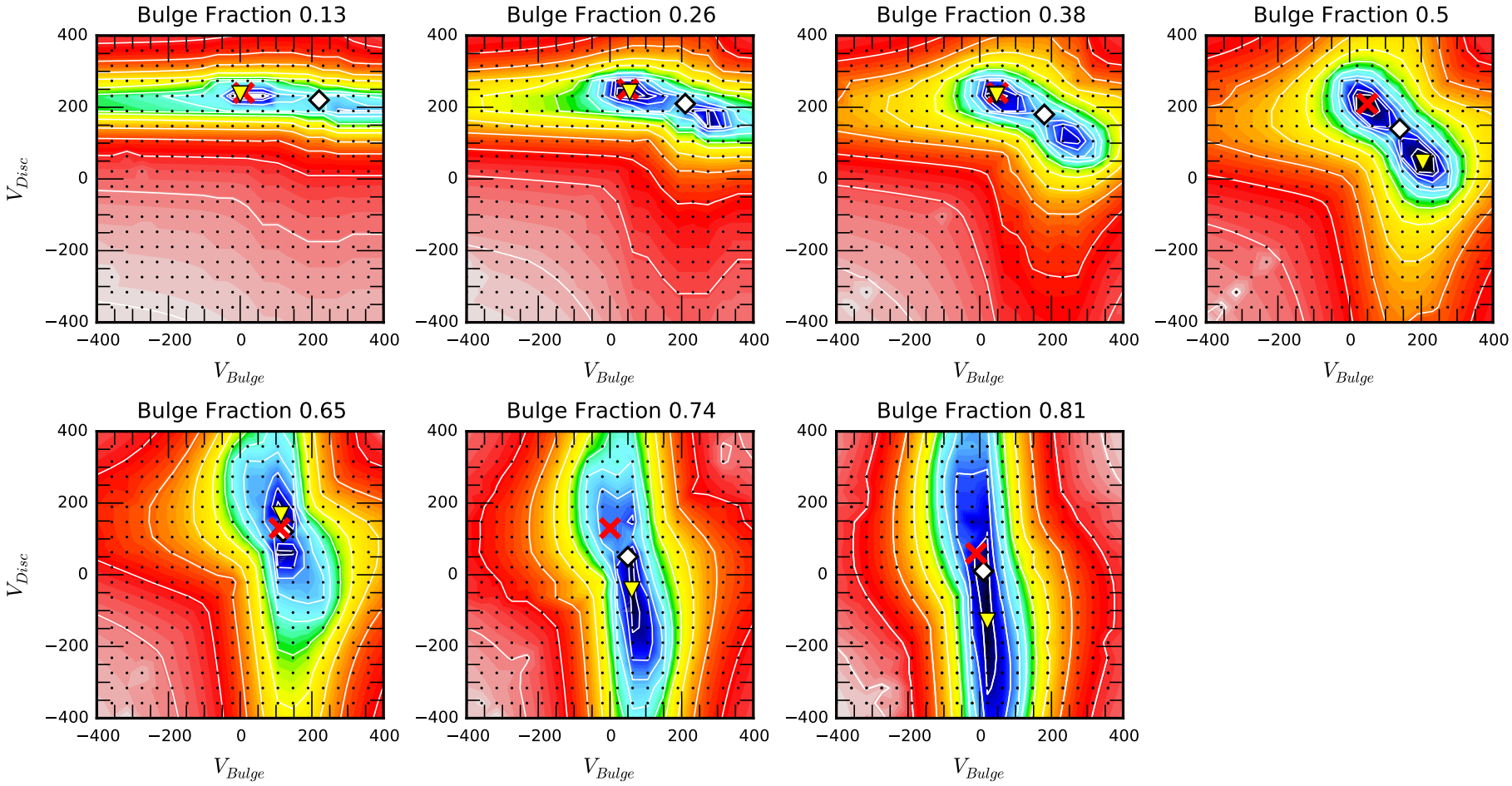


Figure 3.4: Chi-squared maps for a sample of bins along the major axis of the galaxy. One sigma contours are also plotted. Red crosses show the velocities found when pPXF is left free to vary, white diamonds show the velocity of a one component fit, and yellow triangles show the velocities for the lowest chi-squared grid pixels. When the yellow triangles and red crosses coincide, pPXF is effectively finding the global minimum from the estimated starting conditions.

The chi-squared map over this grid is shown in Figure 3.4 including contours spaced at 1 sigma intervals, with the minimum chi-squared locations indicated by the yellow triangles. In order to evaluate how well pPXF finds this global minimum, the best-fit velocities found by pPXF when it is left free to vary are plotted as red crosses. As starting conditions for this free fit we took the velocity of a single component fit for the disk velocity, and the average velocity dispersion in the disk dominated region of the galaxy, here 144 km s^{-1} for the disk dispersion. For the bulge we estimated zero rotational velocity, and a velocity dispersion value of 200 km s^{-1}.

This test gives us an insight both into how well pPXF finds the true best fit to the data when left free, and how accurately the kinematics of the components can really be determined overall for this quality of data.

As is to be expected, when a component dominates the flux pPXF effectively finds the best fit to the kinematics for this component when left free, and the velocity of this component is very well constrained, with the one-sigma contours covering a small range of velocities. However, the kinematics of the component with less flux are less likely to be found by pPXF and tend to show some degeneracy. This is especially apparent in bulge-dominated regions of the galaxy, with the one sigma contours stretching over a wide range of disk velocities. This is not surprising considering that in the very central regions of the galaxy there will be little difference in velocity between the two components, making it almost impossible to separate the LOSVDs effectively.

The tests also demonstrate that, in the central regions of the galaxy, when pPXF is left free it does not always find the true chi-squared minima. Though the difference here is generally less than 3 sigma, for data of lower signal-to-noise and lower resolution this may not be the case. Therefore, we decided that to ensure that the true chi-squared minimum is found each time, when performing the decomposition on the full galaxy a simple 5×5 grid of velocities should be used for every Voronoi bin.

Also important to note is that when both components contribute comparable fluxes, two clear minima in chi-squared are visible, which have significantly lower chi-squared than the single component fit. This shows that the spectrum is better fit by two Gaussian components with different velocities and velocity dispersions, rather than one single Gaussian component. This is a first indication that two kinematically-distinct

components do appear to be present in this galaxy.

It is worth noting that in conducting these tests we have built the machinery necessary to check the reliability of the decomposition process for any additional parameters, be it signal-to-noise ratio, initial kinematic estimates, component flux contribution etc. which will become useful when exploring new data and more complex systems.

3.1.4 NGC 528

In order to determine the kinematics of the bulge and disk implied by the assumed bulge–disk photometric decomposition, we have fitted each Voronoi bin with a kinematic model comprising two components with Gaussian line-of-sight velocity distributions. As demonstrated above (Section 3.1.3), in order to be certain that the true best fit to the spectra is being found, it is safest to force pPXF to cover a wide range of velocities for each component. For each Voronoi bin we therefore take the best fit to the spectrum across a 5×5 grid of velocities ranging from -350 km s^{-1} to 350 km s^{-1}. By constraining the resulting velocities of each fit to be within the pixel size of the grid, pPXF is forced to cover the whole velocity range and therefore find the true chi-squared minimum. The only additional constraint on the decomposition is that one component must reproduce the flux of the bulge derived in the photometric decomposition, while the other component must reproduce the disk flux. Both velocity dispersions and the stellar populations of the two components were left as free parameters. Since a change in kinematics can be slightly offset by altering the template spectra selected for the fit, it was deemed safest to continue to use the whole catalogue of 350 spectra to fit each component.

The resulting kinematic maps are presented in Figure 3.5. To avoid plotting noise and to give a clear indication where each component dominates, we have only reproduced the kinematic maps in regions where a component contributes at least 30% of the total flux. As shown above, we found that below this level pPXF struggled to effectively distinguish the LOSVD of the lower flux component. The outer limit of the disk is determined by a minimum signal-to-noise threshold required for the Voronoi binning process, discarding pixels in the collapsed data-cube where the signal-to-noise ratio is too low.

It is apparent from this figure that this process decomposes the galaxy into remarkably coherent individual components, with a well-behaved symmetrically-rotating disk that has a low dispersion at all radii, and a symmetric high-dispersion rotating bulge with a dispersion profile that decreases in an orderly manner with radius. Note that the symmetric appearance of the kinematics is in no way imposed on the results: each spatial bin is decomposed independently, so the coherence of the map is a direct indicator of the consistency and reproducibility of the results, even down to the level where the component is only a 30% contributor to the total light.

The derived velocity dispersion of the bulge is high, but quite consistent with the central dispersion of 264 km s^{-1} found by Scodeggio, Giovanelli & Haynes (1998), and the expected properties of such a massive galaxy ($1.5 \times 10^{11}\mathrm{M}_{\odot}$). The mass of the galaxy is also reflected in the rotation speed of the disk, which, after correcting for inclination, implies a value of a little over 300 km s^{-1}. Astrophysically, the rotation of a low-Sérsic-index bulge is not surprising and agrees with multiple studies finding that these flatter bulges tend to display disk-like characteristics (see Kormendy & Kennicutt 2004 and references therein). The bulge rotation is also consistent with the finding that bulges and disks in fast-rotator early-type galaxies are best described by constant anisotropy (see Cappellari 2016 for a review).

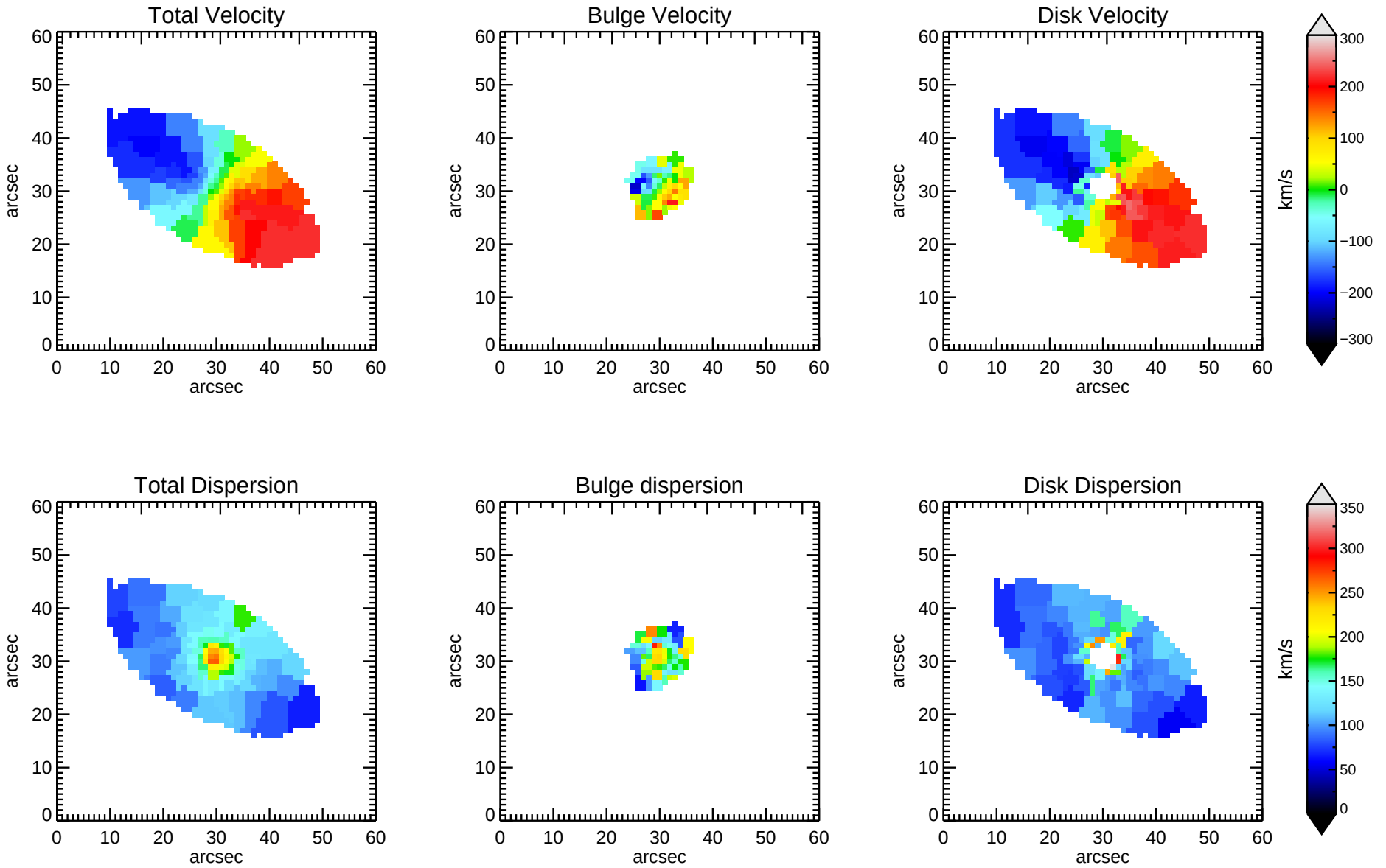


Figure 3.5: Kinematic maps for a one component fit (left) and two component fit (centre and right)

3.1.5 NGC 7671 and NGC 6427

Two other galaxies in this initial test, NGC 7671 and NGC 6427, were analysed in the same way. The galaxy magnitudes, masses and inclinations are shown in Table 2.1 and the parameters of the GALFIT photometric decomposition are shown in Table 3.1. Similar to NGC 528, both galaxies also possess low-Sérsic-index bulges, allowing us to gain further insight into these systems.

Figure 3.6 and Figure 3.7 show the resulting decomposed kinematic components. Again, the decompositions result in two very coherent components which match the photometric decomposition very well, and, as for NGC 528, both show cold rotating disks and hot rotating bulges. Comparing Figures 3.5, 3.6 and 3.7 there is a clear similarity in the kinematic components of these three galaxies as well as the photometric components. This suggests that not only do photometric decompositions represent individual stellar components, but the underlying kinematics of these components may potentially be deduced from their photometric parameters. Of course a much larger, more varied sample of galaxies will be required to determine if this relation holds in general.

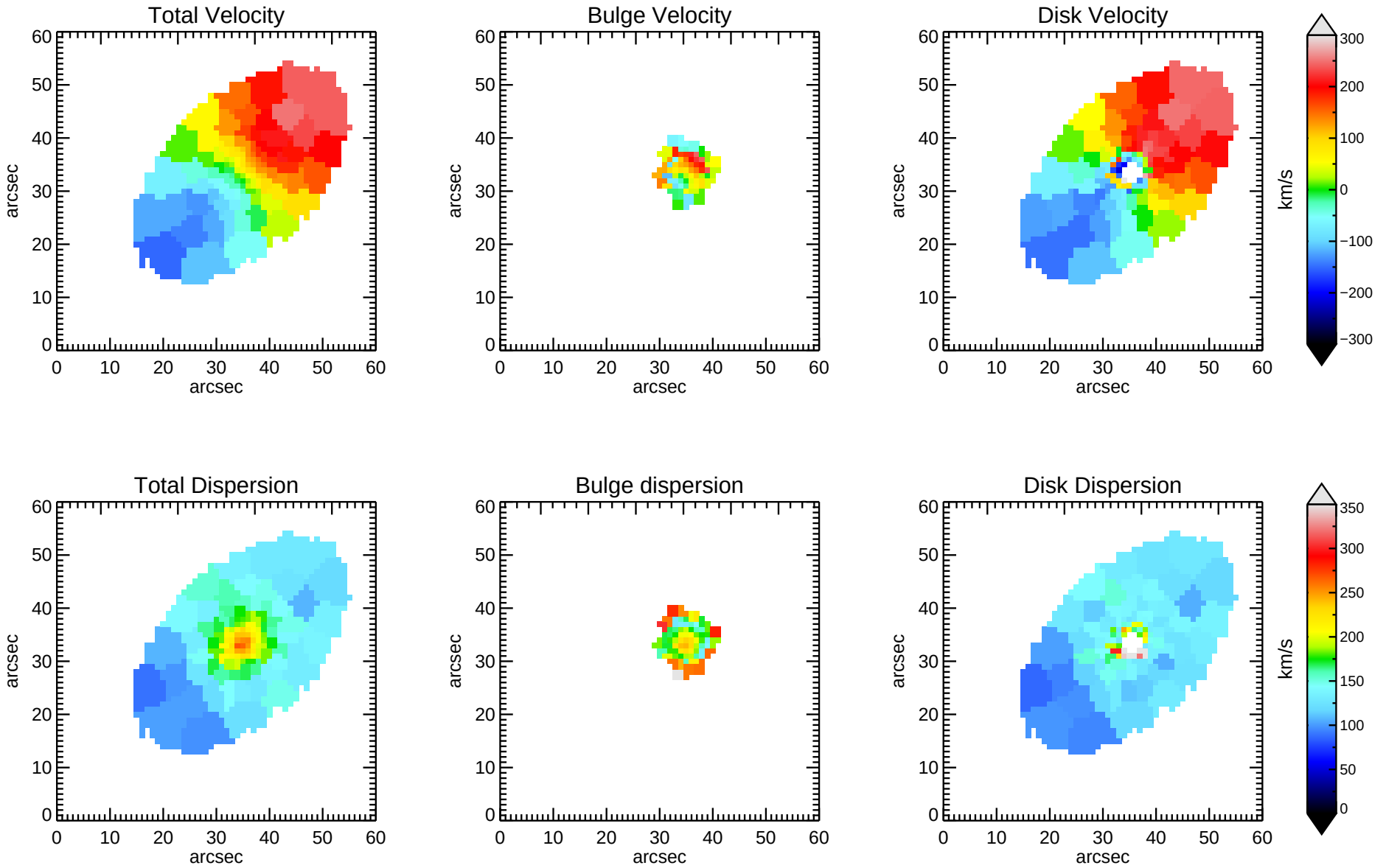


Figure 3.6: Kinematic maps for a one component fit (left) and two component fit (centre and right) for NGC 7671.

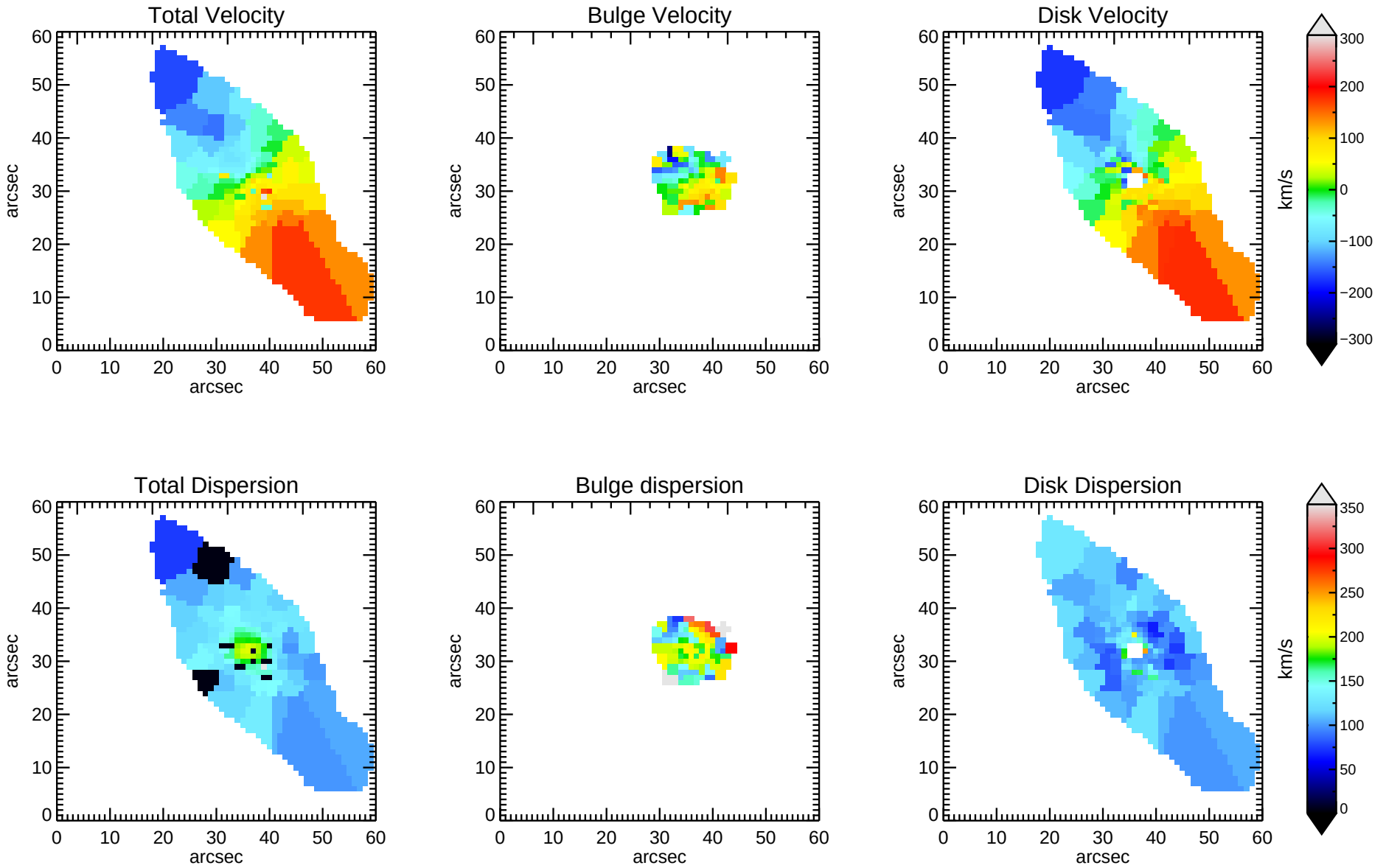


Figure 3.7: Kinematic maps for a one component fit (left) and two component fit (centre and right) for NGC 6427.

3.1.6 Stellar Populations

Since our fits also left the choice of stellar population completely free, as well as the weight assigned to each stellar population, they provide a measure of the age and metallicity of each component in each spatial bin, which yields further information on a galaxy's past history. In particular, we can go beyond the analysis undertaken by Johnston, Aragón-Salamanca & Merrifield (2014) to look for spatial variations in the properties of the population within a single component. To illustrate the potential in such data, Figures 3.8, 3.9 and 3.10 show luminosity-weighted log age and metallicity of the single stellar population spectra selected by pPXF for the bulge and disk, defined as

$$\langle \log(\text{age}_{\text{component}}) \rangle = \frac{\sum(w_{\text{component}} \times \log(\text{age}))}{\sum w_{\text{component}}} \tag{3.3}$$

and

$$\langle [\text{M/H}]_{\text{component}} \rangle = \frac{\sum(w_{\text{component}} \times [\text{M/H}])}{\sum w_{\text{component}}}, \tag{3.4}$$

where $w_{\text{component}}$ are the weights assigned to the set of spectral templates used to fit each component.

In contrast to results found for S0s in the Virgo cluster by Johnston, Aragón-Salamanca & Merrifield (2014), the bulges of two of the three galaxies appear to be systematically older and more metal rich than the surrounding disk, indicating a difference in formation scenarios between field and cluster S0 galaxies. Intriguingly, at larger radii there are also the first indications of structure in the metallicity and ages of the individual components that might allow us to go beyond a monolithic view of the formation of bulge and disk.

However, we must await the analysis of a larger sample to see how prevalent such features may be and what implications they hold for the bigger picture of galaxy evolution.

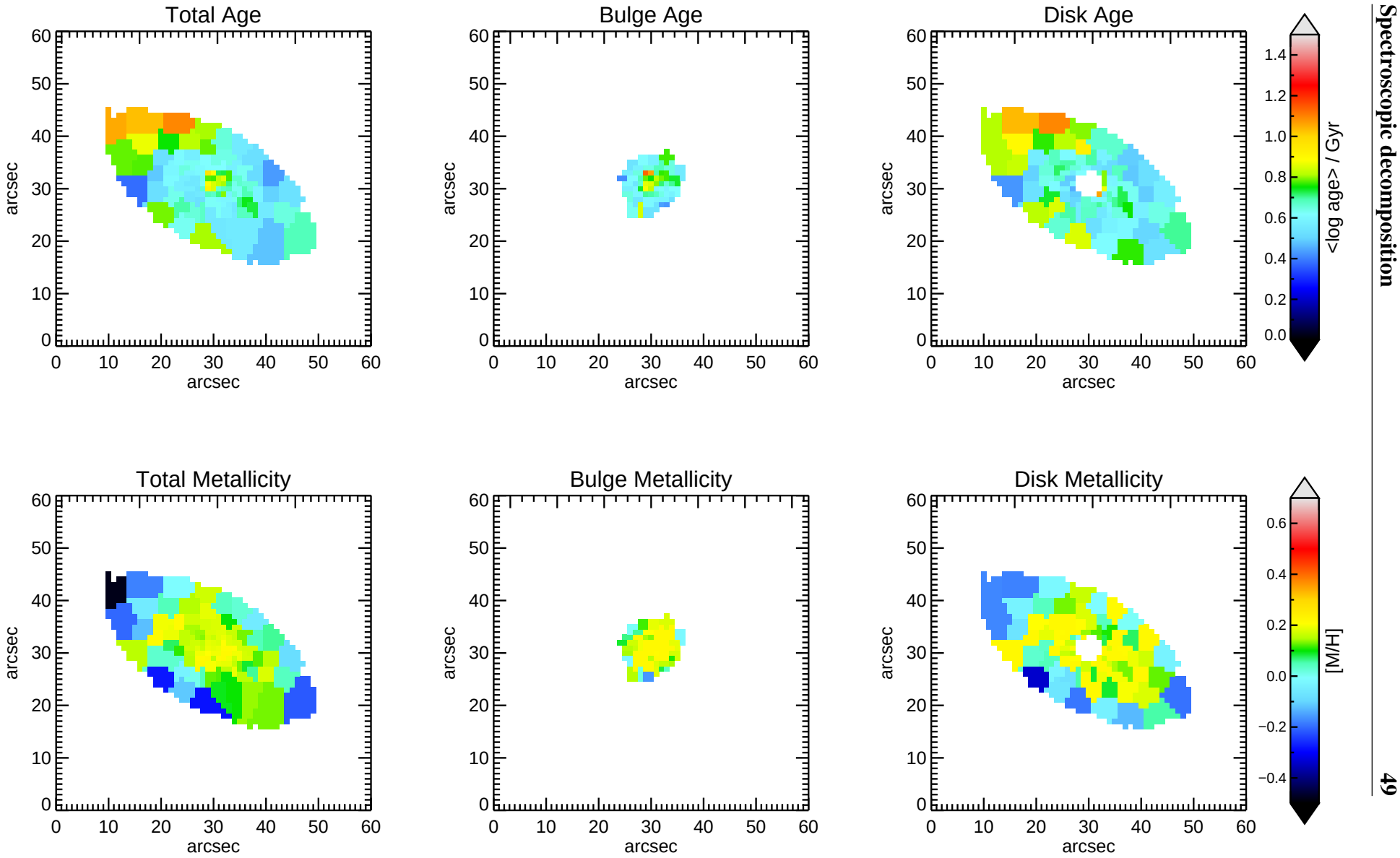


Figure 3.8: NGC 528: maps for the luminosity weighted ages and metallicities of the single stellar population spectra selected by pPXF for the one component kinematic model (left) and the two component kinematic model (centre and right). Bins where the flux of the component contributes less than 30% of the total flux are not included.

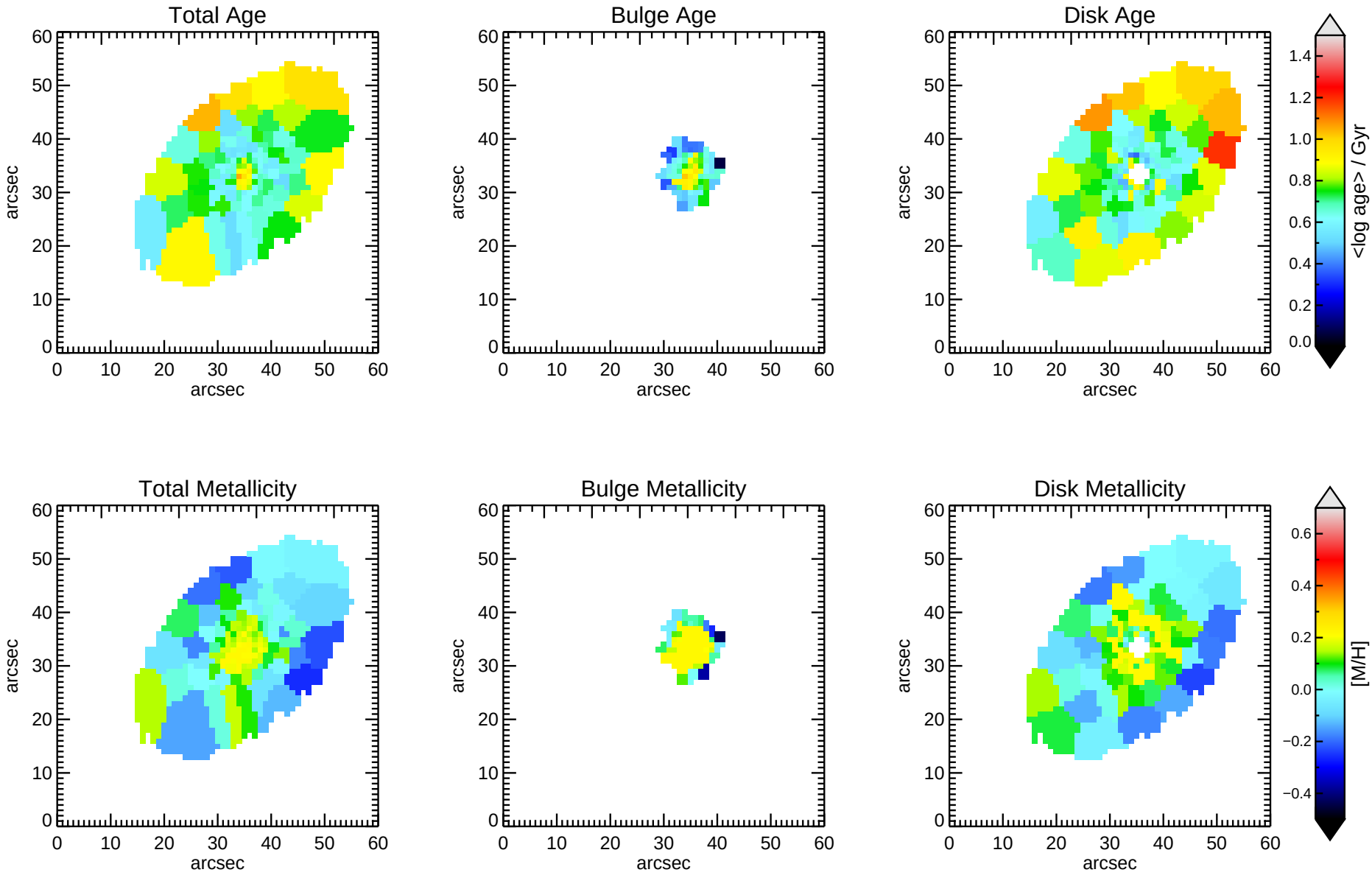


Figure 3.9: NGC 7671: maps for the luminosity weighted ages and metallicities of the single stellar population spectra selected by pPXF for the one component kinematic model (left) and the two component kinematic model (centre and right). Bins where the flux of the component contributes less than 30% of the total flux are not included.

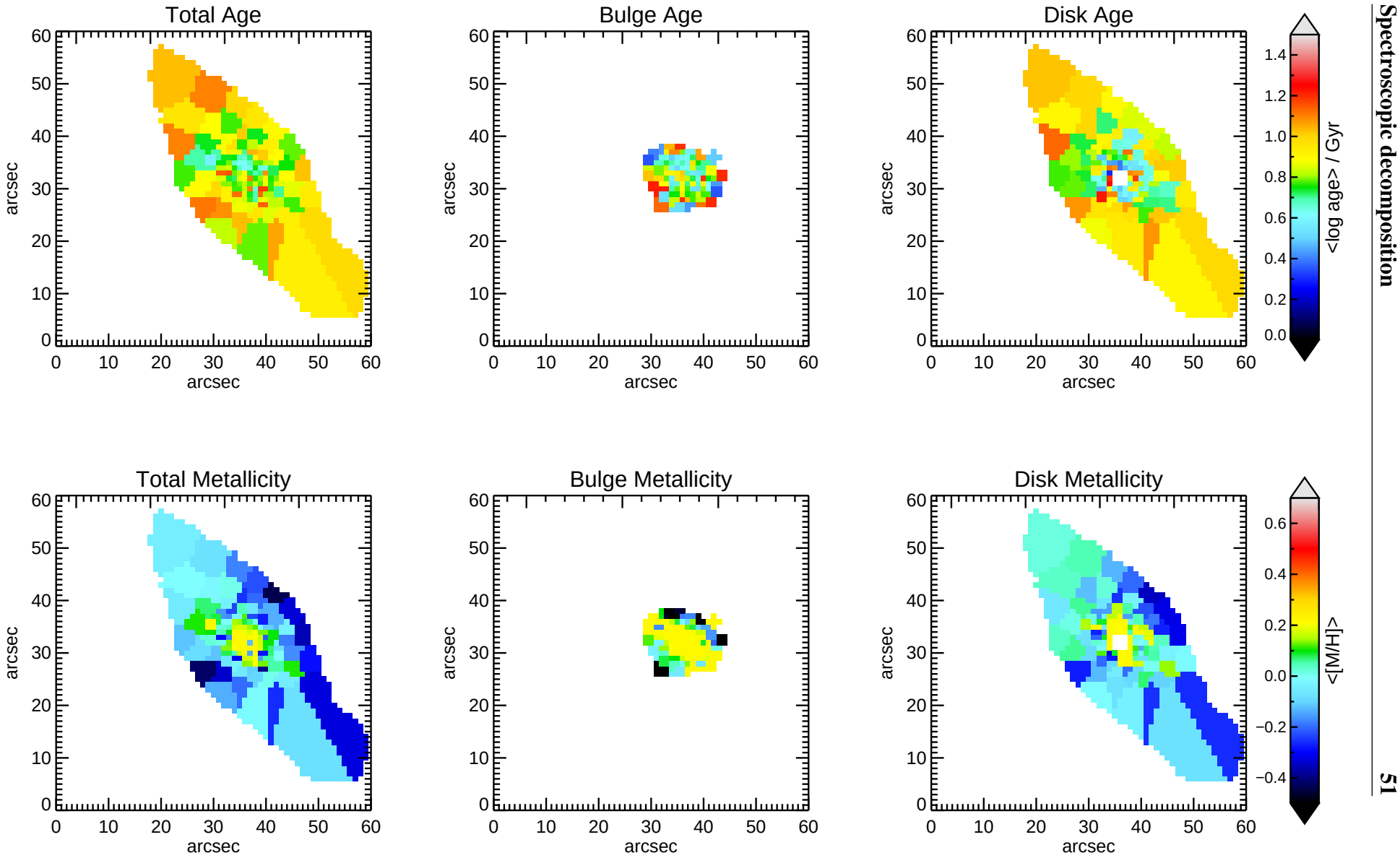


Figure 3.10: NGC 6427: maps for the luminosity weighted ages and metallicities of the single stellar population spectra selected by pPXF for the one component kinematic model (left) and the two component kinematic model (centre and right). Bins where the flux of the component contributes less than 30% of the total flux are not included.

3.2 Discussion

3.2.1 The Method

For this decomposition to be effective we have shown that the data ideally needs to be Voronoi-binned to at least a signal-to-noise ratio of 25 in each bin. This will vary across datasets, depending on spectral range and resolution, but we now have the methodology to test for the appropriate value in other data. To ensure that the true best fit to the data is found, it is best to run over a grid of component velocities for each Voronoi bin. This allows the kinematics to be extracted effectively in this case down to a component flux contribution of 30% of the total flux; a level easily low enough to get detailed information on kinematics and stellar populations for each component. A possible way of obtaining kinematic measurements down to lower flux fractions would be to constrain the stellar populations in some way. One possibility would be to combine this method with the decomposition method of Johnston *et al.* (2012). Their method outputs spectra for the individual components, which if used here would remove the need to fit for stellar populations. This would further constrain the fit and potentially allow information to be extracted even for fainter or embedded components. A more simplistic option would be to build model bulge and disk spectra from the bulge and disk-dominated regions of the galaxy to use in the fit, allowing the stellar populations to be constrained. The obvious disadvantage in this constraint is that we would lose the ability to determine spatial variations in the stellar populations across the components. Careful consideration of the objectives of the decomposition, in terms of whether to prioritise kinematics, stellar populations, or both but to a lower spatial extent, should therefore be considered when undertaking such decompositions on a large scale.

Note that although we have concentrated on applying this method to the decomposition of galaxies into disks and bulges, it could equally well be applied to any other attempt to separate galaxies into components, such as multiple nuclei in giant ellipticals, cores and halos in cD galaxies (e.g. Johnston, Merrifield & Aragón-Salamanca, 2018), and even just line-of-sight blended images. It is also worth noting that any residuals to a fit, whether photometric or spectroscopic, are essentially just another component that can be treated in the same way, so one could, for example, look at the kinematics and

stellar populations of spiral arms that might be left after the fitting of a smooth disk component to a spiral galaxy. As a general method, kinematic spectral decomposition constrained by photometric decomposition has many applications.

3.2.2 Bulge and disk properties

We have demonstrated with this work that bulges and disks are distinct and separable components. This has interesting implications for theories of galaxy evolution, indicating that at least some bulges and disks likely formed through different evolutionary paths.

The bulges of all three galaxies in this sample appear to be rotating, demonstrating that while the components display different kinematics, the difference is not as extreme as historically believed to be, with classical bulges originally believed to rotate very little. This agrees with previous studies finding rotation in bulges, particularly bulges of lower Sérsic indices such as the ones found here (see Kormendy & Kennicutt, 2004, for a review).

We have also shown that there is information in the model stellar populations that produce the best fit. Previous studies into population gradients in S0 galaxies have produced a wide range of results, finding older bulge components than disks (Caldwell, 1983; Bothun & Gregg, 1990; Norris, Sharples & Kuntschner, 2006), similar ages in both components (Peletier & Balcells, 1996; Mehlert *et al.*, 2003; Chamberlain *et al.*, 2011), and older disks than bulges (Fisher, Franx & Illingworth, 1996; Bell & deJong, 2000; Kuntschner, 2000; MacArthur *et al.*, 2004). Studies specifically into S0 galaxies residing in clusters tend to find predominantly younger bulges than disks (Bedregal *et al.*, 2011; Johnston *et al.*, 2012), indicating that these S0s are most likely the evolutionary result of gas stripping from spiral galaxies, in which the "last gasp" of star formation occurred in their central regions, enhancing the bulge light.

In contrast, the galaxies in this sample are found in the field and two of them appear to contain older, more metal rich bulges than disks, as found for conventional spiral galaxies. This suggests that these galaxies could be the end product of spiral galaxies which undergo a much more peaceful evolution, with their star formation gradually ceasing

as they run out of gas [e.g. Cappellari (2016)]. Alternatively inside-out quenching of star formation such as that triggered by morphological quenching could also lead to older, more metal-rich bulges such as those observed here (Martig & Bournaud, 2009), and may be in better agreement with the large, dispersion-dominated bulges present in these galaxies.

This difference in evolution scenarios depending on environment could begin to explain the large range of age gradients found in S0s. However, Fraser-McKelvie *et al.* (2018) divided a large sample of S0 galaxies into bulge and disk regions and analysed the ages and metallicities in each. They found that while high-mass galaxies tended to have older bulges than disks, the opposite was true for low mass galaxies. They also found no trend with environment, though their sample did not extend into dense cluster regions. With the S0 galaxies in Johnston *et al.* (2012) being fairly low mass, this appears to be another example of the 'nature versus nurture' problem; is the variation in bulge and disk stellar populations due to mass or due to environment? A larger sample across a range of masses and densities will be necessary to address this question.

There are also intriguing indications of structure in the metallicity and age maps of the decomposed bulges and disks, showing the potential of the method in revealing more detailed galaxy features. Not much should be inferred for such a small sample, but a systematic analysis of a larger number of galaxies could tell us a great deal about the channels through which these systems form and evolve. Fortunately, there is now no shortage of IFU observations of galaxies on which this technique could be used.

3.3 Conclusions

In this chapter we have developed a method of spectroscopically decomposing galaxy bulges and disks. Our main conclusions are as follows:

- Galaxy spectra are statistically significantly better fit when using two spectra with different stellar populations and kinematics, showing that bulges and disks are distinct and separable components with their own stellar populations and kinematics.

- In terms of the kinematics themselves, it appears that all three bulges are rotating; a finding which, given the low Sérsic-indices found for the bulges in the GALFIT photometric decomposition, agrees with previous literature on the disk-like characteristics often displayed by flatter bulges. With the ability to separate the kinematics of the bulge from those of the disk provided by this method, we can go beyond previous studies and look at the kinematics purely of the bulge component to see in what way they relate to the photometric parameters of the galaxy.

- The stellar populations of the components show interesting variations, with two of the galaxies showing older bulges than disks, in contrast to findings by Johnston *et al.* (2012) for cluster S0s.

Chapter 4

Spectroscopic Decomposition of MaNGA early-type galaxies

"This is one for the good days
And I have it all here
In red, blue, green
Red, blue, green"

– Radiohead

In Chapter 3 we developed a method for spectroscopic decomposition in order to demonstrate that bulges and disks are composed of separate stellar populations, with distinct kinematics. In order to understand the systematic differences between these components, and the role they play in determining the global properties of galaxies, in this chapter we apply the method to a large sample of early-type galaxies selected from the MaNGA survey. The method presented in Chapter 3 was demonstrated on a small sample of galaxies, allowing the fits to be heavily monitored. Applying this technique to a larger sample of galaxies allows us to explore the feasibility of applying the decomposition method to large IFU surveys of different quality and sample size in an automated way.

Without discriminating by kinematics, we apply the decomposition to all galaxies with a clear bulge and disk found during a photometric decomposition, extracting and

analysing the kinematics and stellar populations of the bulge and disk separately. Details on the data and how the sample was selected can be found in Chapter 2.

With mergers, dissipative collapse and secular evolution all leaving their fingerprints in the orbits, chemical composition and age distribution of the stars, this combining of the ages and metallicities with the kinematics of the individual components could be the key to determining where and when these processes dominate.

4.1 Enhancements to the method

In this chapter we use the spectroscopic decomposition method described in Chapter 3. A schematic of the method applied to a MaNGA galaxy is shown in Figure 4.1. Given the difficulties in automating such a complex process, some modifications were made to make the method more robust when applied to large samples of galaxies.

4.1.1 Photometric Decomposition

To obtain the light distribution of the bulges and disks of each galaxy, we performed a photometric bulge–disk decomposition on r-band SDSS NASA Sloan Atlas images, with sky subtraction performed as described in Blanton *et al.* (2011). Using GALFIT (Peng *et al.*, 2002), we fit an exponential disk and a Sérsic bulge, leaving Sérsic index, magnitudes, position angles and scale radii as free parameters, using NSA photometric parameters as initial estimates. To then obtain the bulge and disk fraction across the MaNGA data-cube, we repeat the decomposition on the MaNGA un-binned data-cube, averaged across the whole wavelength range to form a single image, fixing the Sérsic index, position angles, axis ratios and scale radii to those obtained in the previous decomposition. GALFIT produces an image of the bulge and disk components, convolved with the PSF of MaNGA data, which can then be binned into the same bins as the full data-cube, giving the fraction of light in the bulge and disk within each spatial bin.

4.1.2 Spectroscopic Decomposition

During the decomposition, the bulge and disk spectra are constrained to their flux, as determined from the photometric decomposition. In bins where the flux of the two components is similar, there may be some exchange between the components, where the spectrum assigned to the bulge is fitted with the disk velocity, and vice-versa. To prevent any confusion in deciding which value of velocity to assign to the bulge and disk, and to prevent trade-off between the velocities of the components, we decided to build a bulge and disk model spectrum, therefore constraining the stellar populations in order to more robustly determine the kinematics. These are built by averaging the bins where B/T > 0.7 for the bulge and B/T < 0.3 for the disk, where B/T is the bulge-to-total ratio in a given bin, and running pPXF on these two spectra. The resulting model spectra, built from SSP models, are then used as as templates for the future two component fits.

Once the kinematics have been obtained we then repeat the decomposition, using the full library of SSP models but constraining the kinematics to those found in the previous decomposition. We used the single stellar population templates of Vazdekis *et al.* (2010), providing high-resolution spectra for stellar populations with metallicities ranging from -2.32 to 0.22 and ages from 0.06 Gyr to 17.8 Gyr, resulting in a total catalogue of 155 spectra. We found that the stellar populations obtained using this iterative process were similar to those obtained when fitting the stellar populations and kinematics simultaneously, but the kinematics were improved due to any degeneracy between the components being reduced.

To ensure sufficiently high S/N in all bins, while also trying to keep calculation time for the decompositions to a reasonable length, we bin each galaxy spatially to a S/N of 30 using the Voronoi binning method of Cappellari & Copin (2003). If this results in fewer than 20 bins, we do not include the galaxy as this would provide insufficient spatial variations within the components. If the number of bins is greater than 100, however, we increase the S/N in increments of 10 until the number of bins is below 100. Since each bin is decomposed individually, limiting the number of bins keeps running time for each galaxy down.

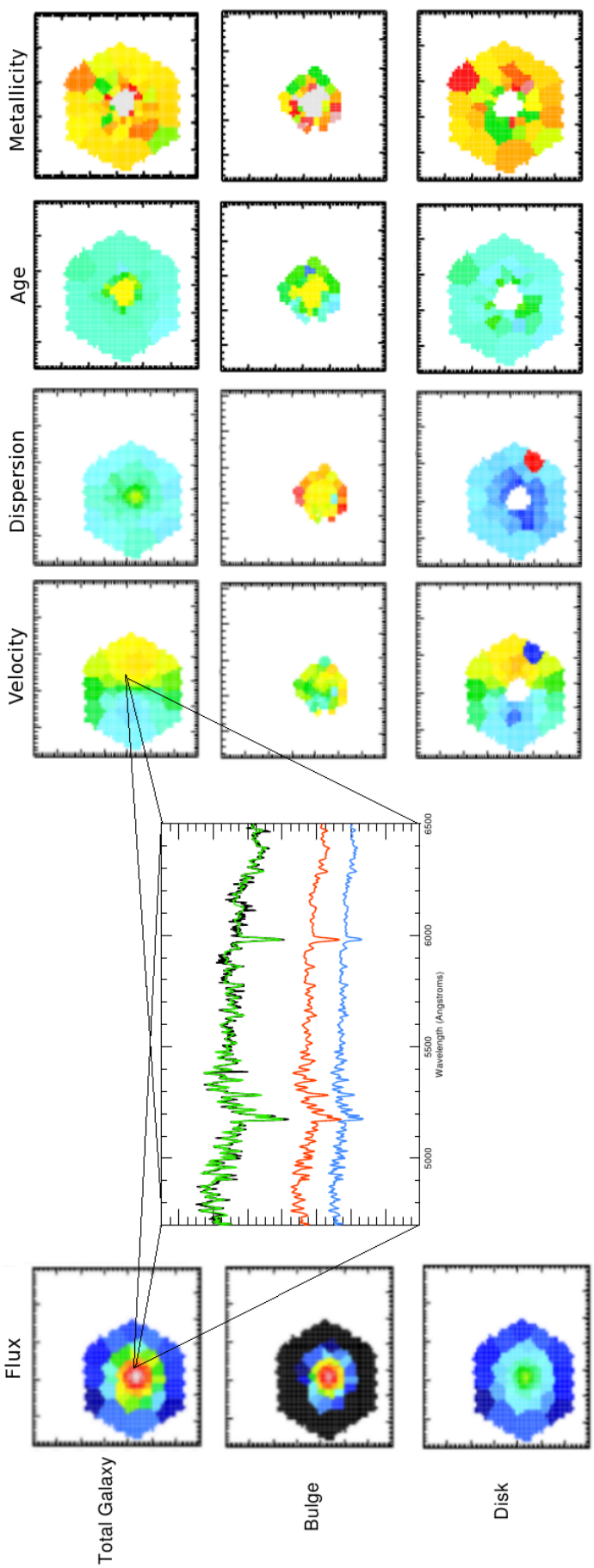


Figure 4.1: Diagram of the decomposition process applied to a sample MaNGA data-cube as described in Chapter 3. On the left is the binned flux maps of the total galaxy, the bulge and the disk, and on the right the maps of velocity, dispersion, age and metallicity arising from the spectroscopic decomposition. The galaxy spectrum for a single bin in the galaxy is shown in black, the decomposed bulge and disk spectra in red and blue, and the sum of the bulge and disk in green.

Selecting galaxies with sufficient flux in the bulge and disk to be able to make meaningful conclusions on their properties is also necessary. To ensure that this is the case we only use galaxies where both components have at least 5 bins in them that contribute greater than 30% of the flux in the that bin. This is effectively like taking a cut in bulge-to-total ratio, since in all of these cases the B/T is less than 0.1 or greater than 0.9.

Several examples of the decomposition are shown in Figures 4.2, 4.3 and 4.4.

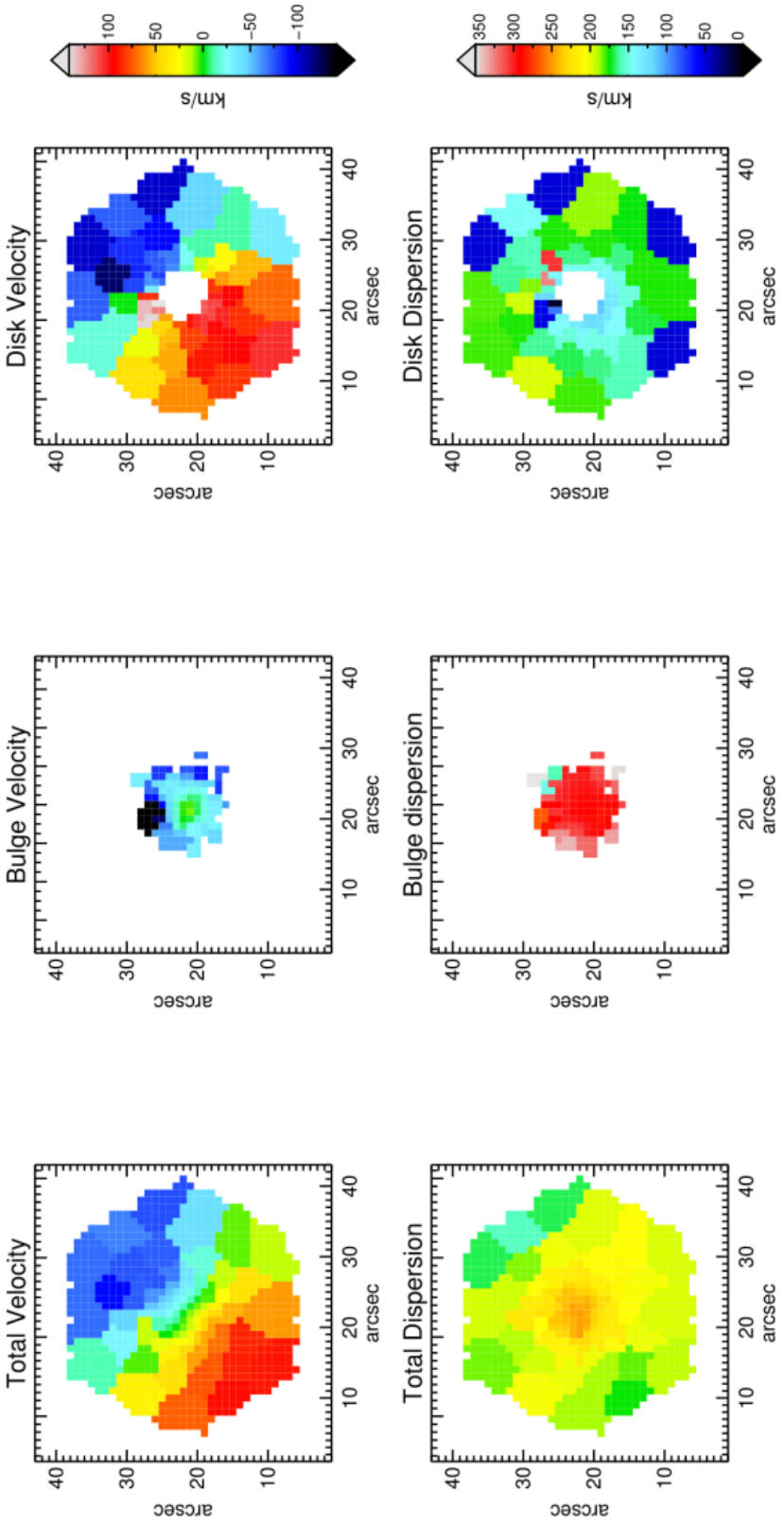


Figure 4.2: Kinematic maps for galaxy with MaNGA plate-IFU 8249-3701.

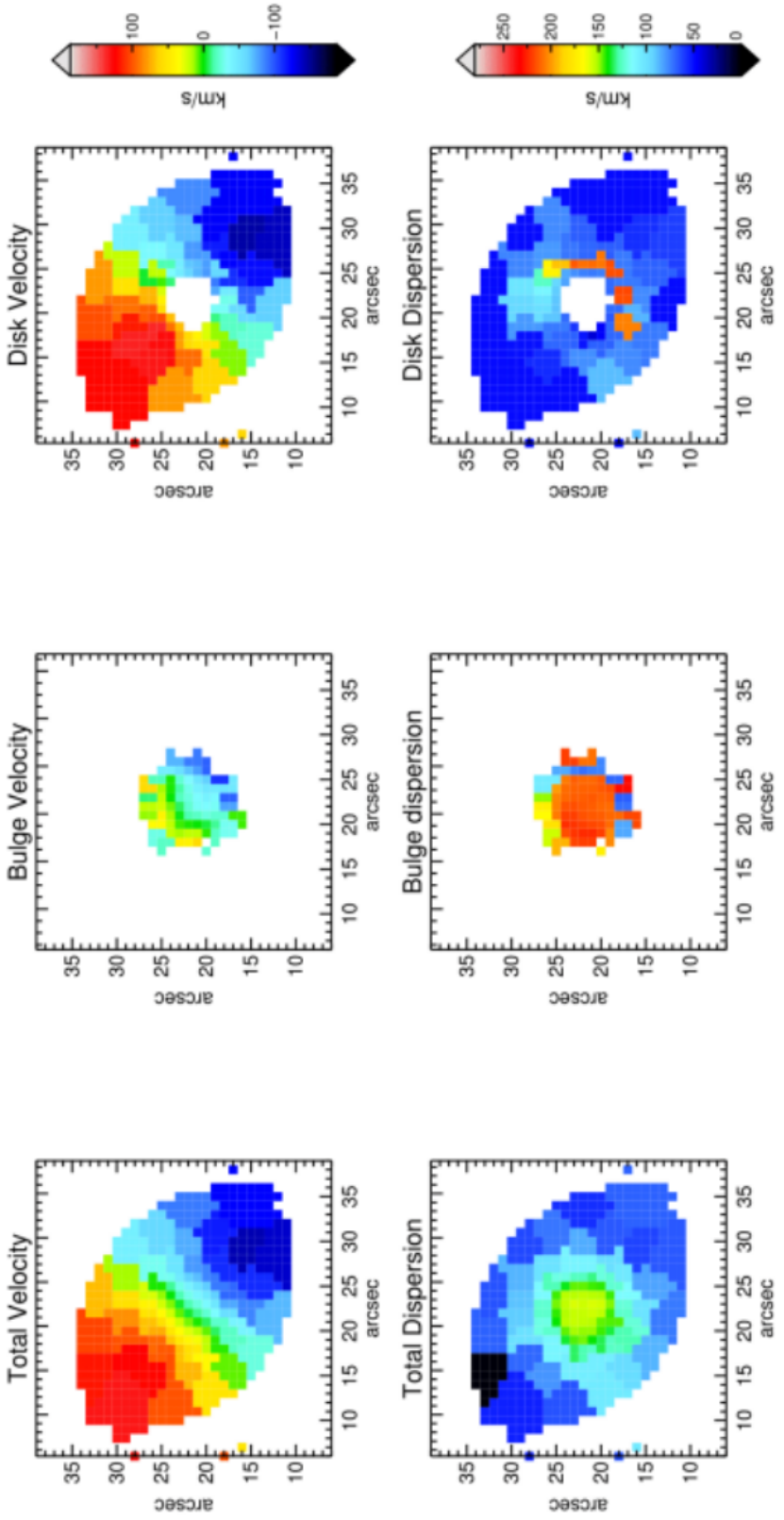


Figure 4.3: Kinematic maps for galaxy with MaNGA plate-IFU 8259-3701.

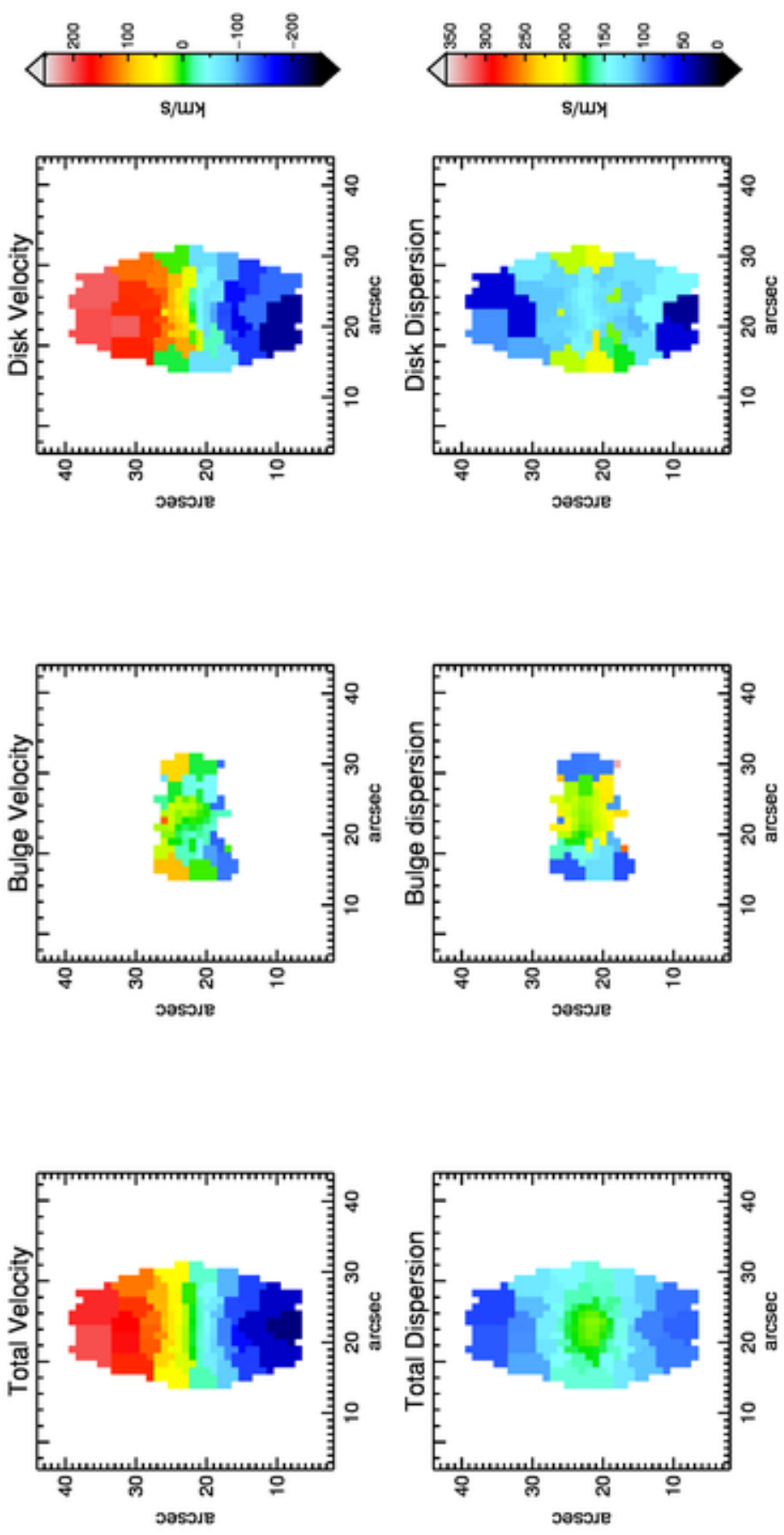


Figure 4.4: Kinematic maps for galaxy with MaNGA plate-IFU 8253-3701.

Once the kinematics and stellar populations have been obtained we apply a few additional constraints to make sure the decompositions are truly separating out bulges and disks. First, in order to avoid including noise, we include bins only in regions where a component contributes at least 30% of the total flux. We also do not include bins where the velocity dispersion of the component is at the far limit of $\sigma = 10$ or $\sigma = 500\text{kms}^{-1}$ set during the pPXF fit, an indication that pPXF has failed to find the true best fit.

Second, partly because not all galaxies in the sample have two kinematic components and partly due to the complexities inherent in performing the decomposition on large numbers of galaxies, the decomposition occasionally fails to effectively fit the kinematics. To account for this, we remove any galaxies where the decomposed disk component has a stellar spin parameter, λ_{Re}, which falls below the fast/slow rotator divide, where λ_R is defined as

$$\lambda_R = \frac{\sum F_i R_i \mid V_i \mid}{\sum F_i R_i \sqrt{V_i^2 + \sigma_i^2}}, \tag{4.1}$$

where R_i, F_i, V_i and σ_i correspond to the radius, flux, line-of-sight velocity and line-of-sight velocity dispersion of the i^{th} Voronoi bin (Emsellem *et al.*, 2007). Fast rotators are then classed as those with

$$\lambda_{Re} > 0.08 + \epsilon/4 \quad \text{or} \quad \epsilon > 0.4,$$

calculated within one effective radius, where the ellipticity, ϵ, is defined as $1 - (b/a)$, where b and a are the minor and major axes of the galaxy, respectively, and b/a is determined from the GALFIT photometric decomposition. An illustration of this boundary can be seen in Figure 4.12. Removing these galaxies after the decomposition rather than making an initial cut on λ_{Re} insures we are not missing galaxies with faint rotating components not evident in the global kinematic measurements. This process removes 30 galaxies, leaving a remaining sample of 272 galaxies.

4.1.3 Aperture effects

Determining parameters within 1R_e of the components allows a comparison of components in a similar way to studies done across the galaxy population. However, parameters such as λ_R and j_* have been shown to depend on the choice of radius within

which they are calculated. This may be due to the bulge and disk components dominating different regions, leading to lower angular momentum in the bulge-dominated central regions of galaxies, but can also be the case even within a pure disk due to the shape of the rotation curve. Comparing the angular momentum of the different components, which dominate in different regions of the galaxy, is therefore subject to biases depending on where the components are in the galaxy, and the radius over which they are calculated. This makes comparisons of the intrinsic properties of the components difficult. To allow a more meaningful comparison, we therefore also determine the parameters only using bins where we have information for both components, i.e. bins where both the bulge and disk contribute greater than 30% of flux, and include these as additional figures in the following sections. Because we also do not include bins where the decomposition has failed, some galaxies in the sample will not have any bins in this overlapping region, which is why the sample size is reduced in these figures. The distribution of the fraction of bins which lie in these overlapping regions is large, ranging from 0 to 0.73, with a mean fraction of 0.26, and does not depend on mass or the effective radii of the components, indicating that we do not introduce any new biases when determining the parameters in this way.

4.2 Stellar Populations

4.2.1 Age and metallicity

Figure 4.5 shows the flux-weighted average ages and metallicities of the two components, coloured by galaxy stellar mass. Due to the flat mass selection of the MaNGA sample, higher mass galaxies are over-represented [see Chapter 2 for a more detailed discussion of this]. The contours shown are therefore weighted by the representation of each galaxy in the sample, assigning higher mass galaxies less weight than lower mass galaxies (Wake *et al.*, 2017). While the ages of the bulges and disks are comparable, there is a clear offset in metallicity towards bulges being more metal rich, though this intriguingly begins to change at lower masses, with both bulge and disk component becoming more metal poor. There is also an interesting tail reaching to younger disks relative to their companion bulges.

When compared to galaxies of a similar mass, these results are broadly consistent with results found by Fraser-McKelvie *et al.* (2018) who more crudely separate S0 galaxies into bulge and disk-dominated regions, and compare their ages and metallicities extracted from spectral indices. They define the component regions as the area within 1 bulge effective radii for the bulge, and the area outside 2 bulge effective radii for the disk, taking the effective radii from the photometric decompositions of Simard *et al.* (2011). They obtain LICK index values of Hβ, Mg*b* and Fe5270, using the dispersion-corrected index measurements from the MaNGA FIREFLY value-added catalogue (Goddard *et al.*, 2017), and combine these over the bulge and disk regions into light-weighted averages. By plotting Hβ against [MgFe]', and comparing their bulge and disk values to contours traced by single stellar population (SSP) models, they estimate ages and metallicities of the two components. Theirs provides a neat way of estimating the stellar population properties of bulges and disks, though it does tend to suffer from problems with contamination, particularly in bulge-dominated galaxies where they find considerable amounts of bulge-light in their disk-dominated regions. However, their sample is similar to the sample used in this work, and a comparing between these two very different methods of obtaining stellar populations provides a convenient sanity check.

The comparison between our work and theirs is shown in figure 4.6. While our measurements of metallicity agree very well, we tend to find slightly older ages. This is expected when comparing spectral index measurements to results from full spectral fitting as done here, since the age-sensitive indices used by Fraser-McKelvie *et al.* (2018) lie at the blue end of the spectrum and are therefore more sensitive to younger populations, while full spectral fitting also takes into account features sensitive to the older stellar populations at the red end of the spectrum.

The similarity in the ages and metallicities of bulges and disks suggests a coupling between the components, which have evidently evolved together, a scenario previously suggested by Laurikainen *et al.* (2010). Johnston, Aragón-Salamanca & Merrifield (2014) also find a coupling in the metallicity of bulges and disks in S0s. They attribute this to the emission from the bulge being dominated by stars formed from gas infall from the disk, leading to similar metallicities in both components, since they

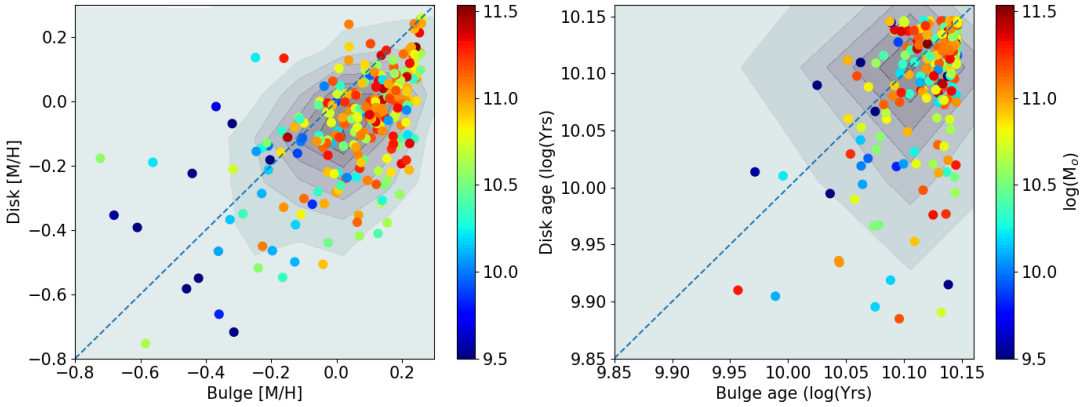


Figure 4.5: Age (right) and metallicity (left) for the bulge and disk components, coloured by mass. Contours (greyscale) show the density of points, weighted by their representation in the MaNGA sample. The dashed line is where bulge and disk parameters are equal.

were formed from the same gas. This theory does not translate directly to this work, however, which finds the bulge to be consistently older and more metal rich than the disk, implying that, while their formations appear to be in some way coupled, the components formed predominantly from gas of different enrichments. The uniformly old stellar ages show that, as expected for such featureless systems, star formation ceased long ago, though the tail to younger, more metal poor disks indicates that on some occasions disks may have either been quenched later than their companion bulges, or possibly experienced some rejuvenation.

Figure 4.7 shows the mass-metallicity relation for the global galaxy and for the individual components. The relation is clear for the global galaxy and holds for both of the individual components, though it is considerably stronger for the bulges than the disks, which show a large amount of scatter. We propose that this can be explained by considering the bulge's position in the centre of the galactic potential well, making it easier to retain metals throughout its lifetime. In contrast, the disk will be more exposed to any external effects such as gas stripping through interactions and gas accretion.

4.2.2 Star-formation histories

Calculating the average ages and metallicities of a stellar population is a good way to get an idea of when most of the stars formed. However, this does not tell the full story of the formation of the components. Often a galaxy will undergo multiple periods of

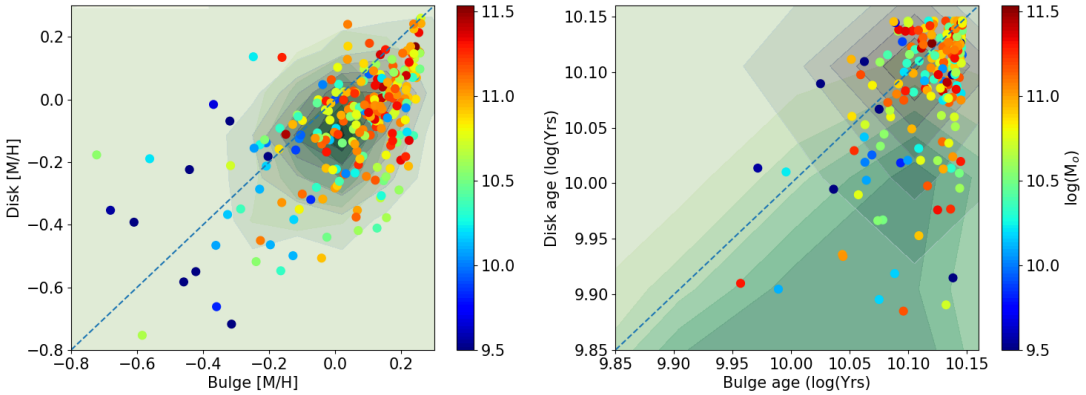


Figure 4.6: Age (right) and metallicity (left) for the bulge and disk components, coloured by mass. Purple contours show the density of points from the work presented here, weighted by their representation in the MaNGA sample. Green contours show the same but for the work of Fraser-McKelvie *et al.* (2018). The dashed line is where bulge and disk parameters are equal.

star formation in its history, of varying duration and intensity. Determining when and where these occurred, and for how long, can shed new light on the formation history of the components.

One of the outputs of the spectroscopic decomposition method is a high S/N global bulge and disk spectrum, constructed by taking the best-fitting spectrum found by pPXF for each component in each bin, and combining them into a flux-weighted average. These can then be fitted with pPXF, recording the SSP model spectra and weights used for each, which, when multiplied with the mass-to-light ratio for each stellar population, provides the fraction of mass at each age and metallicity. This gives the contribution from each stellar population in each component, and therefore the history of when and where stars formed in the galaxy.

The results of this analysis are shown in Figure 4.8, with the age of the populations plotted against their metallicities, where the colour corresponds to the log of the mass fraction of the populations averaged over the full galaxy sample. Similar to the average ages and metallicities, it appears that there is very little difference between the star-formation histories of the bulges and disks, with the majority of stars being old and metal-rich, though, as indicated by the light-weighted averages, there is also an interesting tail leading to more metal-poor populations.

The variation in metallicity with mass demonstrated in the averaged values also indicates a difference in star-formation histories for different stellar masses. Figure 4.9

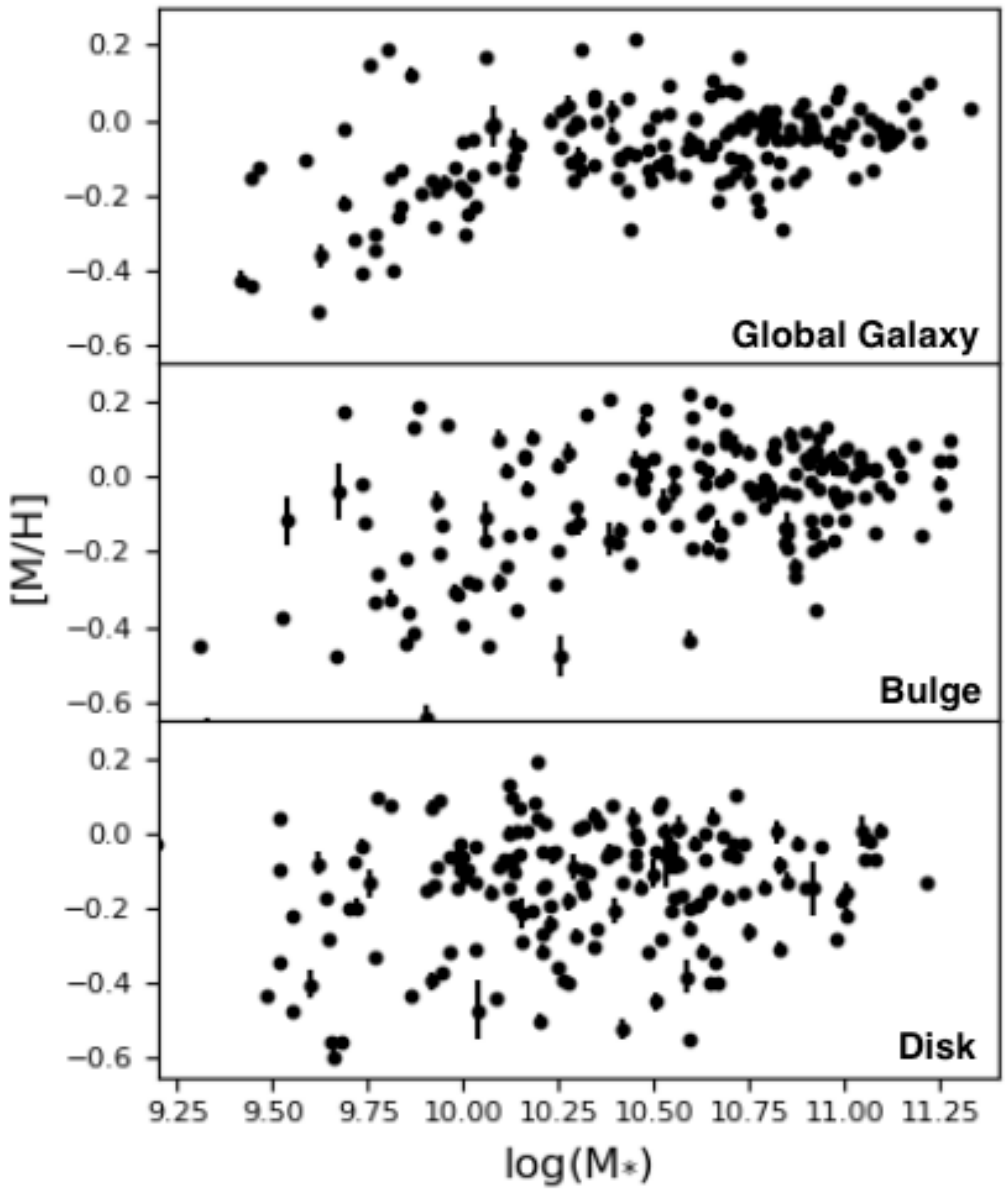


Figure 4.7: Mass–metallicity relation for the global galaxy (top) bulge (centre) and disk (bottom). Component masses are approximated by $M_* \times B/T$ and and $M_* \times (1 - B/T)$ for the bulge and disk respectively. This assumes the same mass-to-light ratio in the components which is an approximation, but a reasonable one given their similar stellar populations. One sigma error-bars are shown but are often too small to be visible.

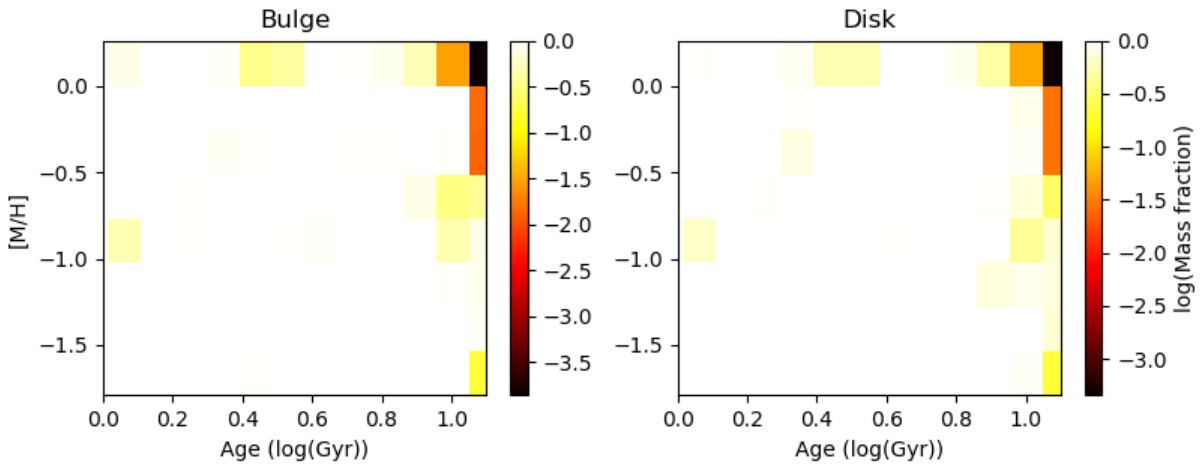


Figure 4.8: Star-formation histories of bulges and disks. The ages and metallicities of all the templates used, coloured by the log of the mass fraction assigned to each by pPXF.

shows the galaxy sample split into high mass ($\log(M_*) > 10$) and low mass ($\log(M_*) \leq 10$) groups. While the difference is not large, the lower mass galaxies show a slightly larger range of ages and metallicities in both the bulge and disk components, indicating a more diverse star-formation history than the higher mass galaxies, which are fairly uniformly old and metal-rich.

This difference in star-formation histories depending on mass agrees with previous work such as that of González Delgado *et al.* (2017), and illustrates the variety of evolution scenarios necessary to form early-type galaxies. While the uniformly old and metal rich populations of high-mass galaxies indicate a rapid early star-formation event, the more diverse populations of low-mass galaxies suggest a more gradual evolution, over which multiple periods of star formation have occurred. However, the differences are slight, and extension to a wider range of stellar masses will be necessary before we can be certain that these variations hold.

4.3 Kinematics

In studying galaxy kinematics, various parameters have been used to quantify the rotation of a galaxy, each with its own merit. In all cases the degree of rotation has been demonstrated to depend on various morphological properties, in particular with stellar mass and with bulge-to-total ratio, or proxies such as Sérsic index and velocity dispersion σ_e (Romanowsky & Fall, 2012; Cortese *et al.*, 2016; Krajnović *et al.*,

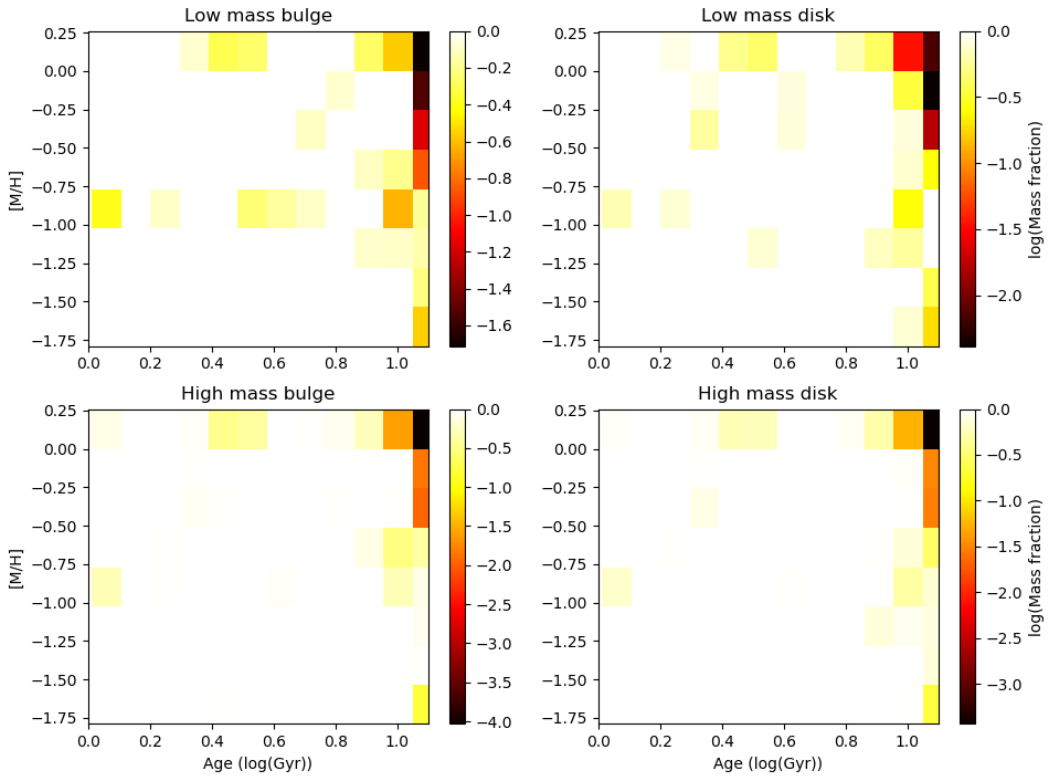


Figure 4.9: Same as Figure 4.8, but divided into two mass groups of $\log(M_*) \leq 10.5$ and $\log(M_*) > 10.5$. It is clear that the lower mass galaxies show more diverse star-formation histories, in both the bulge and disk, than the higher mass group. Within both mass groups the disks tend to show a higher range of ages and metallicities than the bulges.

2013; Graham *et al.*, 2018). This dependence demonstrates that bulges and disks play a key role in determining the evolutionary path of a galaxy, a role which is hard to determine without understanding the kinematic properties of the individual components themselves. Using our decomposed kinematics we can, for the first time, extract and quantify the kinematic properties of the individual components for a large sample of galaxies, and therefore understand how they contribute to the global kinematics of the galaxy.

4.3.1 Specific angular momentum

The angular momentum j_*, where the projected value is defined as

$$j_{\rm p} = \frac{\sum F_{\rm i} R_{\rm i} \mid V_{\rm ilos} \mid}{\sum F_{\rm i}}, \tag{4.2}$$

where F_i, R_i and $V_{\rm ilos}$ are the flux, radius and line-of-sight velocity of the i^{th} bin in the galaxy, has been shown to depend on the stellar mass of the galaxy (Fall, 1983), with a scatter that depends on various morphological parameters, such as Sérsic index and bulge-to-total ratio (Fall, 1983; Cortese *et al.*, 2016). Romanowsky & Fall (2012) hypothesised that the location of a galaxy on the $M_* - j_*$ plane is therefore determined by the relative contributions of the bulge and disk, each of which should, in theory, follow their own distinct $M_* - j_*$ relation. They, and more recently Fall & Romanowsky (2018), used strong simplifying assumptions to estimate j_* values for bulge and disk components within their galaxies which indicated that the components do indeed follow their own $M_* - j_*$ relations, with bulges offset to lower j_* values, similar to elliptical galaxies, and disks lying in similar regions to late-type disk galaxies. This was also explored by Rizzo, Fraternali & Iorio (2018), who decomposed bulges and disks of 10 S0 galaxies in order to compare the $M_* - j_*$ relation of their disks to those of spiral galaxies, which they found to be very similar. With our decomposed kinematics we can extend this analysis to determine more rigorously, for a large sample of galaxies, where bulges and disks lie on the $M_* - j_*$ plane.

In order to determine the intrinsic angular momentum, j_*, the galaxy must be deprojected. This requires knowing the intrinsic axial ratio, q_0, of the galaxy, a property which is highly uncertain for galaxies as a whole, and even more so for individual components. We therefore do not attempt to correct for inclination here, and instead look at the projected angular momentum j_p. While this will introduce some additional scatter into the relations, it should not have a significant effect on the comparison between bulge and disk angular momentum.

Figure 4.10 demonstrates how the position of a galaxy on the $M_* - j_p$ plane varies with bulge-to-total ratio, with lower B/T galaxies tending to have higher values of j_p at a given mass. The dependence of the scatter on B/T is not as prominent as found for previous studies, most likely due to the relatively small range of B/T in our sample, but is still significant, with j_p correlated with B/T with a p-value $= 0.002$. It also shows the distinct $M_* - j_p$ relations when bulges and disks are decomposed, both when j_p is determined within $1\mathrm{R_e}$ as well as in overlapping regions. There is a clear offset between bulge and disk, with the global galaxy lying between the two components,

though since these are early-type galaxies the majority have a high bulge fraction, resulting in the global values tending to lie closer to those of the bulge than the disk. For the values of j_p calculated in the overlapping regions, the offset between bulge and disk is slightly smaller, implying that part of the separation in the $1\mathrm{R_e}$ values is due to aperture effects, but it is still clear that the components have systematically different angular momenta. The disks lie within the same region as found by previous studies for late-type spiral galaxies (Fall, 1983; Cortese *et al.*, 2016), i.e. galaxies with very low bulge-to-total ratios, as well as the separated disks in Romanowsky & Fall (2012).

The relatively tight correlation in the disks of these galaxies, some of which are classed globally as slow rotating galaxies, demonstrates the remarkable consistency of the properties of these disks across all morphologies. There is a fairly large scatter in the relations for both components, which is expected as this is the projected angular momentum rather than the intrinsic angular momentum, resulting in a scatter purely due to the range in inclination.

The right-hand panel of Figure 4.10 demonstrates clearly how the global angular momentum varies according to the contribution of the components. For low B/T the global value of j_p is close to that of the disk, and as the B/T increases it moves closer to the value of the bulge. Due to difficulties inherent in a complex method such as this, there is some additional scatter in the values of j_p for the individual components, which is why j_p of the bulge in high B/T galaxies is occasionally higher than that of the global galaxy. This is not a physical phenomenon, and is just due to the difference between the bulge and global values of j_p scattering around zero for the very bulge-dominated galaxies.

The angular momentum of the components is also clearly correlated, albeit with a large scatter, as shown in Figure 4.11. This demonstrates a coupling of the components, suggesting that, as indicated by the stellar populations in Section 4.2, the evolution of the two components is not independent.

Interestingly, we find no clear correlation between the kinematics of bulges and their Sersic index, a parameter often used as a proxy for morphology, and even, sometimes, for kinematics to determine how 'disky' a bulge is. This agrees with previous work by Méndez-Abreu *et al.* (2018), who compared photometric and kinematic properties

of field S0 galaxies in the CALIFA survey, and concluded that photometric parameters are not a good proxy for kinematics.

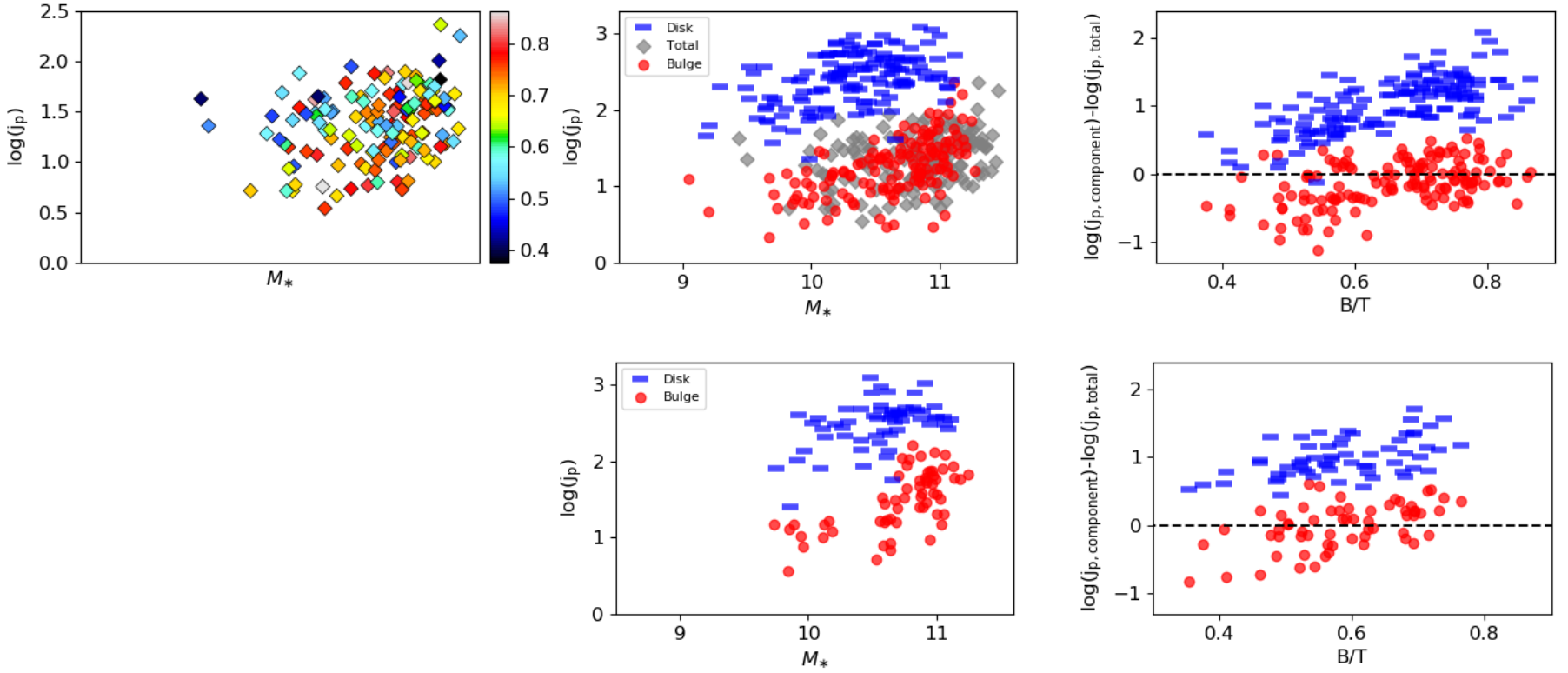


Figure 4.10: Top left: angular momentum vs. stellar mass for global galaxy, coloured by bulge-to-total ratio. Middle: angular momentum vs. stellar mass for decomposed bulge and disk and global galaxy, where the stellar mass of the individual components is approximated by $M_* \times B/T$ for the bulge and $M_* \times (1 - B/T)$ for the disk. The top-centre panel shows the values for the bulge and disk calculated within $1\mathrm{R_e}$. The relations for both bulge and disk are significant with p-value $= (1.7 \times 10^{-13}, 3 \times 10^{-9})$ and r-value $= (0.57, 0.47)$ for bulge and disk respectively. The bottom-centre panel shows the same relations but with the values calculated for overlapping bulge and disk regions. Top right: the difference between the global values of j_p and the component values for varying bulge-to-total ratio. Bottom right: the same as bottom left but calculated across overlapping bulge and disk regions.

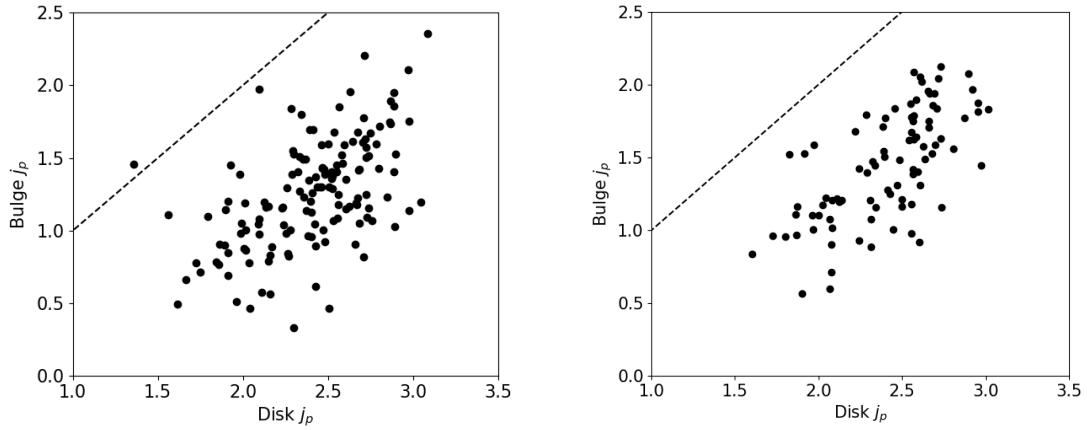


Figure 4.11: Projected specific angular momentum of the bulge and disk components, correlated with r-value = 0.55, p-value=2.3×10^{-12} from a linear regression fit. The dashed line shows a one-to-one correlation. The left hand panel shows the relation for j_p determined within $1\mathrm{R_e}$, while the right hand panel shows the relation for j_p within the overlapping regions.

4.3.2 Stellar Spin Parameter, λ_R

A related quantity, the stellar spin parameter, λ_R, defined in Equation 4.1, is a useful way of determining the relative contributions of rotational and random motions in a galaxy. The location of a galaxy on the plane of λ_R and ellipticity, ϵ, has been shown to depend on the bulge-to-total ratio of the galaxy (Krajnović *et al.*, 2013), demonstrating that, as for the $M_* - j_*$ relation, the relative contributions of bulges and disks play a key role in determining the global properties of a galaxy. This effect is shown in the left panel of Figure 4.12 for this sample. Using the decomposed kinematic maps we can also calculate this parameter for the individual components. Figure 4.12 shows λ_{Re} – λ_R calculated within one R_e – for each component, plotted against ellipticity, obtained for the individual components from the GALFIT decomposition. The contours correspond to the locations of galaxies based on dynamical models for different intrinsic ellipticities and inclinations. The values of λ_{Re} have not been corrected for seeing, a correction which results in a relatively moderate increase in λ_{Re}. This increase is detailed in Graham *et al.* (2018), though there is a large uncertainty in these values.

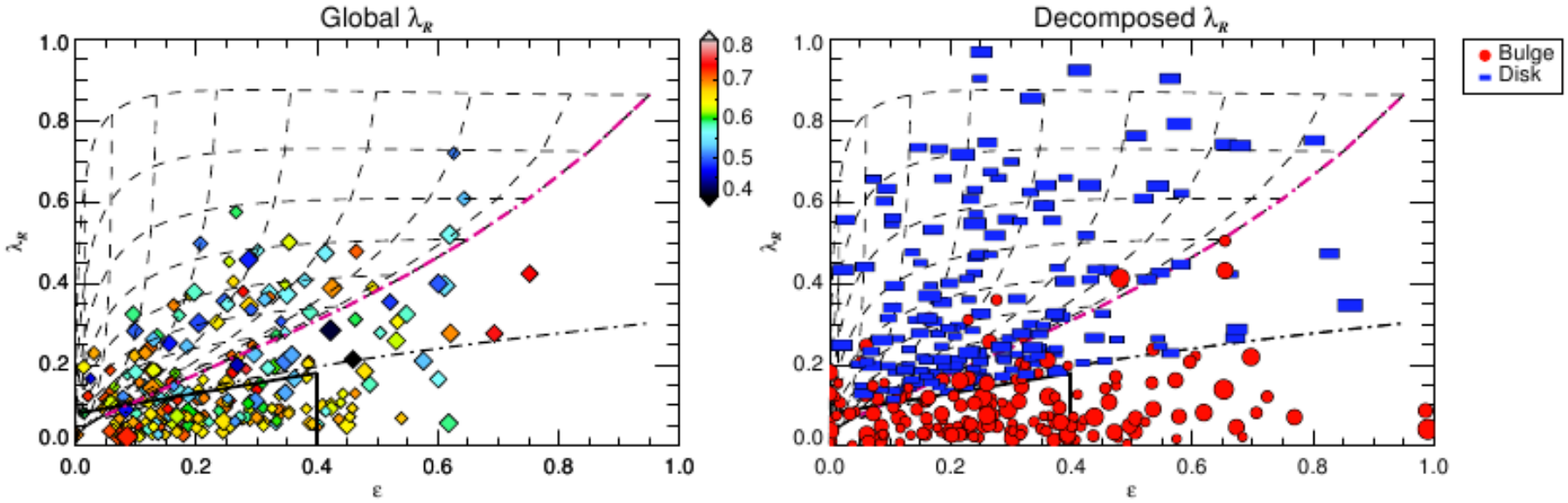


Figure 4.12: Stellar spin parameter λ_{Re} vs ellipticity, ϵ, for the global galaxy on the left, coloured by bulge-to-total ratio, and for the decomposed bulge and disk on the right. The blue bars correspond to disk components and the red circles correspond to bulges. The dashed contours correspond to dynamical models with $\delta = 0.7 \times \epsilon$, as described in Cappellari *et al.* (2007), for varying intrinsic ellipticities and inclinations, with the magenta line corresponding to edge-on galaxies. The dot-dashed line and solid black line correspond to the slow-fast rotator divide as defined by Emsellem *et al.* (2007) and Cappellari (2016) respectively. The decomposed bulges tend to lie at low values of λ_{Re}, while disks lie at higher values. The global values of the galaxy are determined by the combination of the two components. Note that since the bulges and disks sit within the global potential of the galaxy, they can not be directly mapped to intrinsic dynamical properties in the same way as for galaxies as a whole. This figure is included to illustrate the relative positioning of the components, not to provide a detailed interpretation of their dynamical properties.

It is clear that when the components are separated the disks tend to occupy regions of higher λ_R, whereas the bulges tend to sit in lower regions, towards the slow-rotator region. Interestingly, many slow-rotator galaxies still show signs of a disk, the existence of which agrees with work by Krajnović *et al.* (2013) who compared photometric decompositions with the kinematic signatures in early type galaxies from the ATLAS^{3D} sample and found that 29% of slow rotators still appear to contain an exponential component. They demonstrate that there appears to be a transitional region between fast and slow rotators, including slow rotators that contain an exponential disk (e.g. Li *et al.*, 2018), and fast rotators that are not described by an exponential profile.

The majority of disks sit within the contours showing the locations of dynamical models, satisfying the anisotropy condition, $\delta = 0.7 \times \epsilon$ (see Cappellari *et al.*, 2007, and Chapter 5 for a detailed description) for varying intrinsic ellipticities and inclinations. While the global kinematics do not neatly fit into a particular dynamical model, being distributed across the slow/fast-rotator divide, the individual components for the most part do. Some caution is necessary in the interpretation of this figure; since bulges and disks are not self-gravitating systems, their location on the $\lambda_R - \epsilon$ plane cannot be mapped directly to their intrinsic dynamical properties. This issue is addressed in Chapter 5, and here we simply use the figure as a way to illustrate heuristically the separation of the components. Figure 4.13 shows the $\lambda_R - \epsilon$ distribution for values calculated over the overlapping bulge and disk regions. While the components are more widely distributed than in Figure 4.12, the disks still clearly lie at higher values of λ_R than the bulges, showing that the difference in the components is not simply due to the difference in radius. Dynamical modelling provides an additional way of accounting for these problems, allowing extraction of the intrinsic kinematic properties of the components, irrespective of radius. The results of this are presented in Chapter 5. Similar to the location of a galaxy in the $M_* - j_*$ relation, this difference in the properties of the components again points to the global properties of a galaxy being determined by the relative contribution of the bulge and disk.

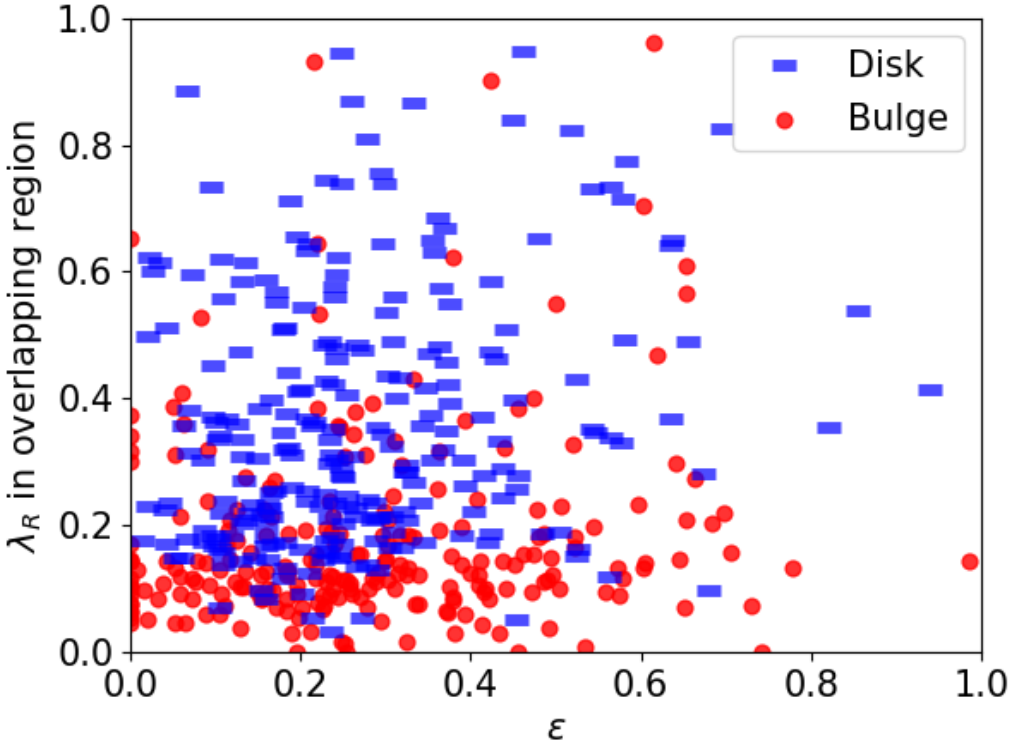


Figure 4.13: Same as for right hand panel of Figure 4.12 but with stellar spin parameter λ_R calculated within overlapping regions of bulge and disk to allow a direct comparison. While the bulges and disks are more widely distributed than in the Figure 4.12, disks still clearly tend to lie towards higher values of λ_R than bulges.

4.4 Applying spectroscopic decomposition to large IFU surveys

In this chapter we have demonstrated that spectroscopic decomposition can be successfully applied to large IFU surveys. However, applying any complex method, such as the one used here, to large numbers of galaxies is not a simple task. As demonstrated by the significant number of galaxies cut from the original sample, the decomposition cannot be applied to all galaxies, and will not always be successful. For the decomposition to work it requires high signal-to-noise data, and sufficient flux in both bulge and disk components.

A particular concern when applying this method on large IFU surveys is how the spatial resolution can affect the properties of the bulge. The cuts made on the sample remove components which have very few bins, and therefore remove the smallest bulges, however, there are still bulges in the sample which have effective radii comparable to the

FWHM of MaNGA observations. If this is having a significant effect on the resulting kinematics then we would expect that all bulges below a certain effective radius would have systematically lower angular momentum than larger bulges, due to the kinematics being smeared out. Figure 4.14 shows how the λ_{Re} values of the bulge vary with effective radius. While the lowest angular momentum bulges with $\lambda_{Re} < 0.1$ do tend to be fairly small, there are also many equally small bulges with high values of λ_{Re}, demonstrating that even in bulges that are not fully resolved some kinematic information can still be extracted.

A clear shortcoming of the work presented here is the lack of errors on kinematic parameters. Obtaining the errors is complex, but would be possible by running Monte Carlo simulations through pPXF. While this is beyond the scope of this thesis, work making use of this method in the future would benefit from extending the method to include such error analysis.

There are additional potential errors that may arise in the calculation of the parameters presented here. We have minimised the possibility of the parameters of individual bins of the the bulge and disk maps being wrongly assigned by constraining the relative flux of the components and, when the flux of the components is similar, by assigning the highest velocity component to the disk. However, for some bins, particularly if the photometric decomposition is not completely accurate, the pPXF outputs could still be wrongly assigned. While problematic, this would result in the calculated parameters for the two components being more similar to each other, as any differences would be washed out. We can therefore safely say that the differences between the components we see in the kinematic parameters do not result from fit wrongly assigning the properties of the bulge and disk. This issue could, however, cause the bulges to appear more rotationally dominated than they are in reality, by assigning some of the rotating disk bins to the bulge. Examining the kinematic maps by eye indicates that this is not the case for the vast majority of galaxies, with the kinematic maps mostly being smooth and consistent, while mis-assigned bins would be clearly incongruous. Constraining the stellar populations while fitting the kinematics, as we do here, also provides a way to limit this effect, though the general similarity in the stellar populations of the components may not be sufficient to always prevent the components from

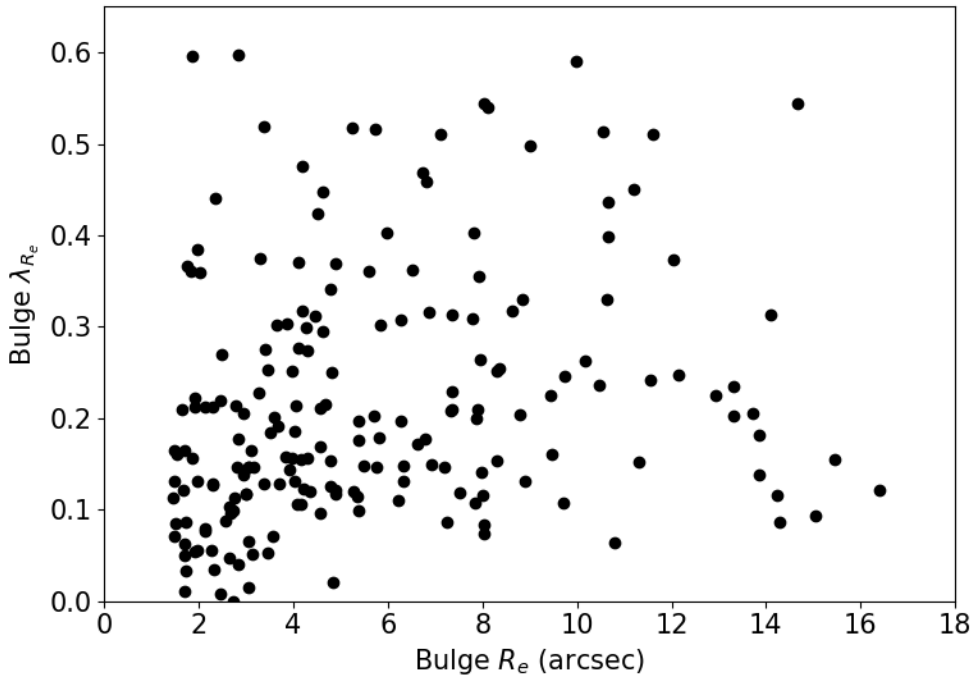


Figure 4.14: Bulge effective radius versus bulge λ_{Re}, showing that the kinematics can be extracted even for bulges with effective radii comparable to the FWHM of MaNGA data.

switching. Future work would benefit from incorporating checks on the assignment of the components into the fitting process.

While some care must be taken when applying this method to large samples of galaxies, providing the quality of data, the signal-to-noise and the morphology of the galaxies are suitable, and the resulting parameters are carefully checked, spectroscopic decomposition can reliably be applied to large IFU surveys.

4.5 Conclusions

In this chapter we have spectroscopically decomposed a sample of MaNGA early-type galaxies into bulge and disk components. This allows us to obtain stellar populations and kinematic parameters for the components separately, and look at their similarities and differences. The main conclusions are as follows:

- Bulges and disks have similar ages, but bulges are systematically offset to higher metallicities. Disks tend to span a wider range of both age and metallicity,

reaching much younger ages and lower metallicities, indicating a more varied star-formation history compared to the bulges.

- The larger spread in metallicity of the disk is also reflected in the star-formation histories of the components. While the stellar populations of the bulges tend to be uniformly old and metal-rich, the disks contain some younger, more metal poor populations.

- When separated into high and low mass populations, the galaxies exhibit different star-formation histories. While the higher mass galaxies, particularly the bulges, tend to be uniformly old and metal-rich, the lower mass group shows a much larger spread in age and metallicity in both the bulge and disk.

The kinematic properties of galaxies, specifically the stellar spin parameter, λ_R, and the specific angular momentum, j_*, have been shown to depend on the bulge-to-total ratio of the galaxy. Decomposing the bulges and disks allow us to understand the root of this dependence, showing that:

- Bulges and disks follow their own $M_* - j_p$ relations, with bulges offset to lower values of j_p compared to the disks. Where the galaxy as a whole sits on this relation is then determined by how much bulge and disk are present in the galaxy.

- A similar trend is seen for the position of bulges and disks on the $\lambda_R - \epsilon$ diagram, with bulges lying at lower values of λ_R than the global galaxy, while disks move to higher values.

The bulges and disks appear to be coupled, both in their stellar populations, which tend to be similar, and in their kinematics, with higher angular momentum bulges associated with higher angular momentum disks. This has interesting implications for the evolution of these galaxies, in particular whether this coupling can arise from galaxies which have undergone mergers. Findings related to this, both observational and in simulations, will be discussed in more detail in Chapter 6.

It is likely that no single evolutionary path applies to all early-type galaxies, even across similar morphologies and mass, but combining the stellar populations and kinematics of the components offers some critical insights into how each may be affected.

Chapter 5

JAM Dynamical modelling

"A certain type of perfection can only be realized through a limitless accumulation of the imperfect."

– Haruki Murakami

In the previous chapter we demonstrated that bulges and disks have different kinematic properties. This is illustrated by Figure 4.12, showing that bulges and disks lie in different areas of the $\lambda_R - \epsilon$ diagram, a strong indication that their intrinsic dynamical properties are different. However, treating bulges and disks as distinct and separable components is actually not entirely correct due to the fact that they are not self-gravitating systems, but rather sit within the global potential of the galaxy. While the location of a galaxy as a whole on the $\lambda_R - \epsilon$ diagram can tell us about its intrinsic dynamical properties, such as the anisotropy of the system, for individual components this is no longer the case. In addition, due to the calculated λ_{Re} only including bins where the component fraction is greater than 30%, the central regions of the disk and the outer regions of the bulge do not contribute towards the final value. This makes direct comparisons between the components difficult. Building dynamical models of galaxies provides a solution to this; by including individual bulge and disk components, the intrinsic dynamical properties of the components can be extracted in a self-consistent manner, over the same spatial ranges, therefore avoiding these issues.

In addition, by obtaining dynamical models of the components we can directly compare the kinematic properties of the components extracted through dynamical modelling to those extracted through spectroscopic decomposition, allowing us to check that the two decomposition methods give consistent results.

5.1 Dynamical models

Dynamical modelling has been shown to be a useful complementary way of studying the kinematics of galaxies. The three methods predominantly used to achieve this are the equations of stellar hydrodynamics of Jeans (1922), the orbit-superposition method of Schwarzschild (1979), and the N-body models of Syer & Tremaine (1996). These modelling techniques are based on the fact that the dynamics of galaxies can be fully described by the stellar distribution function and the gravitational potential of the galaxy. These, however, are not trivial to obtain with only the line-of-sight quantities, with large degeneracies arising even when strong simplifying assumptions are made.

Cappellari *et al.* (2007) demonstrated that IFU data could be used in conjunction with Schwarzschild modelling to extract key kinematic parameters in order to understand and quantify their dynamics. To this end, they introduce three parameters: β_z, γ and δ, where β_z describes the shape of the velocity dispersion tensor in the (v_r,v_z) plane, such that if the anisotropy is spatially constant

$$\beta_z = 1 - (\sigma_z/\sigma_R)^2, \tag{5.1}$$

and γ is the equivalent in the plane orthogonal to β_z, such that if it is spatially constant

$$\gamma = 1 - (\sigma_\phi/\sigma_R)^2. \tag{5.2}$$

For an isotropic system $\beta_z = \delta = \gamma = 0$. By modelling a sample of galaxies from the SAURON survey, it was found that on average $\delta \sim \beta_z$, $\gamma \sim 0$ and $\beta_z \gtrsim 0$. Along with observational studies (Gerssen, Kuijken & Merrifield, 1997; Shapiro, Gerssen & van der Marel, 2003; Noordermeer, Merrifield & Aragón-Salamanca, 2008), this indicates that the anisotropy of fast-rotator early-type galaxies can be approximated by a flattening of the velocity ellipsoid in the z direction parallel to the galaxy symmetry axis.

To implement these findings, Cappellari (2008) developed a method of dynamically modelling a galaxy as a cylindrically aligned velocity ellipsoid with general axial ratios $\sigma_R \neq \sigma_z \neq \sigma_\phi$. Known as the Jeans Anisotropic Modelling method (JAM), this is an anisotropic generalization of the semi-isotropic (two-integral) axisymmetric Jeans formalism presented by Emsellem, Monnet & Bacon (1994). It is important to note that this cylindrical alignment is an approximation, and cannot be accurately satisfied in real galaxies. However, the comparisons between the models and IFU observations show that, assuming a cylindrically aligned velocity ellipsoid of constant anisotropy, the kinematics of fast-rotator early-type galaxies can be effectively reproduced. This method of modelling galaxies provides a simple and effective way of obtaining their dynamical properties.

Increasing evidence, however, indicates that representing galaxies as single systems is, in many cases, not accurate. Galaxies are composed of multiple components and, as demonstrated in the previous chapters, these components have different kinematics. Having distinct kinematics does not necessarily mean the anisotropy of the components is different; for example the ratio of σ_z/σ_R could be the same for bulges and disks, leading to the same value of β_z, even if the values of σ_z and σ_R are very different, as is expected given the well accepted fact that bulges have higher velocity dispersion than disks. However, given the different formation scenarios for bulges and disks and the myriad of processes which can effect the orbits of the stars within them, it would be somewhat surprising, and very interesting, if this ratio ended up being the same for both components, particularly when external accretion and mergers play a role, as they likely have done to build such bulge-dominated galaxies as these. Using a single dynamical model to describe the entire galaxy without accounting for these components may, therefore, be neglecting this variation within galaxies, which could in itself provide interesting insights into the the extent to which bulges and disks are truly coupled.

The motivations for building dynamical models of our sample are therefore threefold:

- To understand the intrinsic dynamical properties of bulges and disks, which cannot be extracted through the normal observational routes such as the position of a system on the $\lambda_R - \epsilon$ diagram.

- To check whether the kinematic properties obtained through dynamical modelling of bulges and disks are consistent with those obtained through spectroscopic decomposition.

- To compare to previous work finding that galaxies are well described using a single anisotropy, implying that bulges and disks do not have intrinsically different dynamical properties. Using dynamical modelling we can determine whether the dynamical properties of the components are systematically the same, or different.

5.2 Building the models

To produce dynamical models of the individual components, we use the Jeans Anisotropic Modelling method (JAM), as it allows us to produce simple models of the system, while allowing for different dynamical properties in different regions of the galaxy. We apply this modelling technique to a subset of the sample of spectroscopically decomposed galaxies from Chapter 4, selecting 50 galaxies with the highest signal-to-noise and cleanest rotation fields, chosen by eye, for which such complex modelling is suitable.

To model the kinematics of the individual components, we require the three-dimensional distribution of light and mass of each component within the galaxy. These are derived using the Multi-Gaussian Expansion (MGE) method (Emsellem, Monnet & Bacon, 1994) with software developed by Cappellari (2002) to fit the bulge and disk images created by GALFIT during a photometric decomposition, as described in Section 4.1.1. An example of the MGE fit to the bulge and disk contours is shown in Figure 5.1. This surface brightness distribution is then deprojected to produce the luminosity density, and, assuming a constant mass-to-light ratio, this is then converted to a stellar mass distribution. Since both components sit in the global potential of the galaxy, likely dominated by stellar mass at these radii, we combined the mass distributions of both components to form a global potential.

The JAM fitting consists of two steps; first, with the luminosity density obtained, the galaxy $V_{\rm rms} = \sqrt{V_{\rm los}^2 + \sigma^2}$ can be fully described by the anisotropy parameter,

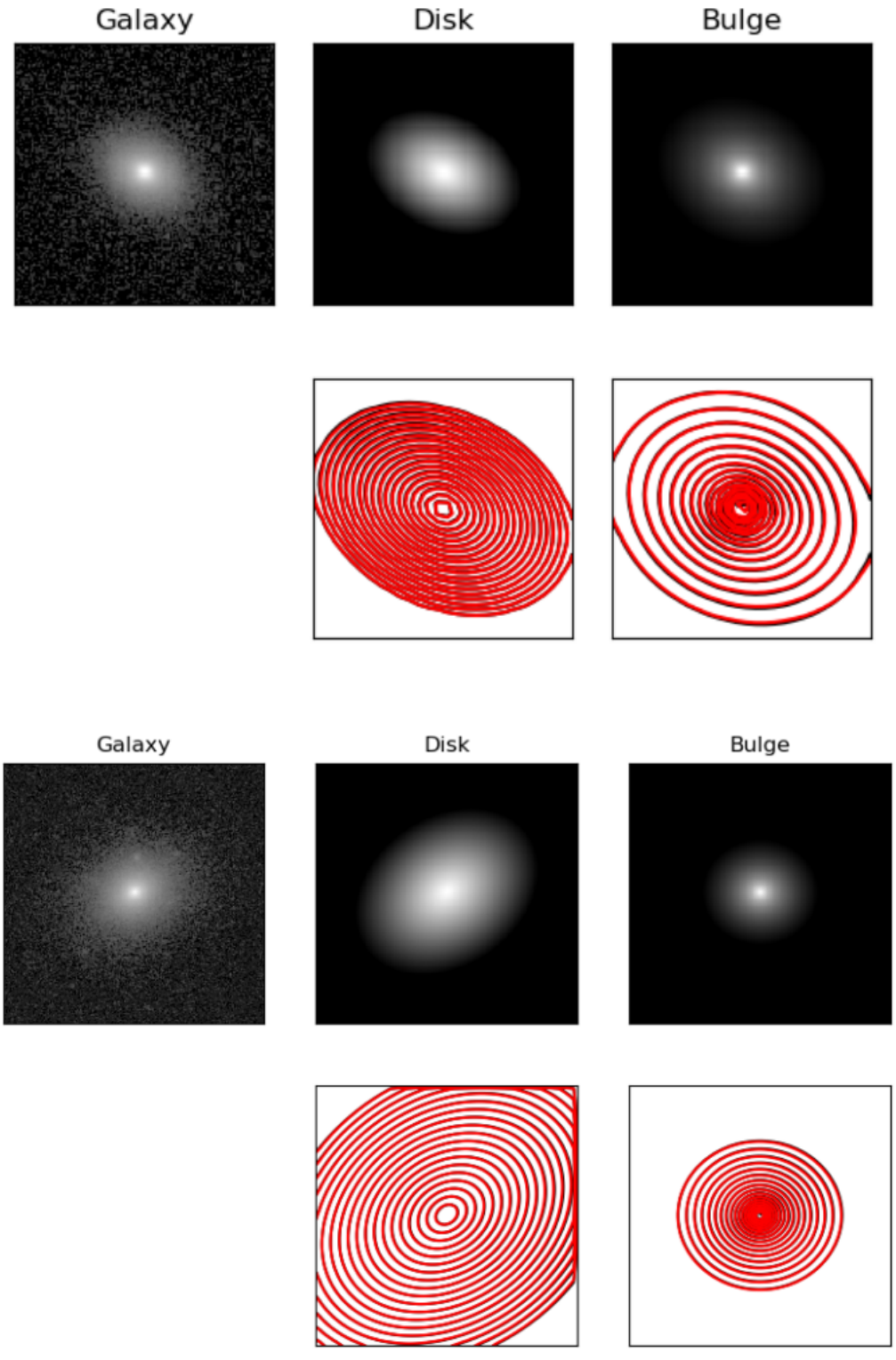


Figure 5.1: Photometric analysis of two example galaxies. Top rows: SDSS r-band image and GALFIT decomposed bulge and disk. Bottom rows: corresponding MGE fit (red) to bulge and disk flux contours (black).

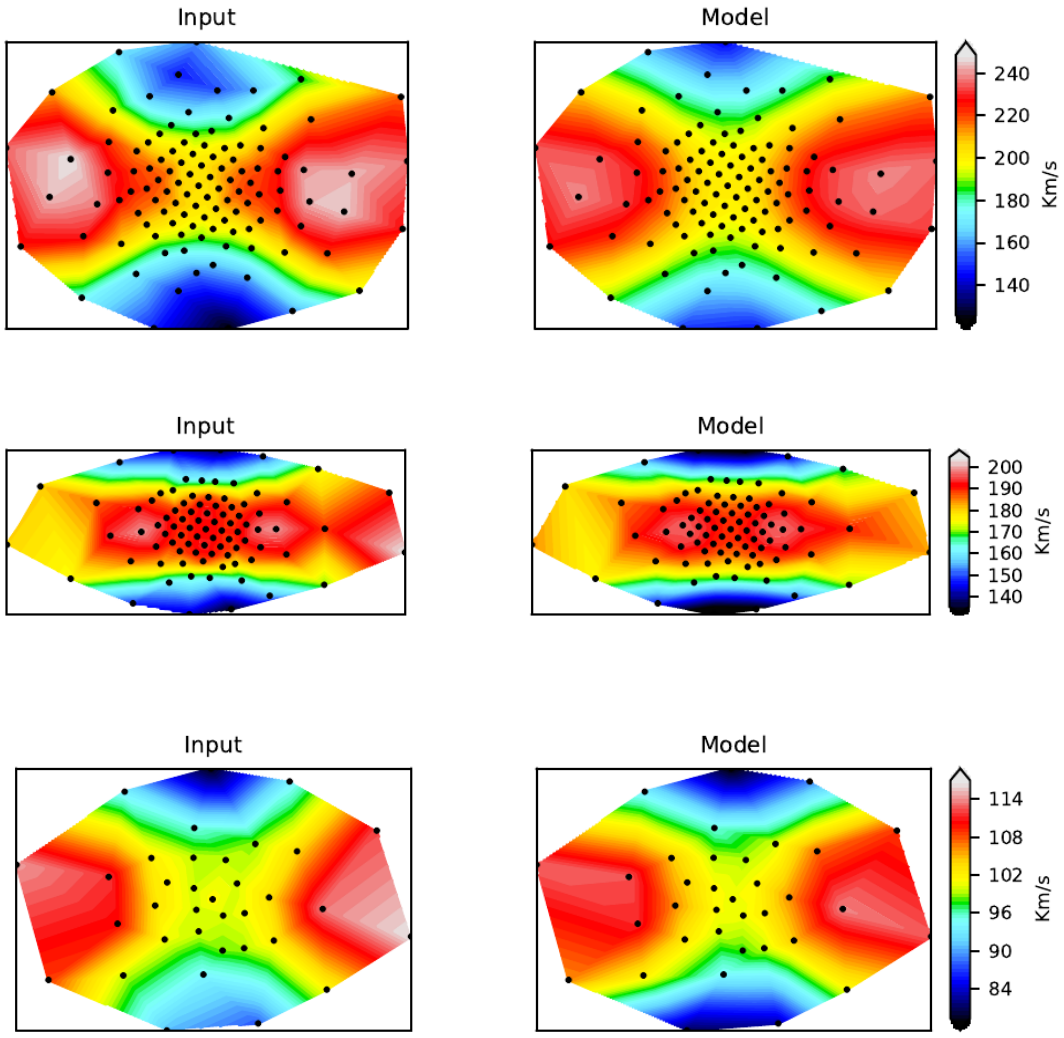


Figure 5.2: Observed $V_{\rm rms}$ (right) and JAM best-fit model $V_{\rm rms}$ (left) for three galaxies in the sample. The dots show the locations of the Voronoi bins. To avoid large degeneracies in the fits we use these global values of β in the following step to fit the $V_{\rm los}$ maps.

$\beta_{\rm z} = 1 - (\sigma_{\rm z}/\sigma_{\rm R})^2$, the inclination and the mass-to-light ratio. We find the best fitting combination of these parameters by minimizing the residuals $(V_{\rm rms})_{\rm obs} - (V_{\rm rms})_{\rm model}$ using a least-squares fit. Some examples of the data and the best-fitting models are shown in figure 5.2. Assuming the same mass-to-light ratio for the bulge and disk will not always be a realistic assumption, but for early-type galaxies such as these, where the bulge and disk have been found to be composed of similar stellar populations, this should not be a problem. When applying this analysis to late-type galaxies, where the stellar populations, and therefore the mass-to-light ratio, of the components can be radically different, a varying mass-to-light ratio should be permitted.

Second, using these parameters, a model for the line-of-sight velocity, $V_{\rm los}$, can be

constructed, described by a parameter, κ, defined as the amount by which an isotropic velocity field of $\sigma_\phi = \sigma_{\rm R}$ must be scaled to fit the data. A large value of κ implies faster rotation, with the sign specifying the direction of rotation, and $\kappa = 0$ implies no rotation. A galaxy best fit by a model of $\kappa = 1$ implies that an isotropic velocity field where $\sigma_\phi = \sigma_{\rm R}$ is a good description of the galaxy dynamics. Assigning different values of $\beta_{\rm z}$ and κ to the bulge and disk luminosity densities allows us to parameterise the components individually.

However, in general measuring the velocity dispersion of a spectrum is more difficult than measuring $V_{\rm los}$. This introduces additional uncertainties in the modelling of $V_{\rm rms}$ and allowing for two different values of $\beta_{\rm z}$ only increases the degeneracies of the fit. We therefore do not allow the two components to have different β_z and only allow for two components in the fit to $V_{\rm los}$, i.e. allowing for two values of κ. Since the value of $\beta_{\rm z}$ used in the fitting of $V_{\rm los}$ does not have a significant effect on the value of κ obtained, we use the single global value of $\beta_{\rm z}$ in the fits to $V_{\rm los}$ for both components.

To determine the dynamical properties of the bulge and disk, we construct a model using two different κ values for the luminosity density of the bulge and disk. As for the single component model, we find the best fitting model of $V_{\rm los}$ for a given $\kappa_{\rm bulge}$ and $\kappa_{\rm disk}$ by minimising the residuals $(V_{\rm los})_{\rm obs} - (V_{\rm los})_{\rm model}$ using a least-squares fit.

All the galaxies in the sample were visually inspected to ensure that the models, both for a single component and two components, were a good description of the data. Due to unsatisfactory photometric decompositions and complicated kinematics, or the JAM fitting failing, a number of galaxies were discarded from the final sample, leaving a core of 29 dynamically simple fast-rotating early-type galaxies.

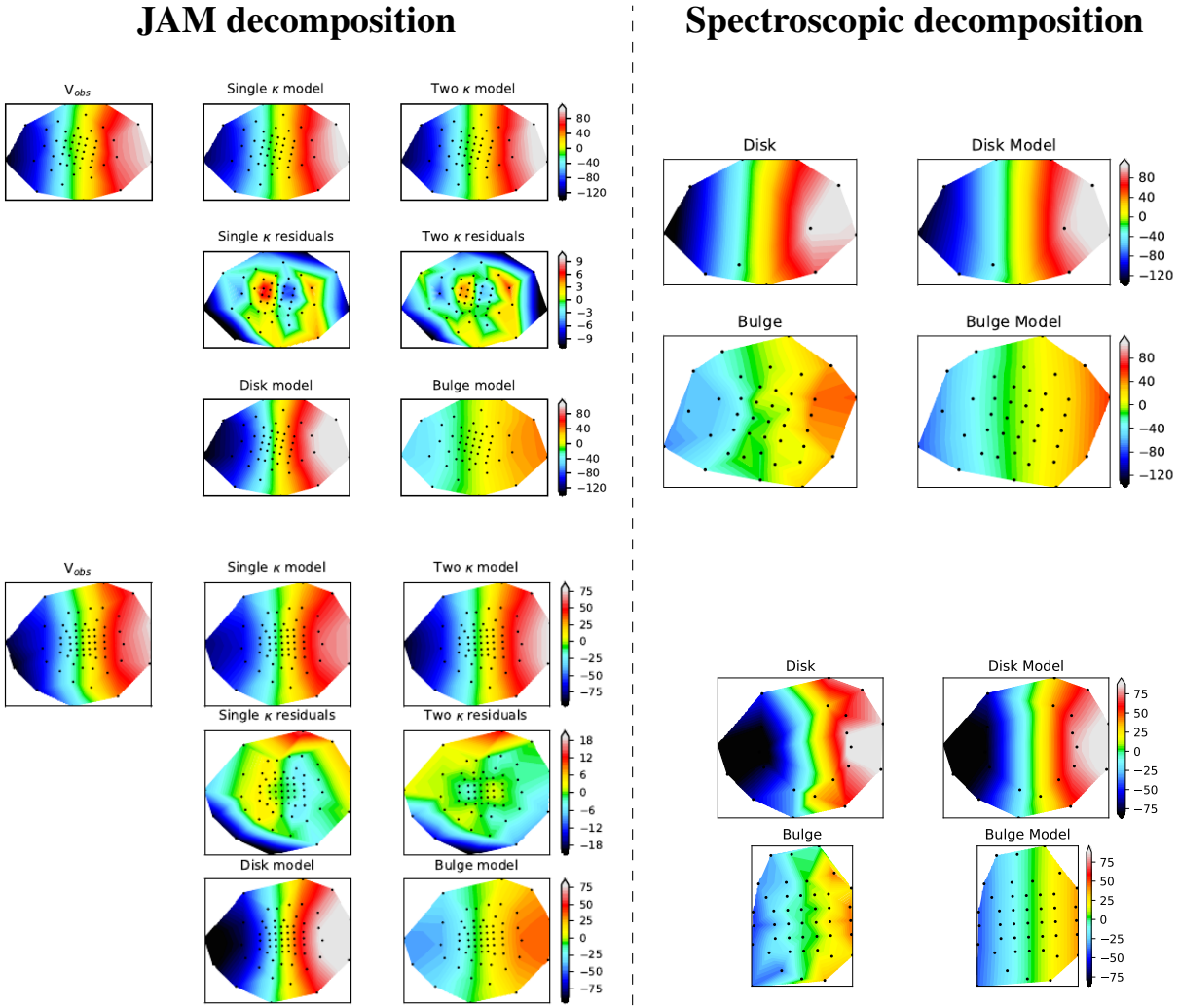


Figure 5.3: On the left are the kinematic maps and the best fitting JAM models for two galaxies in the sample, fitting with a single component and with two components. On the right are the maps from the spectroscopic decomposition and their best fitting JAM models for the same two galaxies. The black points show the locations of the bins. Note that the maps for the individual components only fit the points where the component contributes greater than 50% of the flux, therefore they cover a smaller area than the maps of the global velocity field. The velocity maps for the components obtained through dynamical modelling agree well with those obtained through spectroscopic decomposition.

To compare the kinematics of the components found though the JAM modelling to those obtained through spectroscopic decomposition, we repeat the above process, but fitting the individual JAM model component velocity fields to those obtained from the spectroscopic decomposition. This gives a second value of κ for both the bulge and the disk, which we can compare to the values from the fits to the global galaxy velocity field. To ensure the reliability of the kinematics, we only use bins where the flux of the component is greater than 50% of the total flux. The velocity maps and resulting JAM models for two galaxies in the sample are shown in Figure 5.3, demonstrating that the velocity maps of the components from the spectroscopic decomposition, shown in the right-hand panel, agree well with those from the dynamical modelling shown in the left-hand panel.

5.3 Comparing spectroscopic decomposition to dynamical modelling

The values of κ using a single component model are shown in Figure 5.4. The peak at $\kappa = 1$ agrees with Cappellari (2016), who found that a model with an oblate velocity ellipsoid ($\sigma_\theta = \sigma_\mathrm{R}$) is a good description of the kinematics of most fast rotators.

Figure 5.5 shows the κ parameter for the bulges and disks, both from the fits to the global velocity field, and from the fits to the spectroscopically decomposed components. For the majority of galaxies the values of κ show good agreement between the two decomposition methods. Notably, while κ_disk tends to be around, or slightly greater than, 1, κ_bulge tends to be less than 1. There is also a group of galaxies that show a negative κ for the bulge component in the JAM fits to the global velocity field, implying counter–rotation. There is, however, no indication of a counter rotating component from the observed kinematic maps or from the spectroscopically decomposed components, making it likely that this is not a physical phenomenon, but an effect of the JAM modelling process failing to account for models that deviate significantly from the simple case of an oblate velocity ellipsoid at all radii.

Figure 5.6 shows a histogram of the component κ values with the galaxies with neg-

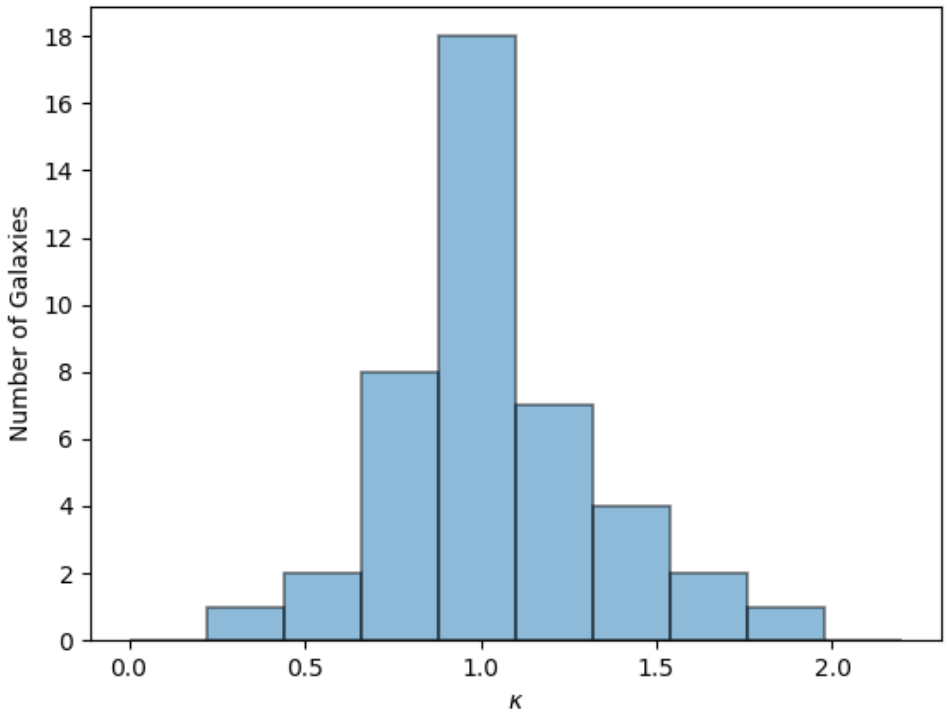


Figure 5.4: Histogram of κ, the ratio of the observed velocity to the velocity field predicted by a JAM model with $\sigma_\phi = \sigma_R$, for a single component JAM model. The distribution of these values is consistent with Cappellari (2016), finding that fast-rotator galaxies tend to have $\kappa \sim 1$.

ative bulge κ removed. A T-test, measuring the null hypothesis that two samples have identical average values, gives a T-value of 6.99 and 1.46 for the spectroscopically decomposed and dynamically decomposed components respectively, with P-values of 1.45×10^{-5} and 0.16, demonstrating that the difference between the components is clearly statistically significant, though less significant for the components extracted through dynamical modelling of the global velocity field than for those extracted through spectroscopic decomposition.

The differences between the components is clear when we look at how the values of κ for each component correlate with the global values, as shown in Figure 5.7. There is a clear correlation between the component and global values of κ, but with the bulges offset to lower values than the disks. This also agrees with findings in the previous chapter of this thesis, indicating that bulges and disks, while kinematically distinct, are also coupled.

It is interesting to compare the bulge and disk κ values to those found for regular and non-regular rotators in Cappellari (2016), with regular rotators tending to have $\kappa \sim 1$

while non-regular rotators have $\kappa \sim 0$. Bulges, while having lower values of κ than the disks, still have higher κs than slow-rotators, and for the most part are consistent with the lower tail end of the distribution of κ for fast-rotator galaxies when considered as a whole.

Indications of differences in bulge and disk anisotropies in spiral galaxies have been found using Schwarzchild modelling. Zhu *et al.* (2018) found radial variations in σ_r/σ_t and σ_z/σ_r, with values decreasing from the central bulge-dominated regions to the outer disk-dominated regions, corresponding to lower anisotropies in the bulge compared to the disk. Similarly, Gerssen & Shapiro Griffin (2012) found that the ratio of vertical to radial dispersion varies across Hubble type, increasing from late-type Sd galaxies to Sa galaxies. While there are several potential disk-heating mechanisms that could lead to this evolution, a simple solution would be that the variation arises due to increasing bulge-dominance in earlier-type galaxies, leading to lower global anisotropies.

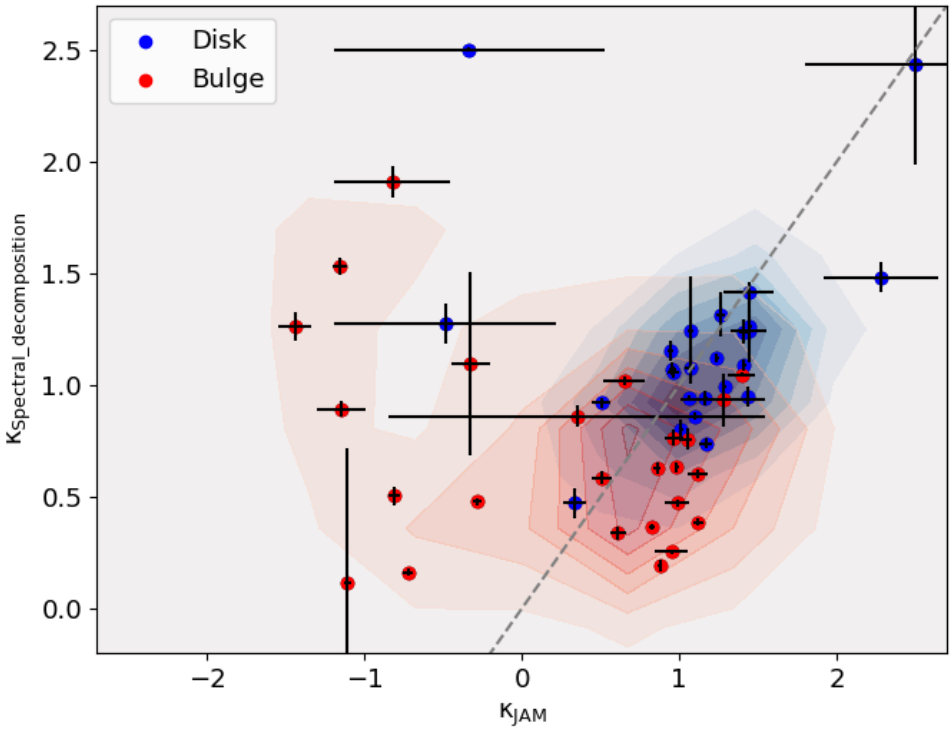


Figure 5.5: Comparison between κ values obtained through JAM modelling of the global velocity field, and those obtained through JAM modelling of the spectroscopically decomposed components. Error-bars correspond to $1-\sigma$ errors calculated by the minimization function. Contours show the density of points. The κ values obtained through the two decomposition methods are consistent, and the agreement in finding an offset in κ values for the bulge and disk demonstrates that bulges and disks have systematically different dynamical properties. However, these differences are not large and both the bulges and disks have κ values consistent with those of fast-rotator galaxies considered as a whole.

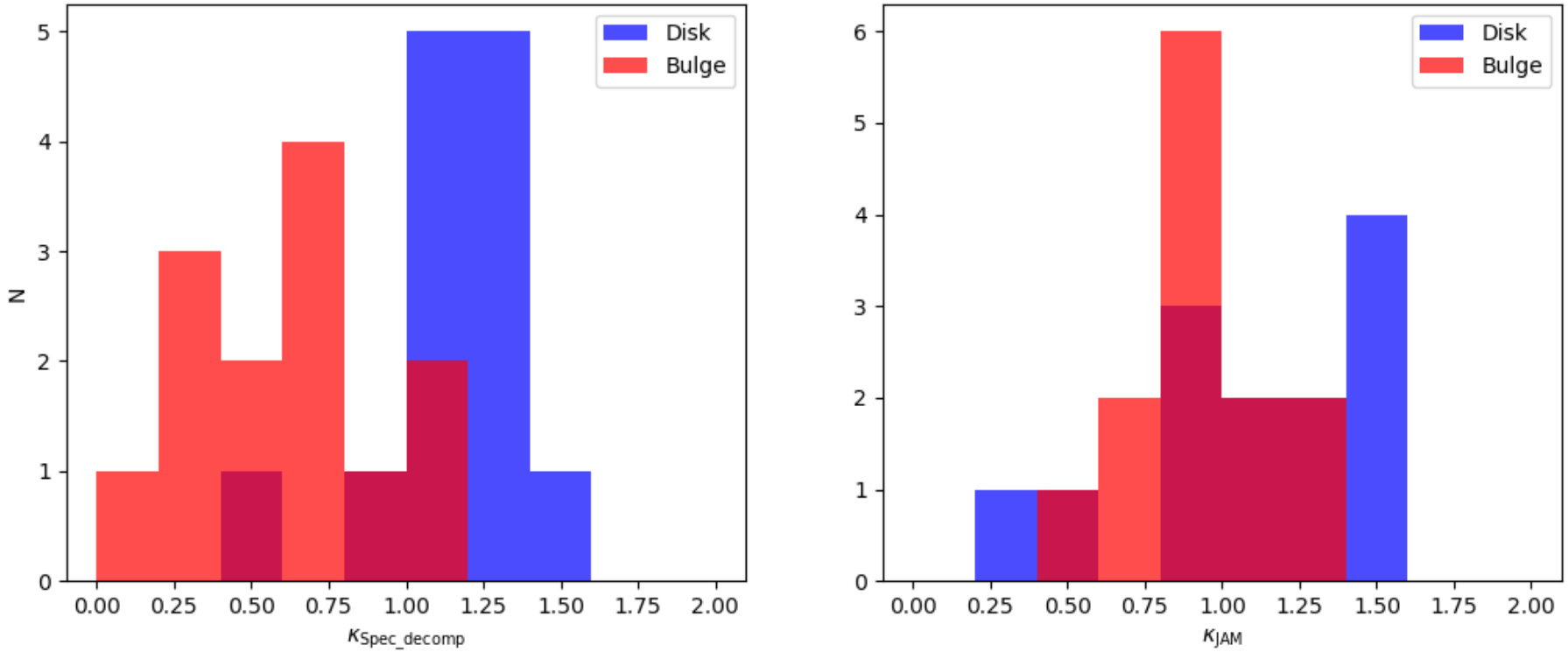


Figure 5.6: Histogram of bulge and disk κ values for the spectroscopic decomposition on the left and for the JAM modelling of the global velocity field on the right.

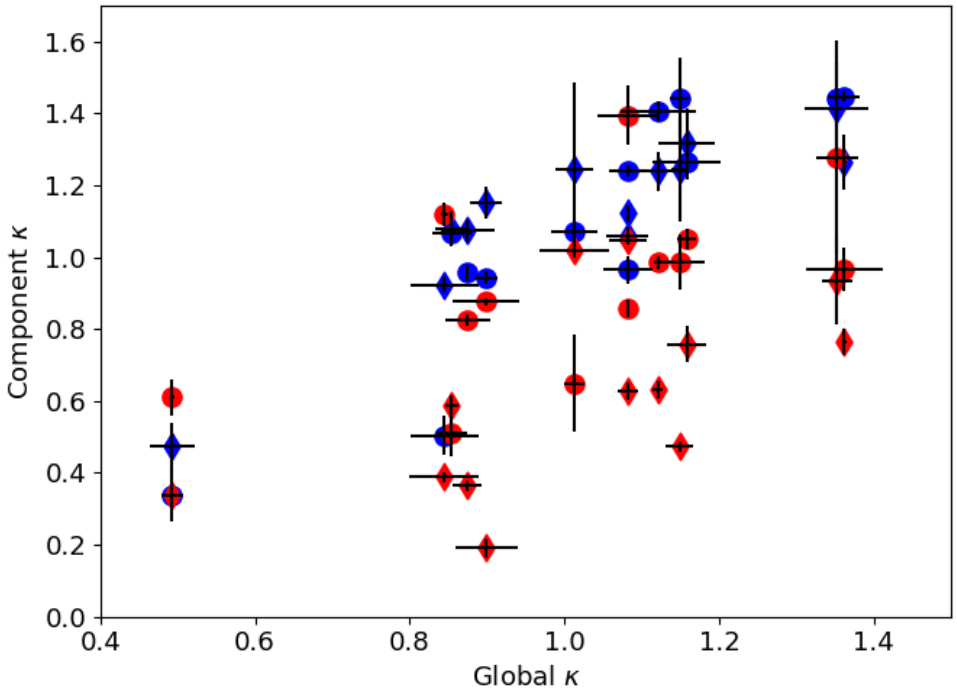


Figure 5.7: Bulge (red) and disk (blue) κ plotted against global galaxy κ. The spectroscopically decomposed components are marked with diamonds while the components obtained through JAM modelling of the global velocity field are marked with filled circles. The component values are clearly correlated with the global values, but with bulges offset to lower values of κ than disks.

One issue in the modelling process is that we do not take into account dark matter. In these central regions the effect should not be large, but potentially it could affect the outer disk–dominated region more than the inner bulge–dominated region, resulting in larger κ values for the disk than the bulge. Our sample includes galaxies from both the primary and the secondary MaNGA sample, covering on average out to $1.5R_{\rm e}$ and $2.5R_{\rm e}$ respectively (see Chapter 2, Section 2.3 for details). If dark matter were having an effect, we would expect there to be an offset in κ between the primary and secondary sample. However, we see no difference between these two samples and therefore conclude that dark matter is not significantly distorting the results.

JAM modelling is also not suitable for modelling slow-rotating galaxies. Since many of the bulges show significantly less rotation than the disks, the counter-rotation may be a result of the models failing to account for these less rotationally-supported systems. While this simple modelling approach is sufficient for a crude comparison, a more sophisticated dynamical model, or higher resolution data, would be required to really determine the underlying physics of these systems.

5.4 Addressing the distinctness of JAM components

Photometric decompositions and, more recently, spectroscopic decompositions have demonstrated the existence of multiple components within galaxies. An interesting question to address is whether this can be confirmed dynamically. It is not clear whether a two-component JAM model actually improves the fit to the data, or whether it introduces unnecessary complexity to a system sufficiently described using a single component model. As a way of testing this we compared the single-component and two-component models to the data. Since including additional degrees of freedom in a fit will inevitably lead to an improvement in chi-squared, determining when the inclusion of a second component corresponds to an actual physical component is not easy. As a criterion for the two-component model showing significant improvement compared to the single-component model, we determined whether the two-component model was closer to the data than it was to the single-component model, i.e. whether:

$$\sum^{nbins}(V_{\rm 2comp_model} - V_{\rm obs})^2 < \sum^{nbins}(V_{\rm 2comp_model} - V_{\rm 1comp_model})^2. \qquad (5.3)$$

If this is the case the improvement is most likely due to the two-component model more accurately describing the kinematics of the galaxy, rather than just the additional degrees of freedom allowing for small adjustments in the model.

Interestingly, none of the galaxies in our sample fulfill this criterion, therefore showing that including two components does not significantly improve the model fit, in turn implying that bulges and disks do not have very different anisotropies. However, due to the un-physical counter-rotating kinematics in several of the dynamical models, indicating that this simplistic model may not be sufficient in describing more complex systems, we feel that there is insufficient evidence at this point to conclude that bulges and disks are dynamically indistinct. On the contrary, while including two components does not lead to a statistically significant improvement in the model, the systematic difference in bulge and disk κ is a strong indication of an underlying difference in their properties; while for a single galaxy we cannot conclude that the bulge and disk are dynamically distinct, looking at a population of galaxies reveals systematic differences between the components unlikely to result from random scatter.

Dynamical models are complex and using good quality data to build the models, both

photometric and spectroscopic, is important. It may be that the spatial resolution of the NSA photometry, used for the photometric decomposition, and the MANGA data, used for the kinematics, is not sufficient to model such galaxies accurately. To explore whether this is the case we applied the same dynamical modeling technique to two MUSE observations of S0 galaxies. With very high spatial resolution, MUSE provides good quality photometry when the cube is collapsed in the wavelength direction, as well as excellent quality spectroscopic observations. While the spectral range of $4650 - 9300$Å is slightly less than MaNGA observations, MUSE provides higher spectral resolution of $\mathrm{R} = \lambda/\Delta\lambda = 2000$ at 4600Å and $\mathrm{R} = 4000$ at 9300Å, greater spatial coverage of 1×1 arcmin^2, and better spatial resolution with sampling of 0.2 arcseconds per pixel, which allows structure to be picked out in great detail. The observations were taken from a pilot project aimed at studying isolated and cluster lenticulars and were reduced using the MUSE pipeline (Weilbacher *et al.*, 2012).

Figure 5.8 shows the best-fitting JAM models for two MUSE observations of isolated lenticulars, selected for their clear presence of a photometric bulge and disk. The bulge components are best fit with $\kappa = 0.25$ and $\kappa = 0.82$ for the left and right-hand galaxies respectively, while the disks are best fit with $\kappa = 0.75$ and $\kappa = 1.12$. When using single component fits κ was found to be 0.4 and 0.89. Importantly, the two component models are both significantly closer to the data than the single component models, as is clearly visible in the residuals,and they both therefore fulfill the criterion presented in Equation 5.3. Of course only two galaxies, one of which is atypical in its positioning at the tail end of the distribution of κ, should not be used to infer the properties of all S0 galaxies, but it does indicate that, at least in some cases, bulges and disk are entirely dynamically distinct and their properties may be extracted.

This work illustrates the difficulties and degeneracies in building dynamical models for multiple components, but also hints at some interesting differences between the dynamics of bulges and disks. Applying such techniques on higher resolution data will likely provide valuable insights into the kinematic properties of the individual components.

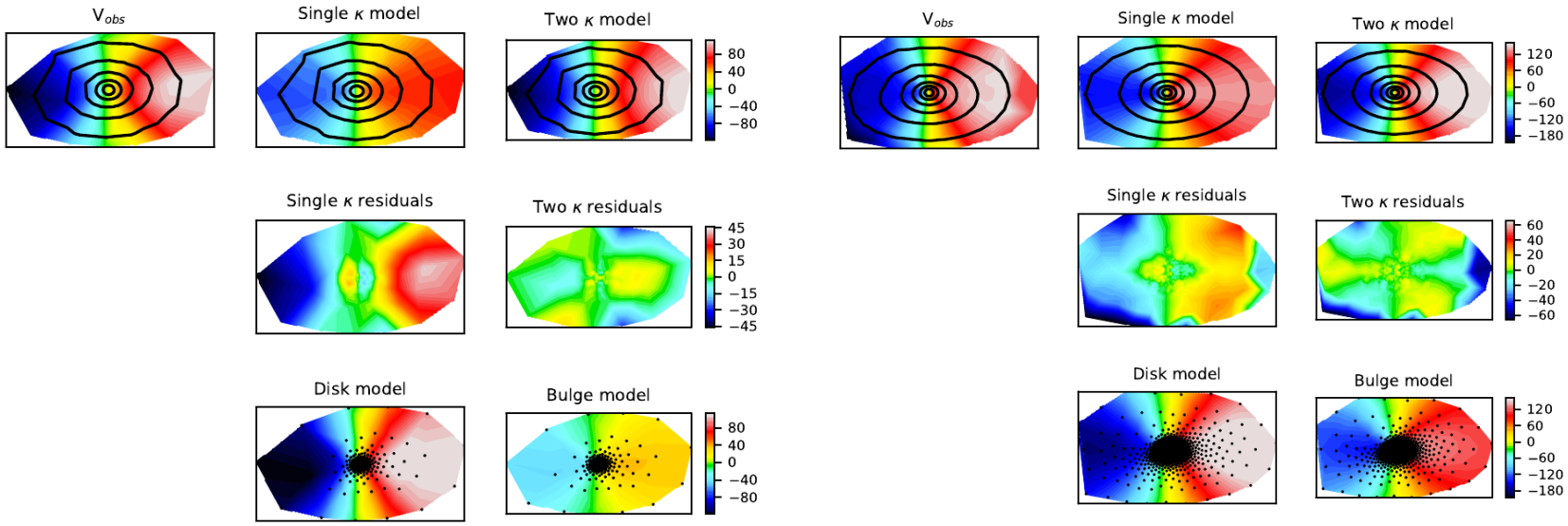


Figure 5.8: JAM models for two MUSE observations. For each galaxy, the top left shows the observed velocity field, top centre shows the JAM model using single κ and top right shows the JAM model using two different κ for bulge and disk. The centre row shows the residuals for each model, and the bottom row shows the models for the disk and bulge components.

5.5 Conclusions

By constructing dynamical models of a sub-sample of galaxies and allowing for different dynamical properties for the bulge and disk components we find:

- The dynamics of bulges and disks are best described by somewhat different values of κ, corresponding to different anisotropies. While disks show similar, or slightly higher, values of κ to those found for fast-rotator galaxies, bulges have slightly lower values.

- However, the improvement to the fit when two components are included in the models is not significant. While the systematic difference between the anisotropies of the components indicates that there is some intrinsic difference, the complexity of the models and the quality of the data used in this work are not sufficient to make a definitive statement about individual galaxies. Applications to higher spatial resolution MUSE observations indicate that bulges and disks are indeed dynamically distinct, and use of such high spatial resolution data, may be the key to understanding the properties of these components.

- The best-fit bulge and disk kinematic parameters from the dynamical models are reassuringly consistent with those obtained through spectroscopic decomposition, demonstrating that spectroscopic decomposition is effectively extracting the kinematics of the components.

Chapter 6

Discussion and further work

"We are all in the gutter, but some of us are looking at the stars."

– Oscar Wilde

6.1 Discussion

6.1.1 The existence of bulges and disks

Separating out galaxies into central and extended components has long been used as a way to explore their formation histories. However, whether these photometric components correspond to distinct stellar populations with separable kinematics, or whether they simply represent a convenient way to fit the light profile of galaxies, is not clear. In this thesis, we have developed a method to extract the kinematics and stellar populations of bulge and disk components, when their relative surface brightness is constrained to be the one provided by a previous photometric decomposition. An initial application of this technique to data cubes for three CALIFA S0 galaxies produces a remarkably coherent picture: these galaxies really can be separated into a cold rotating disk component and a hot rotating bulge component that match the expectations very well. Statistical comparisons for individual spectra show that fitting with two components is significantly better than only using a single component. Thus, the bulge

and the disk do seem to represent plausible distinct components, made of their own stellar populations with separable kinematics. With the distinctness of the components confirmed, we extended this analysis from whether they are different to *how* they are different.

6.1.2 Properties of bulges and disks

6.1.2.1 Kinematics

The spectroscopic decomposition method allows the extraction of bulge and disk velocity and velocity dispersion. This in turn allows calculation of kinematic parameters such as the stellar spin parameter, $\lambda_{\rm R}$, and the specific angular momentum, j_*, parameterisations of the kinematic information which make it possible to compare the kinematics of large samples of galaxies.

Where galaxies lie on the $\lambda_{\rm R} - \epsilon$ diagram is dictated by the intrinsic dynamical properties of the galaxy. However, the global values of λ_R tend not to correspond neatly to any particular simple dynamical model. This is unsurprising when you consider that these galaxies are made up of multiple components, the effect of which is clear when looking at how the position of a galaxy depends on its bulge-to-total ratio. To truly understand the kinematics of these galaxies we must therefore separate them into their constituent components. When we do this, we find that bulges and disks have very different λ_R parameters, with disks tending to be distributed towards higher angular momentum than bulges, which lie in, or close to, the slow rotator region.

However, while the global position of a galaxy on the $\lambda_{\rm R} - \epsilon$ diagram can tell us about its intrinsic dynamical properties, this is not formally true of the individual components in galaxies since they are not distinct systems but rather lie in the global potential of the galaxy. In addition, because bulges and disks cover different spatial ranges in the galaxy, a direct comparison of their properties is difficult. Comparing their values over the same radial range demonstrates that there is still a systematic difference in their properties, but calculating values over such a limited overlapping radial range is not representative of the true values of λ_R. In order to therefore determine the intrinsic dynamical properties of the components we perform full dynamical modelling of the

galaxies.

By combining the spectroscopic decomposition with dynamical modelling we can determine the kinematic anisotropies of bulge and disk, and therefore compare their dynamical structure. We find that while disks tend to have $\kappa \gtrsim 1$, bulges appear to have $\kappa \lesssim 1$, implying that there are systematic differences between bulges and disks. The improvement in including two components in the models, however, is not large, and we are therefore unable to say conclusively if bulges and disks have the same or different intrinsic dynamical properties. An initial application of the technique to high resolution MUSE observations indicates that, at least for some galaxies, bulges and disks are dynamically distinct. Wider application of dynamical modelling to high resolution data will hopefully lead to a more conclusive answer in the future.

This parameterisation of the kinematics of the components could prove very useful when compared across galaxy morphologies. For instance, similarities and differences between the bulges of star-forming versus quenched galaxies could be key in understanding whether the quenching occurred via internal secular processes, or external processes such as mergers. While it could be possible to result in similar anisotropies in the bulge and disk when both were formed via internal processes, it is unlikely for more disruptive processes such as mergers, which will effect the bulge and disk in very different ways, to give this result.

The projected angular momentum, j_p, of the components can also give insight into their history. When decomposed, each component follows a clear $M_* - j_p$ relation, which for the disks is the same relation as found for late-type disk galaxies, while the bulges sit on, or just below, the global values for slow-rotator elliptical galaxies. This demonstrates a remarkable consistency in these components across all morphologies, and is a persuasive indicator that not all slow-rotator galaxies can be classified as being fundamentally different from the more clearly disky lenticular galaxies, agreeing with observations previously made in regards to photometry (Krajnović *et al.*, 2013) and star-formation histories (Smethurst *et al.*, 2018). Combined with the coupling of the kinematics between components, this consistency also indicates that whatever the mechanism that leads to the transformation of these galaxies, it is one which evidently either retains the underlying kinematics of the individual components, or rebuilds the

components in a very similar manner.

Coupling of structural properties of the bulge and disk have been found in spiral galaxies (Courteau, deJong & Broeils, 1996; de Jong, 1995; MacArthur, Courteau & Holtzman, 2003; Carollo *et al.*, 2007), therefore this could be an indication of a passive quenching scenario, where gas has been stripped from a star-forming galaxy to form a disk-dominated early-type galaxy (Gunn & Gott, 1972; Crowl *et al.*, 2005; Rasmussen *et al.*, 2008; Abramson *et al.*, 2011). Whether such bulge-dominated galaxies as the ones studied here can be produced purely through the fading of spirals, however, is not yet clear, though several studies suggest it may be possible. Saha & Cortesi (2018) demonstrate that even an isolated disk can become unstable, resulting in the formation of stellar clumps which feed the growth of a bulge. Alternatively, the gradual accretion of material through minor mergers or gas accretion has been shown to be able to build up the bulge of a galaxy, making the disk stable against fragmentation and therefore ceasing star formation (Martig & Bournaud, 2009).

Simulations have also shown the potential for a disk to emerge from a major merger event (Springel & Hernquist, 2005; Barnes, 2002; Robertson *et al.*, 2006; Moster *et al.*, 2011; Hopkins *et al.*, 2009a). These merger remnants also display a similar structural coupling to the bulges and disks observed in S0s (Querejeta *et al.*, 2015b), as well as similar angular momentum and concentration (Querejeta *et al.*, 2015a). The dependence of the global $M_* - j_*$ relation on B/T ratio has now been replicated in several simulations, including Magneticum (Teklu *et al.*, 2015), Illustris (Genel *et al.*, 2015), Fenix (Pedrosa & Tissera, 2015) and EAGLE (Lagos *et al.*, 2018). Pedrosa & Tissera (2015) and Sokołowska *et al.* (2017) extract the angular momentum of bulges and disks in their simulations, and show that they follow parallel $M_* - j_*$ relations, as shown in Figure 6.1, very similar to those found in this work. They also find, intriguingly, that these relations do not evolve with reshift. These simulations indicate that the majority of galaxies begin their lives on a $M_* - j_*$ similar to present day disk galaxies, with angular momentum approximately equal to that of their halo. However, if a galaxy experiences certain processes such as AGN or a merger it will move off this relation down to regions of lower j_*. Precisely why the stellar populations that build a bulge should have such a similarly tight $M_* - j_*$ relation however is not yet clear.

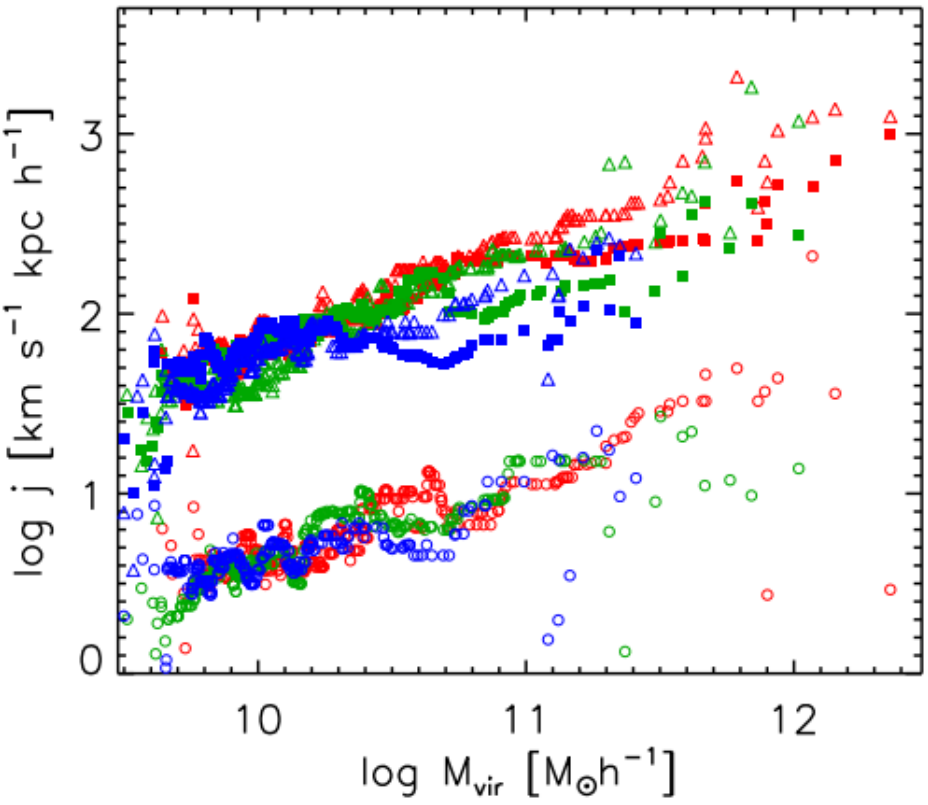


Figure 6.1: Specific stellar angular momentum for the stellar disc (empty triangles) and central spheroid (empty circles) components as a function of the virial mass for z = 0 (red), z = 1 (green) and, z = 2 (blue) in the GADGET-3 simulation. The gap between the two dynamical components does not evolve with redshift. For comparison purposes j for the the dark matter haloes have been also included (filled squares).

Adding further complication, it has also been found that mergers do not always reduce angular momentum. Lagos *et al.* (2018) examine the effect of mergers on the angular momentum of galaxies in the EAGLE simulation and find that j_* either increases or decreases depending on the mass ratio, gas richness and spin orientations of the merger event.

6.1.2.2 Stellar populations

The stellar populations of the components show that bulges and disks of these high mass galaxies in general have similar ages, but the bulges have systematically higher metallicities. For both age and metallicity, the disks show a wider range of values, reaching significantly lower metallicities and ages than the bulges. This is most likely because disks tend to have more varied star-formation histories, being more suscep-

tible to external processes such as gas accretion, suppression or removal (Smethurst *et al.*, 2015). The position of the bulge in the centre of the galactic potential well also allows metal-enriched gas to be retained, and higher metallicity stellar populations to be formed. This also explains the stronger mass-metallicity relation in the bulge compared to the disk.

Extracting the star-formation histories allows variations with mass to be picked out. While the higher mass ($\log(M) > 10.5$) galaxies tend to be uniformly old and metal-rich, the lower mass galaxies show a wider range of ages and metallicities, reaching down to populations as young as 2 Gyrs in the disk. These variations strongly indicate a mass-dependent difference in the evolution of these galaxies, with higher mass galaxies showing evidence of a rapid, early era of star-formation and little activity since, apart from some formation from more metal-poor gas in the disk. In contrast, while the lower-mass galaxies in our sample are for the most part also old and metal-rich, the spread of populations indicate that star-formation happened over a longer time period, and was not as effectively curtailed as for high mass galaxies, with star formation continuing in both components up until a few gigayears ago.

The great advantage of this method of spectroscopic decomposition is in the extraction of both the kinematics and the stellar populations, which when combined provide a detailed view into the evolution of a galaxy. What is intriguing about the outcome of this synthesis is that there appears to be little clear correlation between the stellar composition of the components and their kinematics. In particular, where a component lies on the $M_* - j_*$ plane does not depend on the age of that component, or the relative ages of the components. While there is a dependence of metallicity on angular momentum, it is much stronger for, and therefore likely determined by, the stellar mass. While the different components are therefore clearly dynamically distinct, their stellar populations are often quite similar. However, the range in ages in the sample is small, being all early-type galaxies and therefore not including young discs, and discriminating between populations which are uniformly old is not easy. Extending this work to include star-forming galaxies may be the key to truly understanding exactly where and when star formation is switched off, and what effect, if any, this process has on the kinematics of the components.

6.2 Further work

The method of spectroscopic decomposition, when applied to a wide range of galaxy morphologies, has the potential to provide some novel insight into the internal properties of galaxies. A deeper understanding of the kinematics of bulges and disks, and to what extent they are linked, will be key in understanding the formation mechanisms responsible for the galaxies we see in the local universe. Some key questions to address in the future are outlined below.

6.2.1 Spectroscopic decomposition of spiral galaxies

As well as being an interesting class of galaxies to try to understand, early-type galaxies make an excellent class for testing such a bulge-disk decomposition method on due to their relatively simple structure, for the most part lacking spiral arms, rings, large amounts of dust etc., all of which complicate the decomposition process. However, to truly understand how galaxies form and evolve we will need to understand how the bulges and disks of spiral galaxies compare to those of the early-type galaxies explored in this work. In particular, whether they lie on the same kinematic relations, such as the $M_* - j_*$ relation, as early-type galaxies, and whether, in extending this analysis to a wider range of ages and metallicities, we begin to see any correlations between the kinematics and stellar populations of the components which could provide a key to understanding which processes are dominating in their evolution.

If the spiral structure is sufficiently faint it will in fact have very little effect on the bulge and disk components, allowing them to be decomposed in a similar way to early-type galaxies. Figure 6.2 shows an example of this, with the spectroscopic decomposition method developed in this thesis applied to a spiral galaxy in the MaNGA survey. However, for the majority of spiral galaxies the arms are too bright, and indeed are too interesting, to simply be disregarded. Accounting for these more complex structures during the decomposition process is not an easy task. Including additional components in the decomposition only increases the degeneracy of the fit, making it increasingly hard to disentangle the LOSVD of the various components. It also requires accurate photometric decompositions including spiral structure, which, while possible with

software such as GALFIT, has so far proven difficult to implement successfully. A potential way to get around this issue would be to mask out spiral structure, either for the whole decomposition process, allowing the bulge and disk to be decomposed as if the spiral arms did not exist, or only for the photometric decomposition, allowing the flux fraction of the spiral arms to be determined as the residual once the bulge and disk had been subtracted off, and therefore allowing all three components to be spectroscopically decomposed. Masking out the arms requires knowing where they are, information which could be obtained using Galaxy Zoo 3D, where members of the public are asked to identify galaxy regions dominated by spiral arms and bars. How accurate these masks are, however, is not yet certain; spiral arms, particularly in the more diffuse cases, are not always easy to identify.

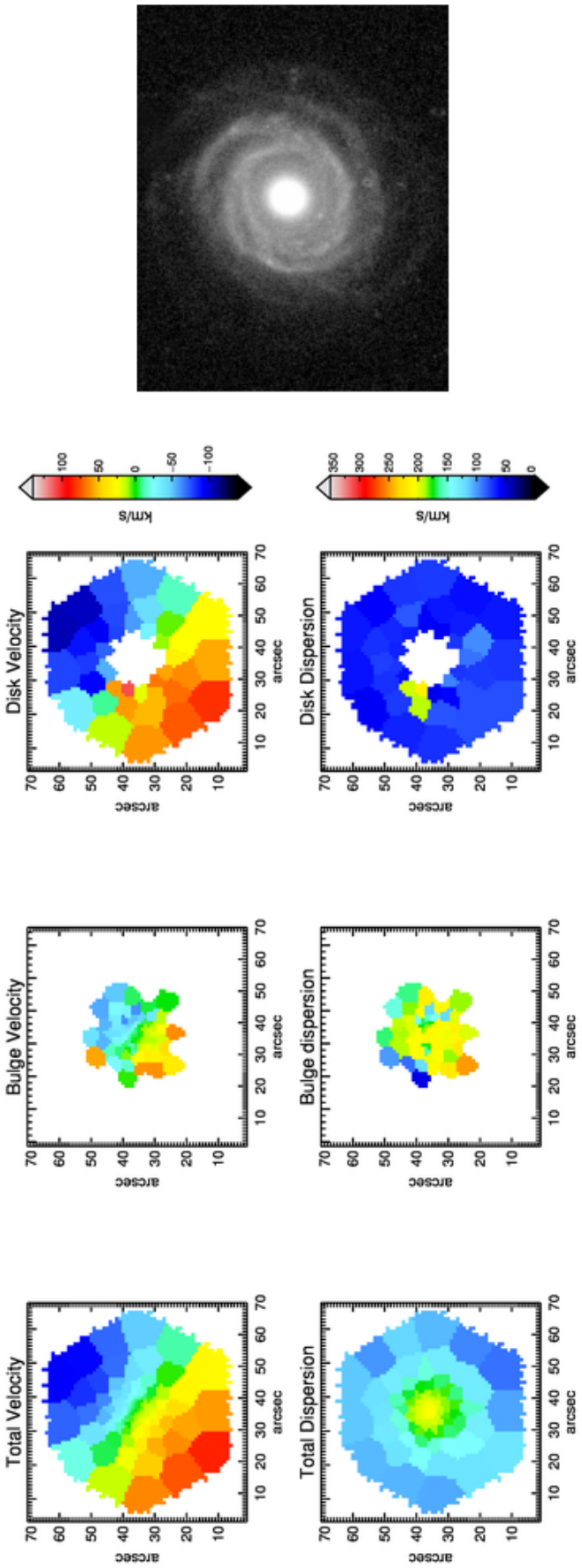


Figure 6.2: Spectroscopic decomposition of a MaNGA spiral galaxy

6.2.2 Extending spectroscopic decomposition to lower masses

The star-formation histories of the components found in this work, as well as other studies extending to lower masses such as Fraser-McKelvie *et al.* (2018), show that lower mass galaxies tend to have different distributions of stellar populations compared to high mass systems, indicating a potential difference in evolutionary path. Currently, due to the high S/N necessary for the spectroscopic decomposition, this analysis is limited to fairly high mass galaxies. Finding a way to extend this work to lower masses will allow us to combine kinematic information with stellar populations and could help us understand the different formation paths responsible for the differences in stellar populations. However, this will require either higher quality data than currently available in large IFU surveys such as MaNGA in order to obtain sufficient signal-to-noise and spatial resolution for lower mass galaxies, or alterations to the method in order to constrain the fit when extended to lower signal-to-noise. A key to this would be in obtaining a good quality template bulge and disk spectrum to use in the two component fit to the kinematics.

6.2.3 Dynamical modelling

With the current quality of data and dynamical models, dynamical modelling when accounting for two components appears to contain too many degeneracies to be able to determine definitively whether bulges and disks have truly distinct dynamical properties. To attempt to address this we demonstrated in Chapter 5 that when dynamical modelling methods are applied to higher resolution data such as MUSE, subtle spatial variations in the kinematics can be picked out, therefore allowing differences between the components to be extracted. By applying the modelling to two S0 galaxies, we found that bulges and disks appear to have different anisotropies, and allowing for these differences in the models produces a significantly better fit than when only allowing for a single anisotropy.

Determining whether or not bulges and disks have the same anisotropy and, if they do, whether this holds across all morphologies, would have important implications on the evolutionary processes responsible for producing such galaxies. This initial

application indicates that applying dynamical modelling on a large sample of data with high spectroscopic and spatial resolution could provide us with the methodology to understand these differences.

6.2.4 The bulge-disk decomposition method to end all bulge-disk decomposition methods

The method presented in this thesis often works by fitting for selected parameters, then holding these fixed in subsequent fits, for example, by obtaining photometric parameters through a photometric decomposition, then fixing these when fitting to the kinematics. While this helps to constrain the fits, it does not make the best use of the data. A more rigorous, but by no means trivial, approach, would be to combine the information available from various decomposition methods into one "super-decomposition" method. Incorporating information from photometric decompositions, spectroscopic decompositions and dynamical models to simultaneously fit for photometric, kinematic, and stellar population parameters would optimise the use of all information available, allowing the best fitting parameters to be extracted in a statistically meaningful way. With the value in performing spectroscopic bulge-disk decomposition methods becoming increasingly apparent, it is likely that such a method will be developed in the not-too-distant future.

We hope that the work undertaken in this thesis provides a good starting point for spectroscopic bulge-disk decomposition methods, and demonstrates the value in separating out components spectroscopically. We believe that with the increasing number and quality of IFU observations, such methods as these will be invaluable in understanding the sometimes subtle differences in how galaxies have formed and evolved, and the role that individual components play over the lifetime of a galaxy.

Bibliography

Abazajian K. N., Adelman-McCarthy J. K., Agüeros M. A., Allam S. S., Allende Prieto C., An D., Anderson K. S. J., Anderson S. F., Annis J., Bahcall N. A., et al., 2009. ApJS, **182**, 543.

Abramson A., Kenney J. D. P., Crowl H. H., Chung A., van Gorkom J. H., Vollmer B., Schiminovich D., 2011. AJ, **141**, 164.

Andredakis Y. C., Sanders R., 1994. MNRAS, **267**, 283.

Andredakis Y. C., Peletier R. F., Balcells M., 1995. *MNRAS*, **275**, 874.

Baldry I. K., Balogh M. L., Bower R. G., Glazebrook K., Nichol R. C., Bamford S. P., Budavari T., 2006. MNRAS, **373**, 469.

Balogh M. L., Morris S. L., Yee H. K. C., Carlberg R. G., Ellingson E., 1999. ApJ, **527**, 54.

Balogh M. L., Baldry I. K., Nichol R., Miller C., Bower R., Glazebrook K., 2004. ApJ, **615**, L101.

Balogh M. L., Navarro J. F., Morris S. L., 2000. ApJ, **540**, 113.

Bamford S. P., Nichol R. C., Baldry I. K., Land K., Lintott C. J., Schawinski K., Slosar A., Szalay A. S., Thomas D., Torki M., Andreescu D., Edmondson E. M., Miller C. J., Murray P., Raddick M. J., Vandenberg J., 2009. MNRAS, **393**, 1324.

Barnes J. E., 2002. MNRAS, **333**, 481.

Bedregal A. G., Cardiel N., Aragón-Salamanca A., Merrifield M. R., 2011. *MNRAS*, **415(3)**, 2063.

Bell E. F., de Jong R. S., 2000. *MNRAS*, **312(3)**, 497.

Bender R., 1990. *A&A*, **229**, 441.

Bernardi M., Sheth R. K., Annis J., Burles S., Eisenstein D. J., Finkbeiner D. P., Hogg D. W., Lupton R. H., Schlegel D. J., SubbaRao M., Bahcall N. A., Blakeslee J. P., Brinkmann J., Castander F. J., Connolly A. J., Csabai I., Doi M., Fukugita M., Frieman J., Heckman T., Hennessy G. S., Ivezić Ž., Knapp G. R., Lamb D. Q., McKay T., Munn J. A., Nichol R., Okamura S., Schneider D. P., Thakar A. R., York D. G., 2003. AJ, **125**, 1866.

Bershady M. A., Verheijen M. A. W., Swaters R. A., Andersen D. R., Westfall K. B., Martinsson T., 2010. ApJ, **716**, 198.

Blanc G. A., Weinzirl T., Song M., Heiderman A., Gebhardt K., Jogee S., Evans, II N. J., van den Bosch R. C. E., Luo R., Drory N., Fabricius M., Fisher D., Hao L., Kaplan K., Marinova I., Vutisalchavakul N., Yoachim P., 2013. AJ, **145**, 138.

Blanton M. R., Hogg D. W., Bahcall N. A., Baldry I. K., Brinkmann J., Csabai I., Eisenstein D., Fukugita M., Gunn J. E., Ivezić Ž., Lamb D. Q., Lupton R. H., Loveday J., Munn J. A., Nichol R. C., Okamura S., Schlegel D. J., Shimasaku K., Strauss M. A., Vogeley M. S., Weinberg D. H., 2003. ApJ, **594**, 186.

Blanton M. R., Eisenstein D., Hogg D. W., Schlegel D. J., Brinkmann J., 2005. ApJ, **629**, 143.

Blanton M. R., Kazin E., Muna D., Weaver B. A., Price-Whelan A., 2011. AJ, **142**, 31.

Blanton M. R., Bershady M. A., Abolfathi B., Albareti F. D., Allende Prieto C., Almeida A., Alonso-García J., Anders F., Anderson S. F., Andrews B., et al., 2017. AJ, **154**, 28.

Bothun G. D., Gregg M. D., 1990. *ApJ*, **350**, 73.

Bournaud F., Jog C. J., Combes F., 2005. A&A, **437**, 69.

Brinchmann J., Charlot S., White S. D. M., Tremonti C., Kauffmann G., Heckman T., Brinkmann J., 2004. MNRAS, **351**, 1151.

Brough S., van de Sande J., Owers M. S., d'Eugenio F., Sharp R., Cortese L., Scott N., Croom S. M., Bassett R., Bekki K., Bland-Hawthorn J., Bryant J. J., Davies R., Drinkwater M. J., Driver S. P., Foster C., Goldstein G., López-Sánchez Á. R., Medling A. M., Sweet S. M., Taranu D. S., Tonini C., Yi S. K., Goodwin M., Lawrence J. S., Richards S. N., 2017. ApJ, **844**, 59.

Bryant J. J., Owers M. S., Robotham A. S. G., Croom S. M., Driver S. P., Drinkwater M. J., Lorente N. P. F., Cortese L., Scott N., Colless M., Schaefer A., Taylor E. N., Konstantopoulos I. S., Allen J. T., Baldry I., Barnes L., Bauer A. E., Bland-Hawthorn J., Bloom J. V., Brooks A. M., Brough S., Cecil G., Couch W., Croton D., Davies R., Ellis S., Fogarty L. M. R., Foster C., Glazebrook K., Goodwin M., Green A., Gunawardhana M. L., Hampton E., Ho I.-T., Hopkins A. M., Kewley L., Lawrence J. S., Leon-Saval S. G., Leslie S., McElroy R., Lewis G., Liske J., López-Sánchez Á. R., Mahajan S., Medling A. M., Metcalfe N., Meyer M., Mould J., Obreschkow D., O'Toole S., Pracy M., Richards S. N., Shanks T., Sharp R., Sweet S. M., Thomas A. D., Tonini C., Walcher C. J., 2015. MNRAS, **447**, 2857.

Bundy K., Bershady M. A., Law D. R., Yan R., Drory N., MacDonald N., Wake D. A., Cherinka B., Sánchez-Gallego J. R., Weijmans A.-M., Thomas D., Tremonti C., Masters K., Coccato L., Diamond-Stanic A. M., Aragón-Salamanca A., Avila-Reese V., Badenes C., Falcón-Barroso J., Belfiore F., Bizyaev D., Blanc G. A., Bland-Hawthorn J., Blanton M. R., Brownstein J. R., Byler N., Cappellari M., Conroy C., Dutton A. A., Emsellem E., Etherington J., Frinchaboy P. M., Fu H., Gunn J. E.,

Harding P., Johnston E. J., Kauffmann G., Kinemuchi K., Klaene M. A., Knapen J. H., Leauthaud A., Li C., Lin L., Maiolino R., Malanushenko V., Malanushenko E., Mao S., Maraston C., McDermid R. M., Merrifield M. R., Nichol R. C., Oravetz D., Pan K., Parejko J. K., Sanchez S. F., Schlegel D., Simmons A., Steele O., Steinmetz M., Thanjavur K., Thompson B. A., Tinker J. L., van den Bosch R. C. E., Westfall K. B., Wilkinson D., Wright S., Xiao T., Zhang K., 2015. *ApJ*, **798(1)**, 7.

Bureau M., Freeman K. C., 1999. *AJ*, **118(1)**, 126.

Caldwell N., 1983. *ApJ*, **268**, 90.

Cano-Díaz M., Sánchez S. F., Zibetti S., Ascasibar Y., Bland-Hawthorn J., Ziegler B., González Delgado R. M., Walcher C. J., García-Benito R., Mast D., Mendoza-Pérez M. A., Falcón-Barroso J., Galbany L., Husemann B., Kehrig C., Marino R. A., Sánchez-Blázquez P., López-Cobá C., López-Sánchez Á. R., Vilchez J. M., 2016. ApJ, **821**, L26.

Cappellari M., Copin Y., 2003. MNRAS, **342(2)**, 345.

Cappellari M., Emsellem E., 2004. *Publications of the Astronomical Society of the Pacific*, **116(816)**, 138.

Cappellari M., Emsellem E., Bacon R., Bureau M., Davies R. L., de Zeeuw P. T., Falcón-Barroso J., Krajnović D., Kuntschner H., McDermid R. M., Peletier R. F., Sarzi M., van den Bosch R. C. E., van de Ven G., 2007. MNRAS, **379**, 418.

Cappellari M., Emsellem E., Krajnović D., McDermid R. M., Scott N., Verdoes Kleijn G. A., Young L. M., Alatalo K., Bacon R., Blitz L., Bois M., Bournaud F., Bureau M., Davies R. L., Davis T. A., de Zeeuw P. T., Duc P.-A., Khochfar S., Kuntschner H., Lablanche P.-Y., Morganti R., Naab T., Oosterloo T., Sarzi M., Serra P., Weijmans A.-M., 2011. *MNRAS*, **413(2)**, 813.

Cappellari M., 2002. MNRAS, **333**, 400.

Cappellari M., 2008. MNRAS, **390**, 71.

Cappellari M., 2013. *ApJ*, **778**, L2.

Cappellari M., 2016. *ArXiv e-prints*.

Carollo C. M., Scarlata C., Stiavelli M., Wyse R. F. G., Mayer L., 2007. ApJ, **658**, 960.

Carollo C., 1998. *ApJ*, **523**, 566.

Chamberlain L. C. P., Courteau S., McDonald M., Rose J. A., 2011. *MNRAS*, **412(1)**, 423.

Coccato L., Fabricius M., Morelli L., Corsini E. M., Pizzella A., Erwin P., Dalla Bontà E., Saglia R., Bender R., Williams M., 2015. A&A, **581**, A65.

Cortese L., Fogarty L. M. R., Bekki K., van de Sande J., Couch W., Catinella B., Colless M., Obreschkow D., Taranu D., Tescari E., Barat D., Bland-Hawthorn J., Bloom J., Bryant J. J., Cluver M., Croom S. M., Drinkwater M. J., d'Eugenio F., Konstantopoulos I. S., Lopez-Sanchez A., Mahajan S., Scott N., Tonini C., Wong O. I., Allen J. T., Brough S., Goodwin M., Green A. W., Ho I.-T., Kelvin L. S., Lawrence J. S., Lorente N. P. F., Medling A. M., Owers M. S., Richards S., Sharp R., Sweet S. M., 2016. MNRAS, **463**, 170.

Courteau S., de Jong R. S., Broeils A. H., 1996. *ApJ*, **457(2)**.

Crowl H. H., Kenney J. D. P., van Gorkom J. H., Vollmer B., 2005. AJ, **130**, 65.

de Jong R., 1995. *A&A*, **118**, 557.

de Souza R. E., Gadotti D. A., dos Anjos S., 2004. ApJS, **153**, 411.

de Vaucouleurs G., 1948. *Annales d'Astrophysique*, **11**.

de Zeeuw P. T., Bureau M., Emsellem E., Bacon R., Carollo C. M., Copin Y., Davies R. L., Kuntschner H., Miller B. W., Monnet G., Peletier R. F., Verolme E. K., 2002. MNRAS, **329**, 513.

Dressler A., 1980. ApJ, **236**, 351.

Driver S. P., Liske J., Cross N. J. G., De Propris R., Allen P. D., 2005. MNRAS, **360**, 81.

Driver S. P., Allen P. D., Graham A. W., Cameron E., Liske J., Ellis S. C., Cross N. J. G., De Propris R., Phillipps S., Couch W. J., 2006. MNRAS, **368**, 414.

Efstathiou G., 2000. MNRAS, **317**, 697.

Eggen O. J., Lynden-Bell D., Sandage A. R., 1962. ApJ, **136**, 748.

Emsellem E., Cappellari M., Krajnović D., van de Ven G., Bacon R., Bureau M., Davies R. L., de Zeeuw P. T., Falcón-Barroso J., Kuntschner H., McDermid R., Peletier R. F., Sarzi M., 2007. MNRAS, **379**, 401.

Emsellem E., Monnet G., Bacon R., 1994. A&A, **285**, 723.

Fabian A. C., 2012. ARA&A, **50**, 455.

Fabricius M. H., Saglia R. P., Fisher D. B., Drory N., Bender R., Hopp U., 2012. *ApJ*, **754(1)**, 67.

Falcón-Barroso J., Balcells M., Peletier R. F., Vazdekis A., 2003. A&A, **405**, 455.

Fall S. M., Efstathiou G., 1980. *MNRAS*, **193**, 189.

Fall S. M., Romanowsky A. J., 2018. *ArXiv e-prints*.

Fall S. M., 1983. In: *Internal Kinematics and Dynamics of Galaxies*, p. 391, ed. Athanassoula E.

Fang J. J., Faber S. M., Koo D. C., Dekel A., 2013. ApJ, **776**, 63.

Fisher D., Franx M., Illingworth G., 1996. *ApJ*, **459**, 110.

Fraser-McKelvie A., Aragón-Salamanca A., Merrifield M., Tabor M., Bernardi M., Drory N., Parikh T., Argudo-Fernández M., 2018. MNRAS.

Freeman K. C., 1970. *ApJ*, **160**, 811.

García-Benito R., Zibetti S., Sánchez S. F., Husemann B., de Amorim A. L., Castillo-Morales A., Cid Fernandes R., Ellis S. C., Falcón-Barroso J., Galbany L., Gil de Paz A., González Delgado R. M., Lacerda E. A. D., López-Fernandez R., de Lorenzo-Cáceres A., Lyubenova M., Marino R. A., Mast D., Mendoza M. A., Pérez E., Vale Asari N., Aguerri J. A. L., Ascasibar Y., Bekerait*error*ė S., Bland-Hawthorn J., Barrera-Ballesteros J. K., Bomans D. J., Cano-Díaz M., Catalán-Torrecilla C., Cortijo C., Delgado-Inglada G., Demleitner M., Dettmar R.-J., Díaz A. I., Florido E., Gallazzi A., García-Lorenzo B., Gomes J. M., Holmes L., Iglesias-Páramo J., Jahnke K., Kalinova V., Kehrig C., Kennicutt R. C., López-Sánchez Á. R., Márquez I., Masegosa J., Meidt S. E., Mendez-Abreu J., Mollá M., Monreal-Ibero A., Morisset C., del Olmo A., Papaderos P., Pérez I., Quirrenbach A., Rosales-Ortega F. F., Roth M. M., Ruiz-Lara T., Sánchez-Blázquez P., Sánchez-Menguiano L., Singh R., Spekkens K., Stanishev V., Torres-Papaqui J. P., van de Ven G., Vilchez J. M., Walcher C. J., Wild V., Wisotzki L., Ziegler B., Alves J., Barrado D., Quintana J. M., Aceituno J., 2015. *A&A*, **576**, A135.

Genel S., Fall S. M., Hernquist L., Vogelsberger M., Snyder G. F., Rodriguez-Gomez V., Sijacki D., Springel V., 2015. ApJ, **804**, L40.

Gerssen J., Shapiro Griffin K., 2012. MNRAS, **423**, 2726.

Gerssen J., Kuijken K., Merrifield M. R., 1997. MNRAS, **288**, 618.

Goddard D., Thomas D., Maraston C., Westfall K., Etherington J., Riffel R., Mallmann N. D., Zheng Z., Argudo-Fernández M., Lian J., Bershady M., Bundy K., Drory N., Law D., Yan R., Wake D., Weijmans A., Bizyaev D., Brownstein J., Lane R. R., Maiolino R., Masters K., Merrifield M., Nitschelm C., Pan K., Roman-Lopes A., Storchi-Bergmann T., Schneider D. P., 2017. MNRAS, **466**, 4731.

González Delgado R. M., Cid Fernandes R., García-Benito R., Pérez E., de Amorim A. L., Cortijo-Ferrero C., Lacerda E. A. D., López Fernández R., Sánchez S. F., Vale Asari N., Alves J., Bland-Hawthorn J., Galbany L., Gallazzi A., Husemann B., Bekeraite S., Jungwiert B., López-Sánchez A. R., de Lorenzo-Cáceres A., Marino R. A., Mast D., Mollá M., del Olmo A., Sánchez-Blázquez P., van de Ven G., Vílchez J. M., Walcher C. J., Wisotzki L., Ziegler B., Collaboration920 C., 2014. ApJ, **791**, L16.

González Delgado R. M., Cid Fernandes R., Pérez E., García-Benito R., López Fernández R., Lacerda E. A. D., Cortijo-Ferrero C., de Amorim A. L., Vale Asari N., Sánchez S. F., Walcher C. J., Wisotzki L., Mast D., Alves J., Ascasibar Y., Bland-Hawthorn J., Galbany L., Kennicutt R. C., Márquez I., Masegosa J., Mollá M., Sánchez-Blázquez P., Vílchez J. M., 2016. A&A, **590**, A44.

González Delgado R. M., Pérez E., Cid Fernandes R., García-Benito R., López Fernández R., Vale Asari N., Cortijo-Ferrero C., de Amorim A. L., Lacerda E. A. D., Sánchez S. F., Lehnert M. D., Walcher C. J., 2017. A&A, **607**, A128.

Graham M. T., Cappellari M., Li H., Mao S., Bershady M. A., Bizyaev D., Brinkmann J., Brownstein J. R., Bundy K., Drory N., Law D. R., Pan K., Thomas D., Wake D. A., Weijmans A.-M., Westfall K. B., Yan R., 2018. MNRAS, **477**, 4711.

Greene J. E., Leauthaud A., Emsellem E., Goddard D., Ge J., Andrews B. H., Brinkman J., Brownstein J. R., Greco J., Law D., Lin Y.-T., Masters K. L., Merrifield M., More S., Okabe N., Schneider D. P., Thomas D., Wake D. A., Yan R., Drory N., 2017. ApJ, **851**, L33.

Gunn J. E., Gott, III J. R., 1972. ApJ, **176**, 1.

Gunn J. E., Siegmund W. A., Mannery E. J., Owen R. E., Hull C. L., Leger R. F., Carey L. N., Knapp G. R., York D. G., Boroski W. N., Kent S. M., Lupton R. H., Rockosi C. M., Evans M. L., Waddell P., Anderson J. E., Annis J., Barentine J. C., Bartoszek L. M., Bastian S., Bracker S. B., Brewington H. J., Briegel C. I., Brinkmann J., Brown Y. J., Carr M. A., Czarapata P. C., Drennan C. C., Dombeck T., Federwitz G. R., Gillespie B. A., Gonzales C., Hansen S. U., Harvanek M., Hayes J., Jordan W., Kinney E., Klaene M., Kleinman S. J., Kron R. G., Kresinski J., Lee G., Limmongkol S., Lindenmeyer C. W., Long D. C., Loomis C. L., McGehee P. M., Mantsch P. M., Neilsen, Jr. E. H., Neswold R. M., Newman P. R., Nitta A., Peoples, Jr. J., Pier J. R., Prieto P. S., Prosapio A., Rivetta C., Schneider D. P., Snedden S., Wang S.-i., 2006. AJ, **131**, 2332.

Hart R. E., Bamford S. P., Willett K. W., Masters K. L., Cardamone C., Lintott C. J., Mackay R. J., Nichol R. C., Rosslowe C. K., Simmons B. D., Smethurst R. J., 2016. MNRAS, **461**, 3663.

Häußler B., Bamford S. P., Vika M., Rojas A. L., Barden M., Kelvin L. S., Alpaslan M., Robotham A. S. G., Driver S. P., Baldry I. K., Brough S., Hopkins A. M., Liske J., Nichol R. C., Popescu C. C., Tuffs R. J., 2013. *MNRAS*, **430**, 330.

Hogg D. W., Blanton M. R., Eisenstein D. J., Gunn J. E., Schlegel D. J., Zehavi I., Bahcall N. A., Brinkmann J., Csabai I., Schneider D. P., Weinberg D. H., York D. G., 2003. ApJ, **585**, L5.

Hopkins P. F., Cox T. J., Younger J. D., Hernquist L., 2009a. ApJ, **691**, 1168.

Hopkins P. F., Somerville R. S., Cox T. J., Hernquist L., Jogee S., Kereš D., Ma C.-P., Robertson B., Stewart K., 2009b. MNRAS, **397**, 802.

Hopkins P. F., Quataert E., Murray N., 2012. MNRAS, **421**, 3522.

Hubble E. P., 1926. ApJ, **64**.

Jeans J. H., 1922. MNRAS, **82**, 122.

Johansson J., Thomas D., Maraston C., 2012. MNRAS, **421**, 1908.

Johnston E. J., Aragón-Salamanca A., Merrifield M. R., 2014. *MNRAS*, **441**, 333.

Johnston E. J., Aragón-Salamanca A., Merrifield M. R., Bedregal A. G., 2012. *MNRAS*, **422(February)**, 2590.

Johnston E. J., Aragón-Salamanca A., Merrifield M. R., Bedregal A. G., 2014. In: *Structure and Dynamics of Disk Galaxies*, 161, eds Seigar M. S., Treuthardt P.

Johnston E. J., Häußler B., Aragón-Salamanca A., Merrifield M. R., Bamford S., Bershady M. A., Bundy K., Drory N., Fu H., Law D., Nitschelm C., Thomas D., Roman Lopes A., Wake D., Yan R., 2017. MNRAS, **465**, 2317.

Johnston E. J., Merrifield M., Aragón-Salamanca A., 2018. MNRAS, **478**, 4255.

Kauffmann G., Heckman T. M., White S. D. M., Charlot S., Tremonti C., Brinchmann J., Bruzual G., Peng E. W., Seibert M., Bernardi M., Blanton M., Brinkmann J., Castander F., Csábai I., Fukugita M., Ivezic Z., Munn J. A., Nichol R. C., Padmanabhan N., Thakar A. R., Weinberg D. H., York D., 2003. MNRAS, **341**, 33.

Kereš D., Katz N., Weinberg D. H., Davé R., 2005. MNRAS, **363**, 2.

Kormendy J., Kennicutt R. C., 2004. *ARA&A*, **42(1)**, 603.

Kormendy J., 1977. ApJ, **217**, 406.

Krajnović D., Alatalo K., Blitz L., Bois M., Bournaud F., Bureau M., Cappellari M., Davies R. L., Davis T. A., de Zeeuw P. T., Duc P.-A., Emsellem E., Khochfar S., Kuntschner H., McDermid R. M., Morganti R., Naab T., Oosterloo T., Sarzi M., Scott N., Serra P., Weijmans A.-M., Young L. M., 2013. MNRAS, **432**, 1768.

Kuijken K., Merrifield M. R., 1995. *ApJ*, **443**, L13.

Kuntschner H., 2000. *MNRAS*, **315(1)**, 184.

Lagos C. d. P., Stevens A. R. H., Bower R. G., Davis T. A., Contreras S., Padilla N. D., Obreschkow D., Croton D., Trayford J. W., Welker C., Theuns T., 2018. MNRAS, **473**, 4956.

Larson R. B., 1974. MNRAS, **166**, 585.

Laurikainen E., Salo H., Buta R., Knapen J. H., Comerón S., 2010. MNRAS, **405**, 1089.

Law D. R., Yan R., Bershady M. A., Bundy K., Cherinka B., Drory N., MacDonald N., Sánchez-Gallego J. R., Wake D. A., Weijmans A.-M., Blanton M. R., Klaene M. A., Moran S. M., Sanchez S. F., Zhang K., 2015. AJ, **150**, 19.

Law D. R., Cherinka B., Yan R., Andrews B. H., Bershady M. A., Bizyaev D., Blanc G. A., Blanton M. R., Bolton A. S., Brownstein J. R., Bundy K., Chen Y., Drory N., D'Souza R., Fu H., Jones A., Kauffmann G., MacDonald N., Masters K. L., Newman J. A., Parejko J. K., Sánchez-Gallego J. R., Sánchez S. F., Schlegel D. J., Thomas D., Wake D. A., Weijmans A.-M., Westfall K. B., Zhang K., 2016. AJ, **152**, 83.

Lawson C., Hanson R., 1995. *Solving Least Squares Problems*, Society for Industrial and Applied Mathematics.

Lewis I. J., Cannon R. D., Taylor K., Glazebrook K., Bailey J. A., Baldry I. K., Barton J. R., Bridges T. J., Dalton G. B., Farrell T. J., Gray P. M., Lankshear A., McCowage C., Parry I. R., Sharples R. M., Shortridge K., Smith G. A., Stevenson J., Straede J. O., Waller L. G., Whittard J. D., Wilcox J. K., Willis K. C., 2002. MNRAS, **333**, 279.

Li S.-l., Shi Y., Chen Y.-M., Tabor M., Bizyaev D., Chen J.-h., Yu X.-l., Bing L.-j., 2018. MNRAS, **480**, 1705.

Lilly S. J., Le Fèvre O., Renzini A., Zamorani G., Scodeggio M., Contini T., Carollo C. M., Hasinger G., Kneib J.-P., Iovino A., Le Brun V., Maier C., Mainieri V., Mignoli M., Silverman J., Tasca L. A. M., Bolzonella M., Bongiorno A., Bottini D., Capak P., Caputi K., Cimatti A., Cucciati O., Daddi E., Feldmann R., Franzetti P., Garilli B., Guzzo L., Ilbert O., Kampczyk P., Kovac K., Lamareille F., Leauthaud A., Le Borgne J.-F., McCracken H. J., Marinoni C., Pello R., Ricciardelli E., Scarlata C., Vergani D., Sanders D. B., Schinnerer E., Scoville N., Taniguchi Y., Arnouts S., Aussel H., Bardelli S., Brusa M., Cappi A., Ciliegi P., Finoguenov A., Foucaud S., Franceschini A., Halliday C., Impey C., Knobel C., Koekemoer A., Kurk J., Maccagni D., Maddox S., Marano B., Marconi G., Meneux B., Mobasher B., Moreau C., Peacock J. A., Porciani C., Pozzetti L., Scaramella R., Schiminovich D., Shopbell P., Smail I., Thompson D., Tresse L., Vettolani G., Zanichelli A., Zucca E., 2007. ApJS, **172**, 70.

Lintott C., Schawinski K., Bamford S., Slosar A., Land K., Thomas D., Edmondson E., Masters K., Nichol R. C., Raddick M. J., Szalay A., Andreescu D., Murray P., Vandenberg J., 2011. MNRAS, **410**, 166.

MacArthur L. A., Courteau S., Holtzman J. A., 2003. ApJ, **582**, 689.

MacArthur L. A., Courteau S., Bell E., Holtzman J. A., 2004. *ApJS*, **152(2)**, 175.

Makarov D., Prugniel P., Terekhova N., Courtois H., Vauglin I., 2014. *A&A*, **570**, A13.

Martig M., Bournaud F., 2009.

Mehlert D., Thomas D., Saglia R. P., Bender R., Wegner G., 2003. *A&A*, **407**, 423.

Méndez-Abreu J., Aguerri J. A. L., Falcón-Barroso J., Ruiz-Lara T., Sánchez-Menguiano L., de Lorenzo-Cáceres A., Costantin L., Catalán-Torrecilla C., Zhu L., Sánchez-Blazquez P., Florido E., Corsini E. M., Wild V., Lyubenova M., van de Ven G., Sánchez S. F., Bland-Hawthorn J., Galbany L., García-Benito R., García-Lorenzo B., González Delgado R. M., López-Sánchez A. R., Marino R. A., Márquez I., Ziegler B., Califa Collaboration, 2018. MNRAS, **474**, 1307.

Mihos J. C., Hernquist L., 1996. ApJ, **464**, 641.

Moore B., Katz N., Lake G., Dressler A., Oemler A., 1996. Nature, **379**, 613.

Moster B. P., Macciò A. V., Somerville R. S., Naab T., Cox T. J., 2011. MNRAS, **415**, 3750.

Naab T., Burkert A., 2003. ApJ, **597**, 893.

Noordermeer E., Merrifield M. R., Aragón-Salamanca A., 2008. MNRAS, **388**, 1381.

Norris M. A., Sharples R. M., Kuntschner H., 2006. *MNRAS*, **367**, 815.

Obreschkow D., Glazebrook K., 2014. ApJ, **784**, 26.

Pedrosa S. E., Tissera P. B., 2015. A&A, **584**, A43.

Peletier R. F., Balcells M., 1996. *AJ*, **111**, 2238.

Peng C. Y., Ho L. C., Impey C. D., Rix H.-W., 2002. *AJ*, **124(1)**, 266.

Peng C. Y., Ho L. C., Impey C. D., Rix H.-W., 2010a. AJ, **139**, 2097.

Peng Y.-j., Lilly S. J., Kovač K., Bolzonella M., Pozzetti L., Renzini A., Zamorani G., Ilbert O., Knobel C., Iovino A., Maier C., Cucciati O., Tasca L., Carollo C. M., Silverman J., Kampczyk P., de Ravel L., Sanders D., Scoville N., Contini T., Mainieri V., Scodeggio M., Kneib J.-P., Le Fèvre O., Bardelli S., Bongiorno A., Caputi K., Coppa G., de la Torre S., Franzetti P., Garilli B., Lamareille F., Le Borgne J.-F., Le Brun V., Mignoli M., Perez Montero E., Pello R., Ricciardelli E., Tanaka M., Tresse L., Vergani D., Welikala N., Zucca E., Oesch P., Abbas U., Barnes L., Bordoloi R., Bottini D., Cappi A., Cassata P., Cimatti A., Fumana M., Hasinger G., Koekemoer A., Leauthaud A., Maccagni D., Marinoni C., McCracken H., Memeo P., Meneux B., Nair P., Porciani C., Presotto V., Scaramella R., 2010b. ApJ, **721**, 193.

Pérez E., Cid Fernandes R., González Delgado R. M., García-Benito R., Sánchez S. F., Husemann B., Mast D., Rodón J. R., Kupko D., Backsmann N., de Amorim A. L., van de Ven G., Walcher J., Wisotzki L., Cortijo-Ferrero C., CALIFA Collaboration, 2013. ApJ, **764**, L1.

Posti L., Fraternali F., Di Teodoro E. M., Pezzulli G., 2018. A&A, **612**, L6.

Querejeta M., Eliche-Moral M., Tapia T., Borlaff A., van de Ven G., Lyubenova M., Martig M., Falcón-Barroso J., Méndez-Abreu J., Zamorano J., Gallego J., 2015a. *Galaxies*, **3**, 202.

Querejeta M., Eliche-Moral M. C., Tapia T., Borlaff A., Rodríguez-Pérez C., Zamorano J., Gallego J., 2015b. A&A, **573**, A78.

Rasmussen J., Ponman T. J., Verdes-Montenegro L., Yun M. S., Borthakur S., 2008. MNRAS, **388**, 1245.

Rizzo F., Fraternali F., Iorio G., 2018. MNRAS, **476**, 2137.

Robertson B., Bullock J. S., Cox T. J., Di Matteo T., Hernquist L., Springel V., Yoshida N., 2006. ApJ, **645**, 986.

Romanowsky A. J., Fall S. M., 2012. ApJS, **203**, 17.

Saha K., Cortesi A., 2018. ApJ, **862**, L12.

Salim S., Charlot S., Rich R. M., Kauffmann G., Heckman T. M., Barlow T. A., Bianchi L., Byun Y.-I., Donas J., Forster K., Friedman P. G., Jelinsky P. N., Lee Y.-W., Madore B. F., Malina R. F., Martin D. C., Milliard B., Morrissey P., Neff S. G., Schiminovich D., Seibert M., Siegmund O. H. W., Small T., Szalay A. S., Welsh B. Y., Wyder T. K., 2005. ApJ, **619**, L39.

Sánchez S. F., Kennicutt R. C., Gil de Paz A., van de Ven G., Vílchez J. M., Wisotzki L., Walcher C. J., Mast D., Aguerri J. A. L., Albiol-Pérez S., Alonso-Herrero A., Alves J., Bakos J., Bartáková T., Bland-Hawthorn J., Boselli A., Bomans D. J., Castillo-Morales A., Cortijo-Ferrero C., de Lorenzo-Cáceres A., del Olmo A., Dettmar R.-J., Díaz A., Ellis S., Falcón-Barroso J., Flores H., Gallazzi A., García-Lorenzo B., González Delgado R., Gruel N., Haines T., Hao C., Husemann B., Iglésias-Páramo J., Jahnke K., Johnson B., Jungwiert B., Kalinova V., Kehrig C., Kupko D., López-Sánchez A. R., Lyubenova M., Marino R. A., Mármol-Queraltó E., Márquez I., Masegosa J., Meidt S., Mendez-Abreu J., Monreal-Ibero A., Montijo C., Mourão A. M., Palacios-Navarro G., Papaderos P., Pasquali A., Peletier R., Pérez E., Pérez I., Quirrenbach A., Relaño M., Rosales-Ortega F. F., Roth M. M., Ruiz-Lara T., Sánchez-Blázquez P., Sengupta C., Singh R., Stanishev V., Trager S. C., Vazdekis A., Viironen K., Wild V., Zibetti S., Ziegler B., 2012. *A&A*, **538**, A8.

Sánchez S. F., Rosales-Ortega F. F., Iglesias-Páramo J., Mollá M., Barrera-Ballesteros J., Marino R. A., Pérez E., Sánchez-Blazquez P., González Delgado R., Cid Fernandes R., de Lorenzo-Cáceres A., Mendez-Abreu J., Galbany L., Falcon-Barroso J., Miralles-Caballero D., Husemann B., García-Benito R., Mast D., Walcher C. J., Gil de Paz A., García-Lorenzo B., Jungwiert B., Vílchez J. M., Jílková L., Lyubenova M., Cortijo-Ferrero C., Díaz A. I., Wisotzki L., Márquez I., Bland-Hawthorn J., Ellis S., van de Ven G., Jahnke K., Papaderos P., Gomes J. M., Mendoza M. A., López-Sánchez Á. R., 2014. A&A, **563**, A49.

Schawinski K., Urry C. M., Simmons B. D., Fortson L., Kaviraj S., Keel W. C., Lintott C. J., Masters K. L., Nichol R. C., Sarzi M., Skibba R., Treister E., Willett K. W., Wong O. I., Yi S. K., 2014. MNRAS, **440**, 889.

Schwarzschild M., 1979. ApJ, **232**, 236.

Scodeggio M., Giovanelli R., Haynes M. P., 1998. *AJ*, **116(6)**, 2728.

Scorza C., Bender R., 1995. A&A, **293**.

Sérsic J., 1963. *Boletin de la Asociacion Argentina de Astronomia*, **6**.

Shapiro K. L., Gerssen J., van der Marel R. P., 2003. AJ, **126**, 2707.

Simard L., Mendel J. T., Patton D. R., Ellison S. L., McConnachie A. W., 2011. ApJS, **196**, 11.

Simard L., 1998. In: *Astronomical Data Analysis Software and Systems VII*, 108, eds Albrecht R., Hook R. N., Bushouse H. A.

Skrutskie M. F., Cutri R. M., Stiening R., Weinberg M. D., Schneider S., Carpenter J. M., Beichman C., Capps R., Chester T., Elias J., Huchra J., Liebert J., Lonsdale C., Monet D. G., Price S., Seitzer P., Jarrett T., Kirkpatrick J. D., Gizis J. E., Howard

E., Evans T., Fowler J., Fullmer L., Hurt R., Light R., Kopan E. L., Marsh K. A., McCallon H. L., Tam R., Van Dyk S., Wheelock S., 2006. *AJ*, **131**, 1163.

Smee S. A., Gunn J. E., Uomoto A., Roe N., Schlegel D., Rockosi C. M., Carr M. A., Leger F., Dawson K. S., Olmstead M. D., Brinkmann J., Owen R., Barkhouser R. H., Honscheid K., Harding P., Long D., Lupton R. H., Loomis C., Anderson L., Annis J., Bernardi M., Bhardwaj V., Bizyaev D., Bolton A. S., Brewington H., Briggs J. W., Burles S., Burns J. G., Castander F. J., Connolly A., Davenport J. R. A., Ebelke G., Epps H., Feldman P. D., Friedman S. D., Frieman J., Heckman T., Hull C. L., Knapp G. R., Lawrence D. M., Loveday J., Mannery E. J., Malanushenko E., Malanushenko V., Merrelli A. J., Muna D., Newman P. R., Nichol R. C., Oravetz D., Pan K., Pope A. C., Ricketts P. G., Shelden A., Sandford D., Siegmund W., Simmons A., Smith D. S., Snedden S., Schneider D. P., SubbaRao M., Tremonti C., Waddell P., York D. G., 2013. AJ, **146**, 32.

Smethurst R. J., Lintott C. J., Simmons B. D., Schawinski K., Marshall P. J., Bamford S., Fortson L., Kaviraj S., Masters K. L., Melvin T., Nichol R. C., Skibba R. A., Willett K. W., 2015. MNRAS, **450**, 435.

Smethurst R. J., Masters K. L., Lintott C. J., Weijmans A., Merrifield M., Penny S. J., Aragón-Salamanca A., Brownstein J., Bundy K., Drory N., Law D. R., Nichol R. C., 2018. MNRAS, **473**, 2679.

Sokołowska A., Capelo P. R., Fall S. M., Mayer L., Shen S., Bonoli S., 2017. ApJ, **835**, 289.

Springel V., Hernquist L., 2005. ApJ, **622**, L9.

Strateva I., Ivezić Ž., Knapp G. R., Narayanan V. K., Strauss M. A., Gunn J. E., Lupton R. H., Schlegel D., Bahcall N. A., Brinkmann J., Brunner R. J., Budavári T., Csabai I., Castander F. J., Doi M., Fukugita M., Győry Z., Hamabe M., Hennessy G., Ichikawa T., Kunszt P. Z., Lamb D. Q., McKay T. A., Okamura S., Racusin J., Sekiguchi M., Schneider D. P., Shimasaku K., York D., 2001. AJ, **122**, 1861.

Sweet S. M., Fisher D., Glazebrook K., Obreschkow D., Lagos C., Wang L., 2018. ApJ, **860**, 37.

Syer D., Tremaine S., 1996. MNRAS, **282**, 223.

Teklu A. F., Remus R.-S., Dolag K., Beck A. M., Burkert A., Schmidt A. S., Schulze F., Steinborn L. K., 2015. ApJ, **812**, 29.

Thob A. C. R., Crain R. A., McCarthy I. G., Schaller M., Lagos C. D. P., Schaye J., Talens G. J. J., James P. A., Theuns T., Bower R. G., 2018. *arXiv e-prints*.

Thomas D., Maraston C., Schawinski K., Sarzi M., Silk J., 2010. MNRAS, **404**, 1775.

Toomre A., 1977. ARA&A, **15**, 437.

Tremonti C. A., Heckman T. M., Kauffmann G., Brinchmann J., Charlot S., White S. D. M., Seibert M., Peng E. W., Schlegel D. J., Uomoto A., Fukugita M., Brinkmann J., 2004. ApJ, **613**, 898.

van Dokkum P. G., 2005. AJ, **130**, 2647.

Vazdekis A., Sánchez-Blázquez P., Falcón-Barroso J., Cenarro A. J., Beasley M. A., Cardiel N., Gorgas J., Peletier R. F., 2010. *MNRAS*, **404**, 1639.

Veale M., Ma C.-P., Greene J. E., Thomas J., Blakeslee J. P., McConnell N., Walsh J. L., Ito J., 2017. MNRAS, **471**, 1428.

Wake D. A., Bundy K., Diamond-Stanic A. M., Yan R., Blanton M. R., Bershady M. A., Sánchez-Gallego J. R., Drory N., Jones A., Kauffmann G., Law D. R., Li C., MacDonald N., Masters K., Thomas D., Tinker J., Weijmans A.-M., Brownstein J. R., 2017. AJ, **154**, 86.

Walcher C. J., Wisotzki L., Bekeraité S., Husemann B., Iglesias-Páramo J., Backsmann N., Barrera Ballesteros J., Catalán-Torrecilla C., Cortijo C., del Olmo A., Garcia Lorenzo B., Falcón-Barroso J., Jilkova L., Kalinova V., Mast D., Marino R. A., Méndez-Abreu J., Pasquali A., Sánchez S. F., Trager S., Zibetti S., Aguerri J. A. L., Alves J., Bland-Hawthorn J., Boselli A., Castillo Morales A., Cid Fernandes R., Flores H., Galbany L., Gallazzi A., García-Benito R., Gil de Paz A., González-Delgado R. M., Jahnke K., Jungwiert B., Kehrig C., Lyubenova M., Márquez Perez I., Masegosa J., Monreal Ibero A., Pérez E., Quirrenbach A., Rosales-Ortega F. F., Roth M. M., Sanchez-Blazquez P., Spekkens K., Tundo E., van de Ven G., Verheijen M. A. W., Vilchez J. V., Ziegler B., 2014. A&A, **569**, A1.

Weilbacher P. M., Streicher O., Urrutia T., Jarno A., Pécontal-Rousset A., Bacon R., Böhm P., 2012. In: Proc. SPIE, 84510B.

Willett K. W., Lintott C. J., Bamford S. P., Masters K. L., Simmons B. D., Casteels K. R. V., Edmondson E. M., Fortson L. F., Kaviraj S., Keel W. C., Melvin T., Nichol R. C., Raddick M. J., Schawinski K., Simpson R. J., Skibba R. A., Smith A. M., Thomas D., 2013. MNRAS, **435**, 2835.

Wong O. I., Schawinski K., Józsa G. I. G., Urry C. M., Lintott C. J., Simmons B. D., Kaviraj S., Masters K. L., 2015. MNRAS, **447**, 3311.

Wuyts S., Förster Schreiber N. M., van der Wel A., Magnelli B., Guo Y., Genzel R., Lutz D., Aussel H., Barro G., Berta S., Cava A., Graciá-Carpio J., Hathi N. P., Huang K.-H., Kocevski D. D., Koekemoer A. M., Lee K.-S., Le Floc'h E., McGrath E. J., Nordon R., Popesso P., Pozzi F., Riguccini L., Rodighiero G., Saintonge A., Tacconi L., 2011. ApJ, **742**, 96.

Yan R., Bundy K., Law D. R., Bershady M. A., Andrews B., Cherinka B., Diamond-Stanic A. M., Drory N., MacDonald N., Sánchez-Gallego J. R., Thomas D., Wake D. A., Weijmans A.-M., Westfall K. B., Zhang K., Aragón-Salamanca A., Belfiore F., Bizyaev D., Blanc G. A., Blanton M. R., Brownstein J., Cappellari M., D'Souza R., Emsellem E., Fu H., Gaulme P., Graham M. T., Goddard D., Gunn J. E., Harding P., Jones A., Kinemuchi K., Li C., Li H., Maiolino R., Mao S., Maraston C., Masters K., Merrifield M. R., Oravetz D., Pan K., Parejko J. K., Sanchez S. F., Schlegel D., Simmons A., Thanjavur K., Tinker J., Tremonti C., van den Bosch R., Zheng Z., 2016a. AJ, **152**, 197.

Yan R., Bundy K., Law D. R., Bershady M. A., Andrews B., Cherinka B., Diamond-Stanic A. M., Drory N., MacDonald N., Sánchez-Gallego J. R., Thomas D., Wake D. A., Weijmans A.-M., Westfall K. B., Zhang K., Aragón-Salamanca A., Belfiore F., Bizyaev D., Blanc G. A., Blanton M. R., Brownstein J., Cappellari M., D'Souza R., Emsellem E., Fu H., Gaulme P., Graham M. T., Goddard D., Gunn J. E., Harding P., Jones A., Kinemuchi K., Li C., Li H., Maiolino R., Mao S., Maraston C., Masters K., Merrifield M. R., Oravetz D., Pan K., Parejko J. K., Sanchez S. F., Schlegel D., Simmons A., Thanjavur K., Tinker J., Tremonti C., van den Bosch R., Zheng Z., 2016b. AJ, **152**, 197.

Zhu L., van den Bosch R., van de Ven G., Lyubenova M., Falcón-Barroso J., Meidt S. E., Martig M., Shen J., Li Z.-Y., Yildirim A., Walcher C. J., Sanchez S. F., 2018. MNRAS, **473**, 3000.